COUNTING THE UNCOUNTABLE: NON-GAUSSIAN QUANTUM OPTOMECHANICS

Ph.D. thesis

Ivan Galinskiy

Submitted to
UNIVERSITY OF COPENHAGEN
NIELS BOHR INSTITUTE
PH.D. SCHOOL OF SCIENCE

THE CLEANLINESS REQUIRED WAS NOT MERELY SURGICAL – IT WAS LEVITICAL.

- JOHN DRURY CLARK, 1971– , *IGNITION!: AN INFORMAL HISTORY OF LIQUID ROCKET PROPELLANTS*

COLOPHON
This thesis was set with LaTeX 2_ε using the *memoir* class.
The text font is Palatino 10, on normal A4 paper.
Mathematics typeset using the Euler font.
Graphics created using Matplotlib under Python 3.10, as well as Inkscape with a custom optical components library based on `ComponentLibrary` (CC BY-NC 3.0) by Alexander Franzen.
Initial LaTeXtemplate kindly provided by Christoffer Østfeldt.

Counting the uncountable: Non-Gaussian quantum optomechanics

Author Ivan Galinskiy
Advisor Prof. Dr. Eugene S. Polzik

UNIVERSITY OF
COPENHAGEN

QUANTOP

The Danish Center for Quantum Optics
The Niels Bohr Institute

This thesis has been submitted to the
PhD School
of
The Faculty of Science
University of Copenhagen
March 1st 2023

ABSTRACT

In this work, we use the force of light pressure to precisely control the motion of a vibrating thin membrane. We manage to reduce the motion of the main mode almost to the lowest possible level, limited only by the quantum mechanical ground-state motion. Then, we successfully convert this mechanical motion into information carried by light, and finally analyze this information using a photon detector capable of detecting single photons. We show, in a way, the manner in which the membrane's surrounding thermal environment influences its motion on a quantum level. Then we use the exceptional isolation of the main mechanical mode, enabled by the ultracoherent soft-clamped design of the membrane, to prepare non-classical, non-Gaussian states of its motion via heralded preparation. Analyzing the Cauchy-Schwarz parameter that stems from our statistics, we show strong evidence of non-classicality, i.e. that the behaviour of our system in this regime cannot be described by classical physics. This work brings us very close to demonstrating the possibility of creation of highly non-classical single-excitation states of macroscopic mechanical motion.

SAMMENFATNING

I dette værk udnytter vi kræften produceret af lys til at kontrollere bevægelsen af en tynd vibrerende membran. Vi lykkes at reducere bevægelsen af den primære mode til næsten det lavest mulige niveau, kun begrænset af den kvantemekaniske grundtilstands bevægelse. Dernæst konverterer vi denne mekaniske bevægelse til information, båret af lys, og endeligt analyserer vi denne information ved brug af en lys detektor, i stand til at detektere enkelte fotoner. Vi viser, på sin vis, måden hvorpå membranens termiske miljø påvirker dens bevægelse på et kvantemekanisk niveau. Dernæst bruger vi den exceptionelle isolation af den primære mekaniske mode, muliggjort af membranens ultra-kohærente blød-fæstnet (Soft-clamped) design, til at forberede ikke-klassiske, ikke-Gaussiske tilstande af dens bevægelse ved hjælp af bebudet forberedelse (Heralded preparation). Ved analyse af Cauchy-Schwarz parameteret som stammer fra vores statistik, viser vi stærk evidens for ikke-klassikalitet (Non-classicality), hviket vil sige, at vores systems opførsel ikke kan beskrives med klassisk fysik. Dette værk bringer os meget tæt på at demonstrere muligheden for skabelsen af yderst ikke-klassiske enkelt-excitations tilstande af makroskopisk mekanisk bevægelse.

ACKNOWLEDGMENTS

None of this work would have been possible, has it not been for the support, help, and wisdom of many people.

First, Eugene, I would like to thank you for being an inspiration to our work, an exemplary advisor, brilliant physicist, and a great human being. You were there during hard times, always cheerful and motivating, and without your support this would not be possible.

Yeghishe Tsaturyan, there is a reason why we nicknamed you "The God of Membranes". Your talent and expertise in physics, experimental and theoretical, are legendary. And your person, friendly and understanding, has helped so many of us throughout our lives. I am certain that whatever future lies ahead of you, it will be bright.

Christoffer Moller, we've known each other since you were my TA in Eugene's class, and not for a single moment did you fail to bring joy to whatever place you happened to be in. You were among the first people to teach me "The way of QUANTOP", and will be always remembered as the proud owner of a sneeze capable of causing an avalance of failing PID loops like no other, limited only by the amount of PID loops available.

Andi Barg, you were the first person with whom I started doing quantum optics, the real stuff. I have learned so much from your expertise in the field, and am glad to have been part of your team!

Michal Parniak, for when our mirrors needed a little more Polish. You know it all, not just experiments, but techniques and theory too. The amount of things that I learned, and keep learning from you, is astonishing. I can hardly repel expertise of that magnitude!

Georg Enzian, thank you for being a jolly part of the Fock team! Your readiness to perform the most challenging tasks for the experiment, and your Tesla-coil-building-fuelled expertise in all matters RF has opened a new way of looking at so many things. We both went through some hard times, and I sincerely wish you all the best, and thank you for being patient and understanding with me.

Chao Meng, the newest member of the single-phonon team, I cannot praise you enough for your solid grasp of the theory of optomechanics. Learning a new experiment, with all its black boxes, reinvented wheels, and strange quirks is never easy, and you are learning them at an impressive rate! I am glad to continue working with you in the coming time.

Jürgen Appel, I owe you uncountably many of the skills that I learned under your guidance. Your legacy in QUANTOP is hard to oversee, with nearly all custom electronics still bearing your oh-not-so-gentle touch. Additionally, I still marvel at the relativistic speeds which you sustained when biking to pick up your kids from kindergarten after a day's work.

Jörg Helle Müller, I cannot help but wonder at the depth and breadth of your knowledge of science, literature, and music. In physics, there is hardly a time where I did not learn something new from you, even for the wildest hypothetical questions. I still remember when we were filling a vacuum system with CO_2 from a balloon to investigate the nature of noise, mysterious to us at the time.

To all the former students in our experiments: Jonas Mathiassen, your

talent in finding unusual solutions to unusual problems in the experiment is astounding! The nice warm hat for a temperature-controlled cavity is now a historical artifact in the Dungeon Lab. Timo Zwettler, the only person in my life that learned Verilog before "more normal" programming, you're a steamroller that paves the way of experimental physics! Georgia "Yiouli" Anyfantaki, thank you for being an excellent student and a dear friend.

Rebecca Schmieg, you are an exceptionally talented, hard-working, and compassionate person. I thank you for all of your support before, during, and after the writing of this thesis.

I would like to thank the friendly gang of the "Hybrid" experiment: Christoffer Bo Østfeldt, apart from your unquestionable talent in physics, I am in awe of your discipline and perseverence. Without any doubt, you are the "Lawful Good" of a DnD alignment, and you have never let us down. Rodrigo, "The Spin Whisperer", I thank you for being a cheerful, friendly, and kind soul. Peyman, you are learning the extremely complex "Hybrid" experiment at an alarming rate, keep it up! Christian, the magician that puts the tophat into the beam, best of wishes with writing your PhD thesis. Sergey, you are an example of experience and unconditional persistence. Emil, the theory mastermind who never strays too far from our earthly experiments.

Tulio Brasil, thank you for being an understanding friend and colleague with a remarkable set of DIY experimental skills.

To all former and present QUANTOP members: Jacob, thank you for being a great mate and a fellow pundit! Michael, Karsten, Signe, Valeriy, Jun, and many others: thank you for bringing life to our discussions and coffee breaks!

To members of SLAB: I would like to personally thank Massi Rossi, David Mason, Eric Planz, Eric Langman, Sampo Saarinen, Letizia Catalini, Yannick Seis, Mads Kristensen, Thibault Capelle and, of course, Albert Schliesser. Thank you for being great fellows, and an endless source of knowledge on optomechanics!

To the folks at HyQ: in addition to unquestionable scientific achievements, your social achievements don't lag behind!

To my fellow pilot friends at the Polyteknisk Flyvegruppe gliding club: thank you for showing me that sky is not the limit (the lack of thermals still is). I would especially like to thank Morten Bennick for being a great instructor and friend, who supported me when I needed it the most. To Leopold Broby, thank you for your friendship, knowledge of the broadest kind, and my most memorable flights. And to Felipe Cvitanich, thank you for your calm and constructive instructorship, and for dragging myself and the glider out of a field surrounded by an electric fence, while being observed by cows and a slightly aggressive bull.

To my family: I am infinitely grateful for your support and understanding, even though we are separated by thousands of kilometers. To my mom and dad, Svetlana and Vadim, to my brother Mikhail, to my grandmas Tatiana and Lyudmila, thank you.

Last but not least, I would like to thank the people who have helped me by listening to my long monologues that we recorded and later transcribed into text that served as the seed for this work. Peyman Malekzadeh, Tulio Brasil, Rebecca Schmieg, Evi Aspropotamiti, a sincere "thank you"!

PRIOR WORK AND FUTURE DIRECTIONS

This thesis has been preceded by the following publications by the author and collaborators:

- I. Galinskiy et al. (June 2020a). "Phonon Counting Thermometry of an Ultracoherent Membrane Resonator near Its Motional Ground State". In: *Optica* 7.6, pp. 718–725. DOI: 10.1364/OPTICA.390939. URL: http://www.osapublishing.org/optica/abstract.cfm?URI=optica-7-6-718
- Michał Parniak et al. (Mar. 1, 2021). "High-Frequency Broadband Laser Phase Noise Cancellation Using a Delay Line". In: *Optics Express* 29.5, pp. 6935–6946. ISSN: 1094-4087. DOI: 10.1364/OE.415942. URL: https://opg.optica.org/oe/abstract.cfm?uri=oe-29-5-6935 (visited on 02/01/2023)

In addition, the following conference posters have been presented:

- Ivan Galinskiy, Georg Enzian, et al. (5/Sep/2021). "Counting MHz Phonons: Towards Generaton of Non-Gaussian Quantum States of Moton". In: Quantum Optics X. Torun, Poland
- Ivan Galinskiy, Yeghishe Tsaturyan, et al. (2/Dec/2018). "Towards Heralded Single-Phonon State Generation of an Ultracoherent Nanomechanical Resonator". In: Advances in Open Systems and Fundamental Tests of Quantum Mechanics. Bad Honnef, Germany

Finally, currently there is a manuscript under preparation that will present our results of Cauchy-Schwarz inequality violation, described in this work in Chapter 10.

DETAILED TABLE OF CONTENTS

Part I

INTRODUCTION

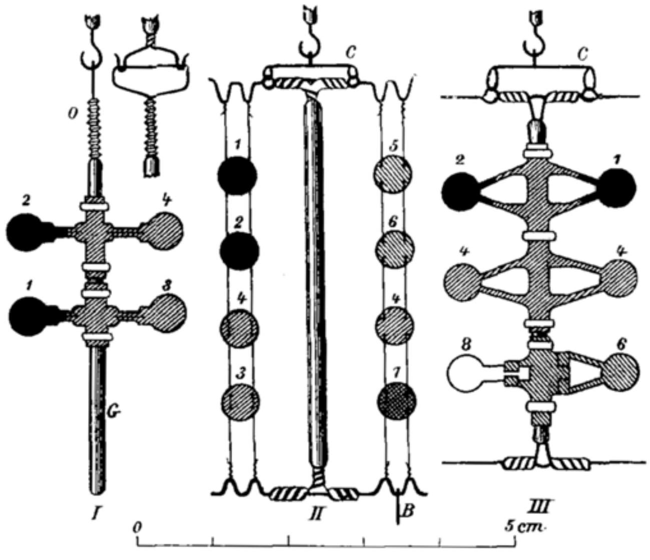

Fig. 3 (natürl. Grösse).

To-scale schematic of the experiment of Lebedew (1901) for measuring the pressure of light.

Chapter 1

Introduction

Quantum mechanics is often described as study of objects on microscale. "Microscale" refers to physical microscale, a world where single particles play together, and where even a the tiniest virus is a behemoth. And yet, the birthplace of quantum mechanics is precisely the macroscopic world, where Planck took the first macroscopically giant leap, explaining the nature of thermal radiation emitted by incandescent objects (Planck 1900)(1). Quantum mechanics indeed closed several large gaps in our understanding of thermodynamics, bringing a deep explanation of the entropy, a very macroscopic phenomenon, by linking it with the microscopic world. In hindsight, the first system that obtained its quantum description via Planck's work, where he postulated quantization of energy "in an act of desperation"(2), was a harmonic oscillator.

What followed next was an avalanche of results, both theoretical and experimental, in time for more and more sophisticated experiments that manipulated matter and energy on increasing levels of precision. The works of De Broglie (De Broglie 1923)(3) and Bohr (Bohr 1913)(4) explained the wave-like behaviour of matter, and explained a great amount of properties of light emission and absorption by simple atoms. Schrödinger (Schrödinger 1926)(5) and Heisenberg (Heisenberg 1925)(6), in turn, laid the theoretical foundation on which modern quantum theory stands, allowing the semi-classical description of atoms by Bohr to be corrected and extended to explain essentially all properties of atomic emission, and allowing the quantum description to be applied, at least in principle, to essentially all non-relativistic problems. We are, of course, skipping many other beautiful results in quantum theory for brevity.

As we said, the first results were applied to explain behaviour of collections of quantum objects. In the times when quantum mechanics were Born(7), the state of technology would not allow experiments to be performed on single atoms. Many of the ground-laying results from that era studied the fundamental behaviour of large collections of atoms, such as emission lines of a discharge lamp, heat capacity of solids, etc. Particle accelerators,

(1) Max Planck (1900). "Entropie Und Temperatur Strahlender Wärme". In: *Annalen der Physik* 306.4, pp. 719–737. ISSN: 1521-3889. DOI: 10.1002/andp.19003060410. URL: https://onlinelibrary.wiley.com/doi/abs/10.1002/andp.19003060410 (visited on 03/07/2023).

(2) quote attributed to Planck

(3) Louis De Broglie (Oct. 1923). "Waves and Quanta". In: *Nature* 112.2815 (2815), pp. 540–540. ISSN: 1476-4687. DOI: 10.1038/112540a0. URL: https://www.nature.com/articles/112540a0 (visited on 03/07/2023).

(4) N. Bohr (July 1, 1913). "I. On the Constitution of Atoms and Molecules". In: *The London, Edinburgh, and Dublin Philosophical Magazine and Journal of Science* 26.151, pp. 1–25. ISSN: 1941-5982. DOI: 10.1080/14786441308634955. URL: https://doi.org/10.1080/14786441308634955 (visited on 03/07/2023).

(5) E. Schrödinger (1926). "Quantisierung Als Eigenwertproblem". In: *Annalen der Physik* 384.4, pp. 361–376. ISSN: 1521-3889. DOI: 10.1002/andp.19263840404. URL: https://onlinelibrary.wiley.com/doi/abs/10.1002/andp.19263840404 (visited on 03/07/2023).

(6) W. Heisenberg (Dec. 1, 1925). "Über quantentheoretische Umdeutung kinematischer und mechanischer Beziehungen." In: *Zeitschrift für Physik* 33.1, pp. 879–893. ISSN: 0044-3328. DOI: 10.1007/BF01328377. URL: https://doi.org/10.1007/BF01328377 (visited on 03/07/2023).

(7) not a typo

and their detection techniques, were among the first systems that allowed to visualize the trajectories of single particles after their interaction. Advances in vacuum tube technology then enabled the construction of photomultiplier and electromultiplier tubes, among the first experimental devices able to detect, in the modern sense of the word, single particles.

1.1 History of light pressure

It is rather amazing that light can exert pressure, to be honest. We are accustomed in our daily life (8) that light is a thing that is "there". It can illuminate, or even burn, but we never experience light pressure. Of course, that is due to the simple fact the force that a light source can exert is extremely tenuous, on the order of P/c. To levitate a single mosquito (2 mg), one would require about 5 kW of light power, which is rather likely to convert the poor thing into plasma in a couple of milliseconds.

However, light pressure does have visible effects, which many of us have seen as the tail of a comet(9). As far as 1619, Kepler observed the fact that a comet's tail always pointed away from the sun (Keplero 1619)(10), which he attributed to Sun's light pushing it away. Back then it was only a hypothesis, of course, as experimental techniques capable of measuring such a miniscule force did not exist yet, and neither did a theory capable of predicting its magnitude. That theory was created a few centuries later as a corollary to the foundational work of Maxwell on the behaviour of electromagnetic waves (Maxwell 1873)(11), where we finally found the force that an electromagnetic wave would produce. As stated above, it is simply P/c upon full absorption in the object, with P being the power of the incident wave, and c being the speed of light. A small force indeed!

It took a few decades more to measure this force reliably, experimentally shown in the beautiful experiments of (Lebedew 1901)(12) and (Nichols and Hull 1903)(13), both of which accounted for other light-induced forces, especially heat-induced ones that power Crookes' radiometers. Light pressure remained somewhat of a curiosity, as with light sources available at the time it was not possible to create light intensities necessary for much observable force. With the advent of lasers (Maiman 1960)(14), however, everything changed. Due to lasers' single-mode emission, focusing large powers of light to a very tight spot became possible. Shortly after, Ashkin (Ashkin 1970)(15) demonstrated optical trapping of microscopic spheres, which in turn led to the creation of a whole new field: optical tweezers. These devices are used nowadays as a standard technique in microbiology, and are a welcome guest in many quantum experiments, where even single atoms can be held nicely and firmly in the warm embrace of a beam waist. The author himself has done work on interferometric techniques in optical tweezers (Ivan Galinskiy, Meza, and Hautefeuille 2014)(16).

The masses manipulated by light were getting bigger and bigger, culminating in the massive test masses of interferometric gravitational wave detectors. We shall briefly overview those next.

(8) outside of the lab, that is

(9) The white uncharged dust part of it, as the charged ionized tail prefers to follow magnetic lines of the Sun instead

(10) Iohanne Keplero (1619). *De Cometis Libelli Tres*. Typis Andreae Apergeri, p. 168.

(11) James Clerk Maxwell (1873). *A Treatise on Electricity and Magnetism*. Vol. 1. Clarendon press.

(12) Peter Lebedew (1901). "Untersuchungen Über Die Druckkräfte Des Lichtes". In: *Annalen der Physik* 311.11, pp. 433–458. DOI: 10.1002/andp.19013111102.

(13) E. F. Nichols and G. F. Hull (1903). "The Pressure Due to Radiation". In: *Proceedings of the American Academy of Arts and Sciences* 38.20, pp. 559–599. ISSN: 0199-9818. DOI: 10.2307/20021808. JSTOR: 20021808. URL: https://www.jstor.org/stable/20021808 (visited on 03/07/2023).

(14) T. H. Maiman (Aug. 1960). "Stimulated Optical Radiation in Ruby". In: *Nature* 187.4736 (4736), pp. 493–494. ISSN: 1476-4687. DOI: 10.1038/187493a0. URL: https://www.nature.com/articles/187493a0 (visited on 03/07/2023).

(15) A. Ashkin (Jan. 26, 1970). "Acceleration and Trapping of Particles by Radiation Pressure". In: *Physical Review Letters* 24.4, pp. 156–159. DOI: 10.1103/PhysRevLett.24.156. URL: https://link.aps.org/doi/10.1103/PhysRevLett.24.156 (visited on 03/07/2023).

(16) Ivan Galinskiy, Jose Luis Meza, and Mathieu Hautefeuille (2014). "Counter-propagating Sagnac Optical Tweezers as an Efficient Method for 3D Trapping in Air". In: *Latin America Optics and Photonics Conference*, LTu4A.31. DOI: 10.1364/LAOP.2014.LTu4A.31. URL: https://www.osapublishing.org/abstract.cfm?uri=LAOP-2014-LTu4A.31.

1.2 NON-CLASSICAL MECHANICAL OBJECTS

Despite the name "quantum mechanics", historically most of quantum work was done on everything but mechanics. I mean this in the most respectful sense, as it was indeed quite difficult to experiment with things that we would call "mechanical" until the second half of the 20th century. But then the situation began to change, as the experimental techniques were becoming more and more precise, measuring smaller and smaller displacements. We owe a lot of research in optomechanics to the gravitational-wave community, where measurements of distance fluctuations among the most precise measurements ever done. It is due to this precision that even effects such light shot noise, an intrinsically quantum phenomenon, start to play a role (Caves 1981)(17),(18). On the other hand, theoretical work by Braginsky and colleagues both introduced a lot of the theory of measurement of mechanical motion (Vladimir B. Braginsky, Vorontsov, and Kip S. Thorne 1980)(19), and experimentally showed non-trivial ponderomotive effects of electromagnetic pressure (V. B. Braginsky and Manukin 1967)(20). While targeted at gravitational-wave detectors, where measurement of mass positions is above all, these works laid a foundation and motivated further work on *interaction* between electromagnetic radiation and mechanical motion.

It is difficult to point to a specific work that really "started quantum optomechanics", so we instead point the reader to the excellent review article (Aspelmeyer, Kippenberg, and F. Marquardt 2014)(21) that covers a multitude of different aspects of our multi-faceted field. It is fair to say, however, that nowadays optomechanics is performed on anything that moves(22), including but not limited to bacteria (Gil-Santos et al. 2020)(23). Optomechanical interaction has been achieved with liquid helium (Shkarin et al. 2019)(24), microtoroids (Jiang et al. 2009)(25), and many other systems, too many to count.

What unites most of these experiments is the size of the mechanical oscillator: it is nearly always a "big thing", involving the collective motion of a great multitude of individual atoms. For us, for example, a nanogram effective mass corresponds to *trillions* of atoms participating in the motion, and the large size of the mode, on the order of 100 μm(26) makes the object visible to the naked eye. Efforts in other groups are underway to increase the absolute *mass* of the object in motion, in hopes of measuring gravity effects on quantum states.

In this work we push our macroscopic system towards nonclassicality as well, and shall explain that in Chapter 10.

1.3 NOTABLE PREVIOUS WORK ON NON-CLASSICAL MECHANICS

In experimental physics, one always stands on the shoulders of giants, many of them. It is a rather wobbly construction, and many of our field's achievements are due to people falling off that tower. And yet, moving sideways from the peak often reveals beautiful landscapes. In the GHz domain, the work of Simon Gröblacher's group, for example, has already shown nonclassicality of photon-phonon pairs (Riedinger, Hong, et al. 2016)(27), together with subsequent entanglement of two oscillators through a similar setup (Riedinger, Wallucks, et al. 2018)(28).

(17) Carlton M. Caves (1981). "Quantum-Mechanical Noise in an Interferometer". In: *Physical Review D: Particles and Fields* 23.8, pp. 1693–1708. DOI: 10.1103/PhysRevD.23.1693.

(18) although it is until recently that other sources of noise were brought down enough for shot noise to really matter

(19) Vladimir B. Braginsky, Yuri I. Vorontsov, and Kip S. Thorne (1980). "Quantum Nondemolition Measurements". In: *Science (New York, N.Y.)* 209.4456, pp. 547–557. DOI: 10.1126/science.209.4456.547.

(20) V. B. Braginsky and A. B. Manukin (1967). "Ponderomotive Effects of Electromagnetic Radiation". In: *Soviet Physics JETP*.

(21) Markus Aspelmeyer, Tobias J. Kippenberg, and Florian Marquardt (Dec. 2014). "Cavity Optomechanics". In: *Reviews of Modern Physics* 86.4, pp. 1391–1452. ISSN: 0034-6861. DOI: 10.1103/RevModPhys.86.1391. URL: https://link.aps.org/doi/10.1103/RevModPhys.86.1391.

(22) pun intended

(23) Eduardo Gil-Santos et al. (June 2020). "Optomechanical Detection of Vibration Modes of a Single Bacterium". In: *Nature Nanotechnology* 15.6 (6), pp. 469–474. ISSN: 1748-3395. DOI: 10.1038/s41565-020-0672-y. URL: https://www.nature.com/articles/s41565-020-0672-y (visited on 03/07/2023).

(24) A. B. Shkarin et al. (Apr. 15, 2019). "Quantum Optomechanics in a Liquid". In: *Physical Review Letters* 122.15, p. 153601. DOI: 10.1103/PhysRevLett.122.153601. URL: https://link.aps.org/doi/10.1103/PhysRevLett.122.153601 (visited on 03/07/2023).

(25) Xiaoshun Jiang et al. (Nov. 9, 2009). "High-Q Double-Disk Microcavities for Cavity Optomechanics". In: *Optics Express* 17.23, pp. 20911–20919. ISSN: 1094-4087. DOI: 10.1364/OE.17.020911. URL: https://opg.optica.org/oe/abstract.cfm?uri=oe-17-23-20911 (visited on 03/07/2023).

(26) though only 15 nm thick

(27) Ralf Riedinger, Sungkun Hong, et al. (2016). "Non-Classical Correlations between Single Photons and Phonons from a Mechanical Oscillator". In: *Nature* 530.7590, pp. 313–316. ISSN: 0028-0836. DOI: 10.1038/nature16536. pmid: 26779950. URL: http://www.nature.com/doifinder/10.1038/nature16536.

(28) Ralf Riedinger, Andreas Wallucks, et al. (Apr. 2018). "Remote Quantum Entanglement between Two Micromechanical Oscillators". In: *Nature* 556.7702 (7702), pp. 473–477. ISSN: 1476-4687. DOI: 10.1038/s41586-018-0036-z. URL: https://www.nature.com/articles/s41586-018-0036-z (visited on 03/15/2023).

Part II

THEORY

CHAPTER 2

LIGHT

> The career of a young theoretical physicist consists of treating the harmonic oscillator in ever-increasing levels of abstraction.
>
> SIDNEY COLEMAN

2.1 OPTICAL CAVITIES

Optical cavities are one of the central topics of this thesis. We use them for filtering, stabilization, and most importantly, optomechanical interaction. To be clear, while we often refer to "optical cavities" or simply "cavities", most results are generally applicable to any other optical resonator, such as, for example, microresonators. However, we will focus our description on Fabry-Pérot resonators.

A Fabry-Pérot resonator is a conceptually simple optical device that consists of two mirrors that recirculate the light inside of the cavity. We will discuss the geometric properties of those mirrors below, and for now will focus on their purely optical properties. Each mirror will reflect a certain amount of light into the cavity, and transmit or absorb the rest. We denote the *power* reflectivity and transmittivity as R and T respectively. When the mirror is entirely lossless, i.e. no power is absorbed or scattered, $R + T = 1$. However, that's unfortunately never the case, so we define the loss (absorption, scattering, or any other irreversible process) as L, so that $R + T + L = 1$. The two mirrors need not be the same, in which case we will use subscripts to distinguish them.

Optical resonators, as the name suggests, display resonances due to light interference. Historically, Fabry-Pérot resonators were first made as highly polished plates of glass, where the reflectivity was due to the mismatch between the refractive index of glass and the surrounding medium. This form would be called an *etalon*. For us, using discrete mirrors gives more freedom in choosing reflectivity, distance, and geometric properties. The mathematics are entirely the same, however. For the derivations, we refer the reader to

Ismail et al. (2016)(1), where the relevant derivations have been carried out in great detail. In a nutshell, to obtain the reflection, transmission, and intracavity power of a Fabry-Pérot resonator, one sets the necessary external field (usually one incident beam), and uses boundary conditions of the mirrors to obtain all the other fields. After that is carried out, we obtain the circulating, reflected, and transmitted field strenghts:

$$E_{\mathrm{circ}} = \frac{it_1}{1 - r_1 r_2 e^{-2i\phi}} \tag{2.1}$$

$$E_{\mathrm{trans}} = \frac{-t_1 t_2 e^{-i\phi}}{1 - r_1 r_2 e^{-2i\phi}} \tag{2.2}$$

where we have set the incident field to 1 for simplicity, i.e. $E_{\mathrm{inc}} = 1$, without loss of generality. Note that we have introduced the *amplitude* transmission and reflection for both mirrors as t_n and r_n, with $n \in \{1, 2\}$. While (Ismail et al. 2016) does not contain an expression for the reflected field, we shall derive it soon.

2.1.1 T-matrix method for optical resonators

Calculating electric fields in optical cavities is sometimes a bit of a chore, especially when the cavity has elements inside of it. One has to solve coupled field equations, which tends to be error-prone if done by hand. However, the RF design community has had the same problem for a long time now, and has come with the concept of S-parameters and T-parameters (members of a bigger family of *scattering parameters*). Let us consider some optical component, such as a mirror. When we operate with a single mode of light, it can be considered a *2-port device*, as it has one input and one output. We shall call the fields on the left a_1 and b_1 (a is incident and b is "scattered"). Likewise, the fields on the right side of the system are a_2 and b_2, as shown in Fig. 2.1.

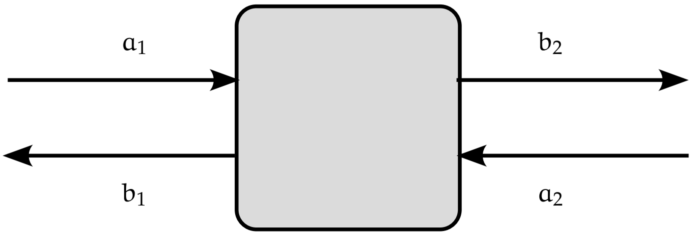

Figure 2.1: Field definitions of a general two-port system

This notation might look odd at first, but the rationale is to label incident and scattered fields separately, while using the subscript to denote the port in question. As you will see soon, this ends up being convenient for multi-component systems. The scattered fields are defined from incident

(1) Nur Ismail et al. (July 25, 2016). "Fabry-Pérot Resonator: Spectral Line Shapes, Generic and Related Airy Distributions, Linewidths, Finesses, and Performance at Low or Frequency-Dependent Reflectivity". In: *Optics Express* 24.15, pp. 16366–16389. ISSN: 1094-4087. DOI: 10.1364/OE.24.016366. URL: https://opg.optica.org/oe/abstract.cfm?uri=oe-24-15-16366 (visited on 02/13/2023).

fields using the *scattering matrix*, or S-matrix. Before we begin, however, it is necessary to establish a convention on the precise definition of both S- and T-matrices, as there are several accepted forms. We will follow the definitions from one of the most known books on RF design, Egan (2003)(2).

$$\begin{pmatrix} b_1 \\ b_2 \end{pmatrix} = \begin{pmatrix} S_{11} & S_{12} \\ S_{21} & S_{22} \end{pmatrix} \cdot \begin{pmatrix} a_1 \\ a_2 \end{pmatrix} \tag{2.3}$$

The S-matrix is very convenient in that it is easy to measure. Both for RF devices and optical devices, one simply applies some input to each port and measures the output signal on all the other ports (including the reflection on the original port). Phase also has to be measured, but for simple optical devices such as mirrors, we already know the phase response. For RF devices, phase is measured directly.

The S-matrix, however, is not directly applicable if we want to calculate the response of a composite system, such as an optical cavity. For this purpose, we define the *transfer matrix* (or transition matrix, depending on whom you ask), called T-matrix for brevity. Instead of relating incident fields with scattered fields, it instead defines the relation between fields in one port to the fields in the other. In other words, it answers the question "given fields on the right, what are the fields on the left?". The advantage of such approach is that now we can simply multiply the T-matrices of several components together to obtain the T-matrix of the composite system. It is defined as follows:

$$\begin{pmatrix} a_1 \\ b_1 \end{pmatrix} = \begin{pmatrix} T_{11} & T_{12} \\ T_{21} & T_{22} \end{pmatrix} \cdot \begin{pmatrix} b_2 \\ a_2 \end{pmatrix} \tag{2.4}$$

Pay close attention to the ordering of a and b terms: it is different on different sides. This is not a mistake: remember that when two components are "stacked", a field scattered from one component becomes incident on another component. This arrangement allows us to multiply matrices together directly when dealing with composite systems.

The T-matrix cannot be measured easily. Fortunately, the S- and T- matrices are related and can be easily converted between one another for the case of 2-port systems. Given an S-matrix, the corresponding T-matrix can be obtained as follows (Egan 2003):

$$T = \frac{1}{S_{21}} \cdot \begin{pmatrix} 1 & S_{22} \\ S_{11} & \det S \end{pmatrix} \tag{2.5}$$

Correspondingly, the S-matrix can be obtained from the T-matrix:

$$S = \frac{1}{T_{11}} \cdot \begin{pmatrix} T_{21} & \det T \\ 1 & -T_{12} \end{pmatrix} \tag{2.6}$$

These two conversions are what enables us to use this method easily. For example, we know from optics that a mirror of a given amplitude reflectivity r and transmissivity tb (Fig. 2.2) will act on its inputs as follows:

$$S_{\mathrm{mirror}} \equiv S_m(r,t) = \begin{pmatrix} -r & t \\ t & r \end{pmatrix} \tag{2.7}$$

(2) William Egan (Apr. 2, 2003). *Practical RF System Design*. John Wiley & Sons, Inc. ISBN: 978-0-471-65409-4. URL: https://doi.org/10.1002/0471654094.

Note the different sign in front of the reflection coefficients. This due to a phase shift that necessarily occurs when light is bounced off a higher refractive index at normal incidence, as highlighted in Fig. 2.2.

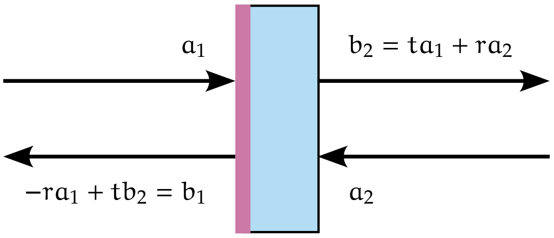

Figure 2.2: Fields around an optical mirror in S-matrix form

The S-matrix of the mirror can then be transformed into the corresponding T-matrix:

$$T_m = \frac{1}{t} \cdot \begin{pmatrix} 1 & -r \\ -r & r^2 + t^2 \end{pmatrix} \tag{2.8}$$

Note that the T-matrix is undefined for a mirror with t = 0. This is expected, since if a mirror is not transmitting anything, we cannot know the fields on one side of it from the fields on the other side.

Similarly, propagation through free space (including uniform dielectrics) has simple S- and T-representations that show a phase shift:

$$S_{\text{free space}} \equiv S_f(kL) = e^{ikL} \cdot \begin{pmatrix} 0 & 1 \\ 1 & 0 \end{pmatrix} \tag{2.9}$$

$$T_f(\phi) = \begin{pmatrix} e^{-i\phi} & 0 \\ 0 & e^{i\phi} \end{pmatrix} \tag{2.10}$$

where we have defined $\phi = kL$ to be the phase shift due to propagation. This lightens up the notation a little bit, as writing "kL" all the time is a bit clunky.

Finally, we can apply all of the above to calculate the properties of a simple Fabry-Pérot resonator, as shown in Fig. 2.3.

First, multiply the T matrices togeter:

$$T_{\text{Fabry-Pérot}} \equiv T_{FP} = T_m(-r_1, t_1) \cdot T_f(\phi) \cdot T_m(r_2, t_2) \tag{2.11}$$

where we are not writing out the expressions, as it is more conveniently done using some computer algebra system. Since we want to know the reflection and transmission given some input, we convert the T-matrix into an S-matrix. Most of the time, the input comes from only one side only, so we additionally multiply it by a normalized input vector with only one nonzero component:

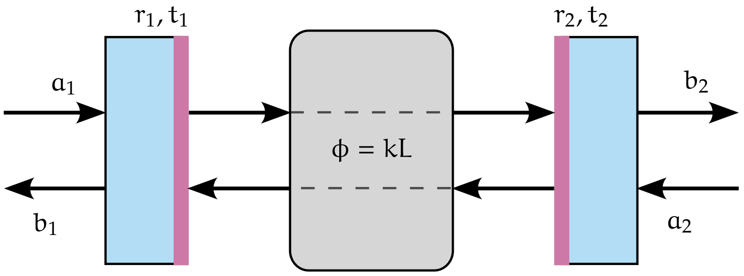

Figure 2.3: 2-port approach to solving a Fabry-Pérot resonator

$$S_{FP} \cdot \begin{pmatrix} 1 \\ 0 \end{pmatrix} = \frac{1}{1 - e^{2i\phi} r_1 r_2} \cdot \begin{pmatrix} r_1 - r_2 e^{2i\phi}(r_1^2 + t_1^2) \\ e^{i\phi} t_1 t_2 \end{pmatrix} \tag{2.12}$$

The first component of that vector is the reflection of the cavity, while the second is the transmission. As you can see, that was pretty easy. The same technique is even more useful when one works with a system that contains multiple components in addition to the mirrors. The case of a membrane-in-the-middle system is a bit more involved and requires splitting the cavity into two sub-resonators, to which we refer the reader to Jayich et al. (2008)(3). We will continue deriving the results for a simple cavity. First, let's compute the power reflection and transmission by multiplying the above expressions elementwise with their complex conjugates. The power transmission of such a cavity is:

$$\mathcal{T} = \frac{t_1^2 t_2^2}{1 + r_1^2 r_2^2 - 2 r_1 r_2 \cos(2\phi)} \tag{2.13}$$

By completing the squares in the denominator and using $2\sin^2(\phi) = 1 - \cos(2\phi)$, we obtain a more suggestive and familiar expression:

$$\mathcal{T} = \frac{t_1^2 t_2^2}{(1 - r_1 r_2)^2 + 4 r_1 r_2 \cdot \sin^2(\phi)} \tag{2.14}$$

which is indeed the correct transmission of a Fabry-Pérot resonator, in accordance with (Ismail et al. 2016).

From the above, we can determine that the transmission function is periodic, with a period of $\Delta\phi = \pi$, and reaches its maximum values at $\phi = \pi \cdot n$ for integer n. In case of a free-space resonator, $\phi = kL = 2\pi L/\lambda = \omega L/c$. Therefore, we get our first definition, that of **Free Spectral range**, or **FSR**:

$$\Delta\omega_{FSR} \equiv \frac{\pi c}{L} \tag{2.15}$$

(3) A M Jayich et al. (Sept. 2008). "Dispersive Optomechanics: A Membrane inside a Cavity". In: *New Journal of Physics* 10.9, p. 095008. DOI: 2008100103130400. URL: https://dx.doi.org/10.1088/1367-2630/10/9/095008.

We shall now look more closely at the transmission of the cavity. To make (2.14) a bit more succinct, let us make a reasonable assumption.In the majority of experimental cases, the mirrors are low-loss, so typically $1 - r^2 < 0.001$. Treating $r_1 r_2$ as a single variable very close to 1 such that $r_1 r_2 = 1 - \delta$, we can rewrite (2.14) as:

$$\mathcal{T} = \frac{t_1^2 t_2^2}{(1 - r_1 r_2)^2} \cdot \frac{1}{1 + \frac{4 r_1 r_2}{(1 - r_1 r_2)^2} \cdot \sin^2(\phi)} \tag{2.16}$$

$$\approx \frac{t_1^2 t_2^2}{\delta^2} \cdot \frac{1}{1 + \frac{4}{\delta^2} \cdot \sin^2(\phi)} \tag{2.17}$$

Now note that since δ is very small, $4/\delta^2$ will be very large, i.e. the transmission will be significant only for $\phi \approx 0$, so we approximate $\sin^2(\phi) \approx \phi^2$ (we're ignoring the periodicity for simplicity). Regardless, we obtain the transmission in a concise form:

$$\mathcal{T} = \frac{t_1^2 t_2^2}{\delta^2} \cdot \frac{1}{1 + \frac{4\phi^2}{\delta^2}} \tag{2.18}$$

Note that the fraction now has the exact shape of a Lorentzian! The full-width-half-maximum of this Lorentzian is $\Delta\phi = \delta$. Additionally, if we write that $r^2 = 1 - l^2$, where $l^2 = t^2 + a^2$ for each mirror and define $L \equiv l_1^2 + l_2^2$, then we can simplify even further: $\delta \approx L/2$. If we now remember that the free spectral range corresponds to $\Delta\phi = \pi$, we are able to define **Finesse** as the ratio between the FSR and FWHM:

$$\mathcal{F} \equiv \frac{\text{FSR}}{\text{FWHM}} = \frac{\pi}{\delta} = \frac{2\pi}{L} \tag{2.19}$$

It is important to note that the above treats the field inside of the cavity as a plane wave. An optical resonator will generally support a multitude of different optical modes that depend on its particular geometry. These modes will have an intrinsic geometry-dependent phase shift at the waist (Gouy shift), which will affect their absolute frequencies. However, the concepts of finesse and FSR still apply for modes existing in resonators that are much larger than the wavelength of light used.

2.2 SPECTRA AND SPECTRAL DENSITIES

In our work, we most often work with signals that are driven by random processes. Examples about: mechanical motion of our membrane transduced by light, RF signals with their intrinsic noise, etc. As it is well-known in experimental fields, looking at a signal in frequency domain is often much more enlightening than the picture of the same signal in time. Fourier transforms are a very useful tool in this regard, but their intrinsically complex output is often not needed, as we are interested in how much *power* a certain frequency band contains.

Fourier transforms and frequency spectra are a bit of a battleground when it comes to conventions on normalization. To avoid confusion, we will follow the same convention as is popular in our field, as evidenced by the theses of (Østfeldt 2022)(4) and (Nielsen 2016)(5). First, we define the Fourier transform and its corresponding inverse:

$$
\begin{aligned}
f(\omega) &\equiv \int_{-\infty}^{+\infty} f(t) e^{-i\omega t} dt \\
f(t) &\equiv \frac{1}{2\pi} \int_{-\infty}^{+\infty} f(\omega) e^{+i\omega t} d\omega,
\end{aligned}
$$

from which the energy spectral density is defined as

$$E_{ff} \equiv \left\| f(\omega) \right\|^2 . \tag{2.20}$$

An advantage of our convention is that to obtain the energy of a signal, it is only necessary to take its energy density's integral, without the need for a normalization constant.

Note that the energy spectral density (and power spectral density) can be equivalently defined as the Fourier transform of the signal's autocorrelation function, made possible by Wiener-Khinchin theorem. These definitions are more useful when a given signal has a finite total energy, but for signals with which we work (signals without a defined beginning or end), the *power* spectral density is a more important metric. First, we define a time-limited Fourier transform:

$$f_T(\omega) \equiv \int_{-T/2}^{+T/2} f(t) e^{-i\omega t} dt, \tag{2.21}$$

which then leads to our definition of the power spectral density (PSD):

$$S_{ff} = S_f \equiv \lim_{T\to\infty} \frac{1}{T} \left\| f_T(\omega) \right\|^2 . \tag{2.22}$$

Let us now list some properties of power spectral densities that make them especially useful:

1. Any real (as in "non-complex") signal will have a symmetric PSD. The definitions above are so-called "two-sided" power spectral densities, valid for both complex and real signals. For real signals, one can define a one-sided PSD simply as $2 \cdot S_f$, where integration is done on non-negative numbers only

2. PSDs lend themselves to easy averaging. Practically, if a stationary signal becomes decorrelated faster than the acquisition time for the PSD, one can safely acquire many spectra, and obtain an averaged spectrum with much less variance. This is possible due to the ergodic theorem.

(4) Christoffer Østfeldt (2022). "Quantum Optomechanics for Hybrid Spin-Membrane Entanglement". Niels Bohr Institute, Faculty of Science, University of Copenhagen.

(5) William Hvidtfelt Padkær Nielsen (2016). "Quantum Cavity Optomechanics with Phononic Bandgap Shielded Silicon Nitride Membranes". University of Copenhagen. 160 pp.

Note that complex signals do arise in certain circumstances, such as when one performs demodulation of an initially real signal. In that case, the power spectral density will be asymmetric.

In the same spirit, we can define an extension of power spectral densities: the *cross power spectral density* or *cross spectral density*, CSD for short:

$$S_{gf} \equiv \lim_{T \to \infty} \frac{1}{T} g_T^*(\omega) f_T(\omega). \tag{2.23}$$

The cross spectral density is a very useful tool to characterize whether two different signals are related, as it highlights correlated spectral components, while removing uncorrelated noise. We use CSDs extensively in our work on characterization of phase noise in delay line phase cancellation. The author believes that CSDs are underused in our field, and should be explored more often as a tool to uncover signals otherwise "buried" in noise.

2.3 PHOTODETECTION

Needless to say, photodetection is our everything. All the optical processes that we create in our experiments sooner or later end up in a photodetector, be it a superconducting single-photon detector, or a humble photodiode. It is then imperative to ask oneself the question, "given some input, what will the photodetector produce at its output?". Rigorous treatment of photodetection is a big topic on itself, for which we refer the reader to existing literature, such as (Walls and G. Milburn 2008), (Mandel and Wolf 1995), and others. We will instead list the results most important to us.

2.3.1 Shot noise

One of the simpler states of light, next to no light at all, is the coherent light. Coherent light is a pure sinusoidal wave at a single frequency, constant intensity, with no beginning or end. From the quantum optics perspective, it is an eigenstate of the annihilation operator:

$$\hat{a} \left|\alpha\right\rangle = \alpha \left|\alpha\right\rangle, \tag{2.24}$$

where α is this state's amplitude, possibly complex. As an experienced reader will know, its average photon number is simply $\langle \hat{a}^\dagger \hat{a} \rangle = \|\alpha\|^2$. However, it is not an eigenstate of the number operator $\hat{n} = \hat{a}^\dagger \hat{a}$, so its photon number will be fluctuating, with variance given by:

$$\langle \hat{n}^2 \rangle - \langle \hat{n} \rangle^2 = \langle \hat{n} \rangle \tag{2.25}$$

A little side-note: so far we have referred to operators that operate (sorry for the tautology) on some kind of mode where a total number of photons can be computed. It can be either a temporal mode, or a confined mode, such as one inside of an optical cavity. If one has to deal with *rates*, i.e. free-propagating fields that are defined in terms of how many photons per second arrive at the detector, a similar treatment applies (Mandel and Wolf

1995), but with a change of units such that, say, $\hat{a}$ has units of photons/$\sqrt{\text{time}}$, and additional care taken to include the fact that the detector is effectively sampling adjacent temporal modes that closely follow each other as they impinge on the detector(Mandel and Wolf 1995). The signal produced by the detector is then conceptually a series of "one-shot" measurements of small temporal segments.

The above variance should also be the result of integrating over the power spectral density produced by a photodetector (assuming output has been normalized to represent numbers of photons). Indeed, the PSD of photodetected current for a coherent state, which is the quantity that we measure, is simply:

$$S_i = \text{photon rate}. \tag{2.26}$$

The difference between measuring incoming free-propagating beams, and the more idealized confined field, is actually somewhat staggering, especially when representing PSDs of photocurrents. Again, we refer the reader to (Mandel and Wolf 1995) for a rigorous treatment.

2.3.2 Interferometry

While the main theme of this work is single-photon counting, homodyne and heterodyne interferometry still play an exceptionally important role for diagnostics, and past and future measurements that will involve continuous measurements of mechanical state. The most used kind of linear detection for us is homodyne interferometry, or homodyning for short. Homodyning allows one to measure extremely weak optical fields using normal non-photon-counting linear detectors, usually photodiodes. Note that it is not a substitute for true photon counting, as homodyning detects *quadratures* of the incoming field, i.e. linear superpositions of $\hat{a}$ and $\hat{a}^\dagger$ (properly normalized). Direct detection on the other hand, in particular photon counting, detects $\hat{a}^\dagger \hat{a}$, which is *quadratic* in the field strength, which can be used for "more quantum" protocols, such as heralding.

Homodyning and heterodyning both exploit the intrinsic non-linearity of photodetectors, as their output is quadratic in the field. Historically, both techniques stem from early advances in radio-frequency design, which are used even more widely in our information-age society.

And now, onto optics. The canonical version of homodyning or heterodyning consists of combining the signal of interest, possibly very weak, with a strong coherent drive using a 50:50 beamsplitter. The two beams overlap geometrically, so there will be interference on the two outputs of the beamsplitter. We shall call the strong coherent drive as *Local Oscillator*, or LO(6). In the regime where LO is much stronger than the signal, as is usually the case, and the phase between the two beams is known, the photocurrent output of the balanced photodetector will be (Bowen and G. J. Milburn 2015):

$$S_i^{\text{hom}}(\omega) = \|\alpha_{\text{LO}}\|^2 \, \bar{S}_{X^\theta}(\omega) \tag{2.27}$$

where the last spectral density is the symmetrized power spectral density of the signal quadrature:

(6) Again, coming from RF, where "local" means "at home inside your radio"

$$\hat{X}^{\theta} \equiv \frac{1}{\sqrt{2}}(\hat{a}^{\dagger}e^{i\theta} + \hat{a}e^{-i\theta}) \tag{2.28}$$

This last thing can correspond to phase, amplitude, or any combination of the two for the signal. θ is the phase angle between the signal and LO, which of course assumes that the signal has some coherent component. If there is no phase dependence (like for thermal light states, or number states, for example), then $\hat{X}$ will be independent of θ.

In case of heterodyne detection, we can detect all quadratures simultaneously, though that comes at the cost of doubling of shot noise's effect on the signal (Bowen and G. J. Milburn 2015).

What is important in the above is the increase of PSD of the signal with increased LO power, which allows one to overcome e.g. electronic noise in the detection system simply by increasing the LO level.

2.4 AFTERWORD

The topics presented above form a foundation for many of our basic techniques. More specific theory relevant to different experiments of this work is outlined in the corresponding chapters.

CHAPTER 3

MECHANICS

A lot of what we do has a classical description first and foremost, and only at the end displays quantum properties. This is why I believe that a introduction to good old classical mechanics is needed, especially focusing on harmonic oscillators. This topic is one of the first to be taught in any classical mechanics course, so we will not go into extreme details of derivations, as that is beautifully covered in many textbooks (Landau and Lifshitz 1976; Cassiday and Fowles 2005; Goldstein, Poole, and Safko 2001). However it is still important to cover some practical parts that are particularly useful to our experiment, such as the frequency response of oscillators under external forces, damping, etc. This will also ensure that we are speaking the same language. Without further ado, let us begin.

3.1 HARMONIC OSCILLATOR: TIME-DOMAIN DYNAMICS

Here we are: the humble harmonic oscillator. The workhorse (and sometimes scapegoat) of physics. Present, in one form or another, in nearly any physical phenomenon. From atomic transitions to planetary motion, from LIGO mirrors to levitated nanoparticles, from electromagnetic fields to civil engineering. This is all due to it being, perhaps, the simplest system beyond a system without any forces at all. In simple terms, whenever there is a force linearly proportional to some displacement, force that tends to bring the object towards its equilibrium point, a harmonic oscillator appears. Herein lies its power: most real-world forces, no matter how nonlinear over large distances, can be *linearly* approximated when displacements are small. Just as importantly, "force" need not be of the mechanical kind. Thanks to the achievements of classical mechanics giants such as Lagrange and Hamilton, it became possible to vastly generalize the concept of harmonic oscillators(1), and bring it to a vastness of other phenomena. All one needs is a system with two conjugate variables q and p (position and momentum, in mechanical terms), that obeys a simple Hamiltonian:

(1) and everything else

$$H = \frac{p^2}{2m} + \frac{1}{2}kq^2 \tag{3.1}$$

The constants m and k represent the mass and spring constant of a classical one-dimensional mass-spring system, but they need not be! As long as a system has two variables, and an energy quadratic in both, it will behave in the exact way in which a harmonic oscillator behaves. And just as easily, this can be generalized to a multi-dimensional case. From this hamiltonian, the equations of motion arise:(2)

$$m\ddot{q} + kq = 0 \tag{3.2}$$

The solution to this equation are simples sines and cosines: a peaceful and undisturbed oscillation. This is where we start adding spoonfuls of tar into our barrel of honey, as the world is not peaceful, and takes every opportunity to disturb the harmonic oscillator. The first such force is decay, or damping. As the harmonic oscillator inevitably interacts with the multitude of things around it, it starts to feel little kicks and nudges. Not to get too prosaic, many independent microscopic disturbances tend to drain the system of its energy, which from the point of view of the oscillator looks like *damping*: a velocity-dependent force counteracting its motion. This adds to our previous equation:

$$m\ddot{q} + \Gamma\dot{q} + kq = 0 \tag{3.3}$$

The new constant Γ is simply a proportionality factor that describes how strong the damping is. We shall now perform a familiar transformation, where the equation is divided by m, and some new constants are introduced to capture the dynamics in a clearer way:(3)

$$\ddot{q} + \eta\Omega_0\dot{q} + \Omega_0^2 q = 0 \tag{3.4}$$

Ω_0 is the natural frequency of the oscillator, that is, the frequency at which it would oscillate in absence of external influences or damping. Also note that we introduced a unitless constant η, which will characterize the "damping regime" in which the system operates. Making it unitless decouples it from the timescale, allowing us to compare e.g. oscillators with different frequencies.

We are now in position to look at some solutions of this system. I say "some" because for the very specific case of critical damping ($\eta = 1/2$), the solutions need a special treatment, which is not particularly useful for this thesis. But do review, for example, (Goldstein, Poole, and Safko 2001) for a comprehensive derivation. We will also omit the overdamped case, as we rarely encounter it in practice. Now, by setting $q = \exp(\lambda t)$, the differential equation becomes a quadratic one, with the following solution:

$$\lambda = -\frac{\eta\Omega_0}{2} \pm i\Omega_0\sqrt{1-(\eta/2)^2} \approx -\frac{\eta\Omega_0}{2} \pm i\Omega_0 \tag{3.5}$$

(2) As promised, we are skipping many derivation steps

(3) With the benefit of hindsight, as is usual in mathematics and physics. Somebody sat down and got that hindsight, so that we don't have to...

where the latter approximation is due to having a typical scenario in mind: $\eta \ll 1$. Then the solutions to the equation of motion are:

$$q = \exp\left(-\frac{\eta\Omega_0}{2} \cdot t\right) \cdot \exp(\pm i\Omega_0 t) \tag{3.6}$$

The first term is the decay of the oscillator's amplitude due to damping, while the second one describes the oscillations. Sidenote: the quantity is complex, but can be converted into a real physical quantity by taking the real part of it. This is due to the linearity of our system, which allows any arbitrary linear combination of its solutions to be a solution as well. Similarly, the solution can be multiplied by any complex number prior to taking the real part. Complex numbers are often easier to manage than sines and cosines, which is why we try to stick to them here.

We can now take a look at the *energy* evolution of the system under such decay. Now, a correct treatment would consider both the kinetic and potential energies. However, for the purpose of exposition, we will look only at a proportionality, which will allow us to make an important definition in a moment, without cluttering this work with derivations much better explained in textbooks. By taking the absolute value squared of the position, which is proportional to the energy, we obtain:

$$|q|^2 = \exp(-\eta\Omega_0 t) \tag{3.7}$$

As you can see, the energy of the system simply decays exponentially with a time constant of $\eta\Omega_0$. Here comes one of the most used definitions in our field, the Q-factor (often referred to simply as "The Q"):

$$Q \equiv \frac{1}{\eta} \tag{3.8}$$

See, I pulled a sneaky on ya! (4) It has been hiding in plain sight all this time. The Q is one of the most important parameters in optomechanical systems, as it quantifies how many oscillations can an oscillator perform, before its energy decays by a factor of e. All of the above will be enough for nearly all mechanics-related time-domain discussions in this work, so now we can proceed to a different view of the same phenomena: the frequency domain.

(4) Famous quote by Steve Ross (Bob Ross' son)

3.2 HARMONIC OSCILLATOR: FREQUENCY-DOMAIN BEHAVOUR

In our work, most of the time we use spectral techniques to analyze our systems, as it is undoubtedly convenient. And since we're dealing with harmonic oscillators all the time, let us look at how they behave in frequency. The approach here is very similar to the previous subchapter, except for the following:

- Instead of substituting complex quantities as a trial solution, we will start using Fourier transforms.
- We will now introduce an external driving force.

The equation of motion with an external force takes the following form:

$$\ddot{q} + \eta\Omega_0\dot{q} + \Omega_0^2 q = f(t), \tag{3.9}$$

where $f(t)$ is some time-dependent external force ($f(t) = F(t)/m$ for actual mechanical oscillators, F being the physical force applied). We now switch to the Fourier domain in the usual way, $t \to \omega$:

$$-\omega^2 q(\omega) - i\omega\eta\Omega_0 q(\omega) + \Omega_0^2 q(\omega) = f(\omega) \tag{3.10}$$

Just as before, we end up with an algebraic equation instead of a differential equation, readily solvable:

$$q(\omega) = \frac{1}{-\omega^2 - i\omega\eta\Omega_0 + \Omega_0^2} \cdot f(\omega) \tag{3.11}$$

This form is the complete solution, valid for all frequencies and dampings. However, most often we deal with high-Q systems, and are only interested in their behaviour near their resonance frequency. To see what I mean, let us first rewrite the denominator an a slighly more suggestive way (redefining again $\Gamma \equiv \Omega_0\eta$ and dropping the subscript in Ω_0 while we're at it):

$$-\omega^2 - i\omega\eta\Omega + \Omega^2 = -(\omega - \Omega)(\omega + \Omega) - i\omega\Gamma \tag{3.12}$$

This is still the previous form, but now let us make some very reasonable definitions and approximations. First, we define the *detuning*. It is such an important concept that it gets its own equation:

$$\Delta \equiv \omega - \Omega \tag{3.13}$$

We will be interested in regimes where this detuning is on the order of Γ, and $\Gamma \ll \Omega$. This allows one to approximate $\omega\Gamma \approx \Omega\Gamma$, and $\omega + \Omega \approx 2\Omega$. Before mathematicians get angry, let me tell you that a more formal approach with Taylor expansions yields the same result, it's just a bit more "visual" to do it our way. With these approximations and some algebra, Eq. (3.11) becomes

$$q(\omega) = \frac{-f(\omega)}{2\Omega\Delta + i\Gamma\Omega} = \frac{-i\Gamma\Omega \cdot f(\omega)}{1 - 2i\Delta/\Gamma} \tag{3.14}$$

See where I'm going? We're arriving at the definition of a Lorentzian! As a matter of fact, $1/(1 - 2i\Delta/\Gamma)$ is the complex Lorentzian, and appears very often in our work, whenever complex response (i.e. response containing phase information) is necessary. We shall provide a proper definition of the complex Lorentzian later, closer to where it's used. However, The Lorentzian, its absolute squared relative, is important enough to define here:

$$L(\Delta; \Gamma) \equiv \frac{1}{1 + (2\Delta/\Gamma)^2} \tag{3.15}$$

CHAPTER 4

OPTOMECHANICS

We have finally reached the point where we can talk about optomechanics, both in the classical and quantum domains. There exist several excellent introduction resources on this topic, such as Aspelmeyer, Kippenberg, and F. Marquardt (2014)(1) and Bowen and G. J. Milburn (2015)(2). Therefore, we will not list all the derivations, and will instead give priority to results that shape this work's approach. However, we will still outline the founding ideas, as I find them illuminating and pedagogical.

Optomechanics has two meanings: "interaction between optical and mechanical phenomena" and "engineering of mechanical devices for control of light". The two definitions look somewhat alike, but in practice the latter refers to the manufacture of fixtures, mounts, optical breadboards, etc. The former, however, is our area of physics, where try to harvest the fundamental mechanical properties of light and matter, and use them to our advantage. We will now descibe several ways in which light can interact with a mechanical object, in order of increasing complexity.

4.1 FREE-PROPAGATING LIGHT AND FREE-FLOATING MASS

Let us consider a simple scenario: a 1 kg retroreflector mirror floating somewhere in intergalactic space, with no forces to perturb it, in an almost perfect vacuum. We are floating some distance away, enough for our gravitational attraction not to affect this mirror too much. We can't quite see the mirror, as it is dark around. So we fire up our 1 W, 1 µm-wavelength laser and start sweeping it across the sky, until we suddenly get a reflection on our detector. We found the mirror! We send a couple of lidar pulses, and determine that the mirror is not moving to the best of our knowledge. However, we would now like to track it precisely. So we take our continuous laser, point it precisely at the mirror, and get a return signal that we send to a homodyne setup, shown in Fig. 4.1. Now we can determine the position of this mirror quite precisely, with the ultimate limit set by light shot noise (more on that later). But we soon see that something is happening: the inter-

(1) Markus Aspelmeyer, Tobias J. Kippenberg, and Florian Marquardt (Dec. 2014). "Cavity Optomechanics". In: *Reviews of Modern Physics* 86.4, pp. 1391–1452. ISSN: 0034-6861. DOI: 10.1103/RevModPhys.86.1391. URL: https://link.aps.org/doi/10.1103/RevModPhys.86.1391.

(2) Warwick P. Bowen and Gerard J. Milburn (Dec. 2, 2015). *Quantum Optomechanics*. Boca Raton: CRC Press. 376 pp. ISBN: 978-0-429-15931-2. DOI: 10.1201/b19379. URL: https://doi.org/10.1201/b19379.

ference pattern starts to shift faster and faster, indicating that the mirror is accelerating away from us. This is the pressure of light, which hits the mirror and reverses its direction, producing a constant force of $F = 2P/c$, with P being the power of the incoming beam, and c the speed of light.

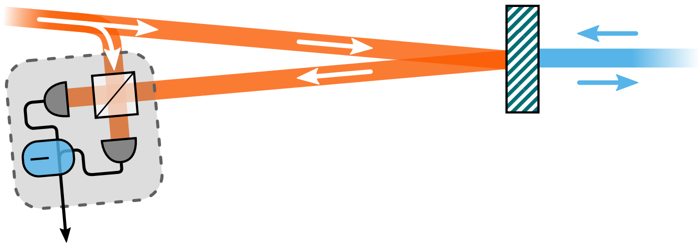

Figure 4.1: Schematic of the thought experiment with a free mass in space

This phenomenon is, of course, nothing new to us, as we are a space-faring civilization. So we quickly ask our friends on the other side, opposite to the mirror, to send a laser beam of their own to first counteract the speed of the mirror, and then set it to be exactly equal to the power of our beam. The mirror predictably stops its motion relative to us and our friends, and now we don't need to worry about it running away. We then continue our measurements. Since the equation of motion of a free mass is simply Newton's second law, $\ddot{x} = F(t)/m$, we know how our light will affect the mirror's motion. Let us disregard the effect that our friend's lasers' shot noise has on the mirror for simplicity, and only concern ourselves with our own shot noise. Remember that the coherent light produced by our laser is not completely constant: shot noise is present in both its amplitude and phase. The floating mirror only responds to amplitude, i.e. intensity. If we convert the equation of motion into its double-sided spectral density form, and use the spectral density form of shot noise, then we obtain:

$$S_{xx}(\omega) = \frac{2(h\nu)P}{mc} \cdot \frac{1}{\omega^4} \tag{4.1}$$

A small caveat: this expression is unbounded for $\omega = 0$. Remember, however, that we agreed with our friends to keep the free-floating mirror stable, which effectively translates into cancelling such low-frequency effects below a certain frequency ϵ. If we now want to know the variance of mirror position, it's a simple manner of integrating. Remembering that this is a double-sided spectral density, we get

$$2\int_{\epsilon}^{\infty} S_{xx}(\omega)\,d\omega = \frac{12(h\nu)P}{mc \cdot \epsilon^3} \tag{4.2}$$

A quick order-of-magnitude estimate with our parameters and $\epsilon = 10\,\text{Hz}$ leads us to have rms variations in the mirror's position on the order of femtometers. That might sound insignificant, but it is precisely the precision level at which gravitational wave detectors such as LIGO operate, with spectral densities of end-mirror positions of $\approx 1\times10^{-16}\,\mathrm{m}/\sqrt{\mathrm{Hz}}$. The important message here is that light randomly perturbs the motion of the mechanical object. And while the shot noise's influence on the detected signal *decreases*, the shot noise *increases the position fluctuations themselves!* This in itself is rather fascinating, especially given the fact that our experiments routinely observe effects that stem directly from shot noise perturbations on mechanical motion, which we shall refer to as *backaction*.

As a sidenote, we might ask ourselves whether there exists an optimal optical power if all we want to do is to measure the position of a mechanical object. That point does indeed exist, and it is famously(3) called the *Standard Quantum Limit*, or SQL*not related to Standard Query Language of computer databases* for short. At that limit, the backaction (which directly affects the mass) and the imprecision (which only affects the measurement, and not the mass) are equal in magnitude. In case of optomechanics with harmonic oscillators, which covers the regime of the vast majority of current experiments, SQL results in an effective added energy of $\hbar\Omega_\mathrm{m}/2$, of which half is physically added to the oscillator, and the other half is due to measurement imprecision (Aspelmeyer, Kippenberg, and F. Marquardt 2014)(4). Gravitational wave detectors are a notorious exception, where mirror motion is much slower than the timescale of gravitational waves, so mirrors can be considered to be free masses, and a modified treatment yields the free-mass SQL of $\sqrt{\hbar\tau/m}$, with τ being the measurement interval (Bowen and G. J. Milburn 2015)(5).

4.2 FREE LIGHT AND HARMONIC OSCILLATOR

We're getting a bit closer to our goal, so let us make another change to our model. We're still in outer space, but this time the mirror is on a spring (a pendulum would work if there was gravity, which there isn't). Let's say the spring is attached to something relatively immovable, like an asteroid that we conveniently brought with us, or a rock (Fig. 4.2).

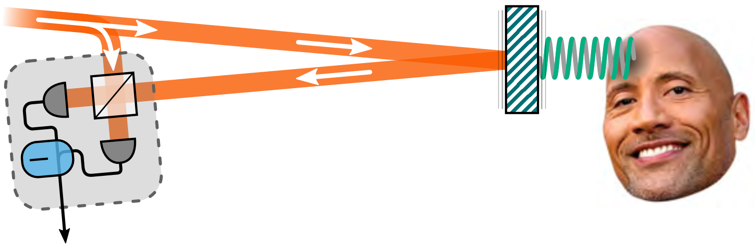

Figure 4.2: Schematic of the thought experiment with a harmonic oscillator in space, attached to a massive rock (Dwaine "The Rock" Johnson).

And let there be a bit of damping, perhaps from the spring itself, but not too much so that we stay in the weak damping regime ($\Gamma \ll \Omega$). As described in the chapter on mechanical oscillators, the equation of motion of such an oscillator in frequency domain is as follows:

$$-\omega^2 x(\omega) + i\omega\Gamma_\mathrm{m} x(\omega) + \Omega^2 x(\omega) = F(\omega)/m \tag{4.3}$$

(3) in our narrow field

(4) Markus Aspelmeyer, Tobias J. Kippenberg, and Florian Marquardt (Dec. 2014). "Cavity Optomechanics". In: *Reviews of Modern Physics* 86.4, pp. 1391–1452. ISSN: 0034-6861. DOI: 10.1103/RevModPhys.86.1391. URL: https://link.aps.org/doi/10.1103/RevModPhys.86.1391.

(5) Warwick P. Bowen and Gerard J. Milburn (Dec. 2, 2015). *Quantum Optomechanics*. Boca Raton: CRC Press. 376 pp. ISBN: 978-0-429-15931-2. DOI: 10.1201/b19379. URL: https://doi.org/10.1201/b19379.

where we adopt the notation of Aspelmeyer, Kippenberg, and F. Marquardt (2014) for Γ_m. Let us introduce the more general concept of *mechanical susceptibility*, which is nothing else than the response of mechanical position to an external force in frequency domain (Aspelmeyer, Kippenberg, and F. Marquardt 2014):

$$\chi_m = \frac{1}{m(\Omega_m^2 - \omega^2) - im\Gamma_m\omega} \tag{4.4}$$

The driving force, i.e. shot noise, is still as in the previous example of a free mass. We are also still disregarding the offset produced by the dc part of the light beam. This time, however, the transduction function has changed. Additionally, because we have agreed on the condition of very weak damping, we will approximate the response of the oscillator as a complex Lorentzian:

$$\chi_m \approx \frac{i}{\Gamma_m\Omega_m} \cdot \frac{1}{1 - \frac{2i\Delta_m}{\Gamma_m}}, \tag{4.5}$$

where we have defined $\Delta_m \equiv \omega - \Omega_m$ to be the mechanical detuning.

If we now translate the above into the language of power spectral densities (by multiplying χ_m by its complex conjugate), it should be evident that the mechanical motion spectrum under the action of shot noise (which is entirely flat over the whole frequency range) will be a Lorentzian as well.

For more worked-out examples for the harmonic oscillator and free masses, we refer the reader to the very thorough work of Bowen and G. J. Milburn (2015).

4.3 Confined light and harmonic oscillator: introduction

One problem with the above approaches is that of waste: light only has one chance to interact with the mechanical system, necessitating a substantial optical power for precise measurements. This is where *cavity optomechanics* finally enters the picture: we use optical techniques that allow the light to recirculate, allowing it to interact with the mirror multiple times. In modern optical devices, this can be done in a multitude of ways, but the core idea is the same: construct an optical resonator interfaced to the mechanical object in question. We shall now talk about an exceptionally useful model that captures the dynamics of most optomechanical systems: the "canonical optomechanical model".

The canonical optomechanical model consists of a two-mirror optical cavity, where one of the mirrors is allowed to move as a harmonic oscillator around its equilibrium position. This motion corresponds to changes in the length of the cavity, i.e. changes of the resonance frequency of the cavity. In the vast majority of experimental cases, such changes are only a tiny portion of the wavelength of light, and we will only consider the following linear expansion, following notation in Aspelmeyer, Kippenberg, and F. Marquardt (2014):

$$\omega_{\mathrm{cav}}(x) = \omega_{\mathrm{cav}}^{(0)} + x \cdot \frac{\partial \omega_{\mathrm{cav}}}{\partial x} \tag{4.6}$$

where x is the displacement of the mirror, and $\omega_{\mathrm{cav}}^{(0)}$ is the "default" cavity resonance frequency. We shall define a quantity called G that characterizes the changes of cavity frequency with respect to displacement. In the case of the canonical model:

$$G \equiv -\frac{\partial \omega_{\mathrm{cav}}}{\partial x} = -\frac{\partial}{\partial L}\frac{cn}{2L} = \omega_{\mathrm{cav}}\frac{1}{L} \tag{4.7}$$

where n is the mode number of a particular resonance (although it's inconsequential in the final result). You can see one important point already: for a canonical system, the coupling strength decreases with an increase of cavity length. This is one of the reasons why we prefer increasing the mirrors' reflectivities instead of increasing the cavity length, when a narrow linewidth is required. G is a fine metric for a system, but it's usually a bit cumbersome to use in case of quantum experiments, as it doesn't encapsulate any properties of the mechanical oscillator, and for us has wild magnitudes on the order of 100 THz/m. For this reason, we define another quantity named "single-phonon coupling strength"(6) or g_0. By remembering that any harmonic oscillator has an associated amplitude of zero-point motion x_{zpf}, we can arrive at a more relevant definition:

$$g_0 \equiv G \cdot x_{\mathrm{zpf}} = G \cdot \sqrt{\frac{\hbar}{2m_{\mathrm{eff}}\Omega_m}} \tag{4.8}$$

we're using the concept of "effective mass" m_{eff}. This definition allows us to compare different systems, including those where it's not initially clear what constitutes a "free mirror" and how to measure displacements, for example microresonators where it's the whole structure that is both the optical cavity and the mechanical oscillator. Contrary to G that has SI units of Hz/m, g_0 has units of Hz. Jumping a bit ahead, our membrane-in-the-middle systems have values of $|g_0|$ ranging between 5 Hz and 100 Hz approximately, depending on the construction(7) of the cavity used.

4.4 QUANTUM-OPTOMECHANICAL EQUATIONS OF MOTION

We shall now dive deeper into a proper description of an optomechanical system, again following Aspelmeyer, Kippenberg, and F. Marquardt (2014). First, let us describe the dynamics of an optical cavity, without mechanics for now. We shall be focusing on only one optical mode (e.g. one of the optical resonances of a Fabry-Pérot cavity). If the cavity is absolutely lossless, its Hamiltonian will be rather simple:

$$\hat{H} = \hbar\omega_{\mathrm{cav}} \cdot \hat{a}^\dagger \hat{a} \tag{4.9}$$

(6) Sometimes called "single-photon coupling strength". The author prefers "phonon" in this context, as the definition specifically uses the *mechanical* zero-point motion

(7) essentially length

Cavities are unfortunately never lossless. These losses can be "good", for example those that allow the intracavity field to leak-out and be used for something else, or allow external laser light to be pumped into the cavity. They can also be "bad", i.e. irreversible losses due to light absorption, scattering, and so on. These effects can be used in the Hamiltonian formulation in the following way:

$$\hat{H}_{\text{test}} = \hbar\omega_{\text{cav}} \cdot \hat{a}^{\dagger}\hat{a} + \hat{H}_{\text{bath}} + \hat{H}_{\text{coupling}} \tag{4.10}$$

The common effect of these Hamiltonians is a bit more evident after using the quantum Langevin approach to open systems outlined in Bowen and G. J. Milburn (2015), where the bath is assumed to be a large collection of harmonic oscillators, and is then traced out (as by definition we're not able to track the quantum state of such a bath). We then arrive at the following equation of motion for the intracavity field:

$$\frac{\partial}{\partial t}\hat{a} = -\frac{\kappa}{2}\hat{a} + \sqrt{\kappa_{\text{ext}}}\,\hat{a}_{\text{input}}(t) + \sqrt{\kappa_0}\,\hat{f}_{\text{loss}}(t), \tag{4.11}$$

where $\kappa = \kappa_{\text{ext}} + \kappa_0$ is the total decay rate. In the language of optical cavities, κ is the full-width-half-maximum in radial units, κ_0 is the irreversible loss (bad), and κ_{ext} is the coupling to the external world, e.g. due to transmission through the mirrors (good). More often than not, $\hat{a}_{\text{input}}$ is a strong drive (typically coherent) with small quantum fluctuations overimposed on it(8). Without loss of generality, we can write

(8) slight abuse of notation, as $\hat{a}_{\text{input}}$ and $\hat{f}_{\text{loss}}$ stem from a continuous-mode treatment of travelling fields, and has units of $1/\sqrt{Hz}$, while $\hat{a}$ is a more textbook operator for a confined mode, and is unitless

$$\hat{a}_{\text{input}} = e^{i\omega_L t} \cdot (\alpha + \delta\hat{a}_i), \tag{4.12}$$

where ω_L is the driving frequency of the laser. This is a good moment to transform our dynamics into a frame rotating with the laser frequency (Bowen and G. J. Milburn 2015), which then converts Eq. (4.11) into:

$$\frac{\partial}{\partial t}\hat{a} = \left(-\frac{\kappa}{2} + i\Delta\right)\hat{a} + \sqrt{\kappa_{\text{ext}}}\,(\alpha + \delta\hat{a}_i) + \sqrt{\kappa_0}\,\hat{f}_{\text{loss}} \tag{4.13}$$

with the usual definition of $\Delta = \omega_L - \omega_{\text{cav}}$.

Let's spice things up a little by adding the mechanical oscillator. We will take a step back and look at the hamiltonian again, except this time we will add the hamiltonian of the harmonic oscillator, and remember than $\omega_{\text{cav}} = \omega^0_{\text{cav}} + Gx$, with x being the position of the mechanics

$$\begin{aligned}\hat{H}_{\text{OM}} &= \hbar(\omega_{\text{cav}} + G\hat{x}) \cdot \hat{a}^{\dagger}\hat{a} + \hbar\Omega_m \cdot \hat{b}^{\dagger}\hat{b} \\ &= \hbar\omega_{\text{cav}} \cdot \hat{a}^{\dagger}\hat{a} + \hbar\Omega_m \cdot \hat{b}^{\dagger}\hat{b} + \hbar g_0(\hat{b} + \hat{b}^{\dagger})\hat{a}^{\dagger}\hat{a}\end{aligned} \tag{4.14}$$

Note the last term, which is the interaction between mechanics and optics. One could even call it optomechanics! In any case, that interaction is fundamentally nonlinear (which is the reason why an optomechanical system can scatter photons to different frequencies). With that said, in the vast majority of experiments, including ours, a large number of intracavity photons is needed for any measurable interaction. By again writing $\hat{a} = \alpha + \delta\hat{a}$, and $\hat{b} = \delta\hat{b}$

(purely notational to highlight the fact that we assume small mechanical fluctuations), the interaction term above becomes linearized:

$$\hat{H}_I = \hbar g_0(\delta\hat{b} + \delta\hat{b}^\dagger)(\alpha + \delta\hat{a}^\dagger)(\alpha + \delta\hat{a}) \tag{4.15}$$

$$= \hbar g_0\alpha^2(\delta\hat{b} + \delta\hat{b}^\dagger) + \hbar g_0\alpha(\delta\hat{b} + \delta\hat{b}^\dagger)(\delta\hat{a} + \delta\hat{a}^\dagger) \tag{4.16}$$

where we disregarded higher-order interaction terms, as they are dominated by second-order terms, and defined α to be real without loss of generality. The first term is the optical spring effect, which we typically ignore in quantum dynamics. The second term is the important one: it characterizes the actual photon-phonon processes occuring in the optomechanical system. For now, this is a general interaction term that does not include the specifics of either sideband-resolved or unresolved operation, which we will cover next.

4.5 THEORY OF SINGLE-PHONON INTERACTIONS

We shall now closely follow the results of Galland et al. (2014), especially those presented in its supplementary material. As stated there, and in Woolley and Clerk (2013), we make the following ansatz. This essentially separates the intracavity field into three components: resonant light $\hat{a}_0$ (detuning of 0), and light on either the "red" side of the cavity resonance ($\hat{a}^-$), or the "blue" side ($\hat{a}^+$). We take those sidebands to be Ω_m away from the cavity resonance, as shown in Fig. 4.3, as in the sideband-resolved regime exactly these detunings will be relevant for all of our operations.

$$\hat{a}(t) = \hat{a}_0(t) + \hat{a}_\pm(t)e^{\mp i\Omega_m t} \tag{4.17}$$

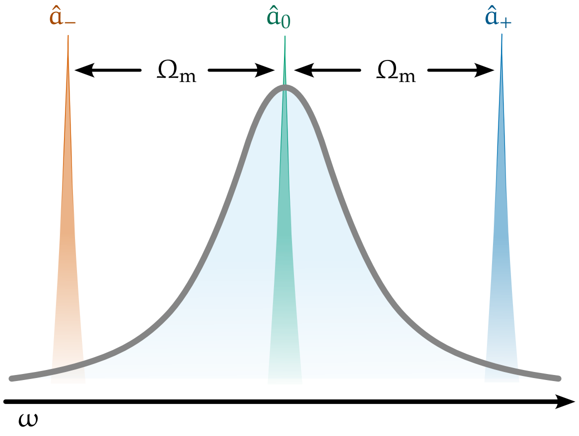

Figure 4.3: Convention on naming of fields in Galland et al. (2014)

By using the above ansatz with Eq. (4.14), one obtains a set of equations(9):

(9) note slight change of notation, as we are following a different work

$$\frac{\partial \hat{a}_0}{\partial t} = i g_0 (\hat{a}_- \hat{b}_0 + \hat{a}_+ \hat{b}_0) - \frac{\kappa}{2} \hat{a}_0 \tag{4.18}$$

$$\frac{\partial \hat{b}_0}{\partial t} = i g_0 (\hat{a}_0 \hat{a}_+ + \hat{a}_- \hat{a}_0) - \frac{\gamma}{2} \hat{b}_0 \tag{4.19}$$

$$\frac{\partial \hat{a}_+}{\partial t} = i g_0 \hat{a}_0 \hat{b}_0 - i s_+ - \left(\frac{\kappa}{2} - i\Omega_m\right) \hat{a}_+ \tag{4.20}$$

$$\frac{\partial \hat{a}_-}{\partial t} = i g_0 \hat{a}_0 \hat{b}_0 - i s_- - \left(\frac{\kappa}{2} + i\Omega_m\right) \hat{a}_- \tag{4.21}$$

where $s_\pm$ are driving terms. Usually only one of the drives is active (either red or blue), so we need not worry about them interfering. Just like in Galland et al. (2014), we linearize the above (fundamentally non-linear) equations, and notice that we drive the system on either the red or the blue side. Therefore, in the resolved regime we only concern ourselves with the scattering from the drive into the main mode of the cavity, $\hat{a}_0$. Additionally, in our experiment, there are many places where we can disregard the mechanical decay rate γ as it's much smaller than any other relevant rate in the system ($\gamma < 50\,\mathrm{mHz}$). The resulting equations, together with the noise that is driving the system (optical and mechanical decay) can be rewritten in matrix form as

$$\frac{\partial}{\partial t} \hat{\mathbf{A}} = M \hat{\mathbf{A}} + \hat{\mathbf{N}} \tag{4.22}$$

or

$$\frac{\partial}{\partial t} \begin{pmatrix} \hat{a} \\ \hat{a}^\dagger \\ \hat{b} \\ \hat{b}^\dagger \end{pmatrix} = \begin{pmatrix} -\kappa/2 & 0 & i g_- & i g_+ \\ 0 & -\kappa/2 & -i g_+ & -i g_- \\ i g_- & i g_+ & -\gamma/2 & 0 \\ -i g_+ & -i g_- & 0 & -\gamma/2 \end{pmatrix} \cdot \begin{pmatrix} \hat{a} \\ \hat{a}^\dagger \\ \hat{b} \\ \hat{b}^\dagger \end{pmatrix} + \begin{pmatrix} \sqrt{\kappa}\, \hat{a}_{in} \\ \sqrt{\kappa}\, \hat{a}_{in}^\dagger \\ \sqrt{\gamma}\, \hat{b}_{in} \\ \sqrt{\gamma}\, \hat{b}_{in}^\dagger \end{pmatrix} \tag{4.23}$$

where we have defined $g_\pm \equiv g_0 s_\pm$ to be the optomechanical coupling rates. The system of equations above captures all the relevant dynamics of the system. Solving it is not trivial, but not impossible either. The sequence of actions that Galland et al. (2014) use is outlined below:

- Diagonalize the system above to uncouple the equations.
- Symbolically solve the uncoupled equations to express $\hat{\mathbf{A}}$ in terms of time integrals of $\hat{\mathbf{N}}$ (with proper change of basis)
- From the noise properties of $\hat{a}_{in}$ and $\hat{b}_{in}$, namely:

  $$\langle \hat{a}_{in}(t_1) \hat{a}_{in}^\dagger(t_2) \rangle = \kappa \cdot \delta(t_2 - t_1) \tag{4.24}$$

  $$\langle \hat{b}_{in}(t_1) \hat{b}_{in}^\dagger(t_2) \rangle = \gamma(\bar{n}_{th} + 1) \cdot \delta(t_2 - t_1) \tag{4.25}$$

  $$\langle \hat{b}_{in}^\dagger(t_1) \hat{b}_{in}(t_2) \rangle = \gamma \bar{n}_{th} \cdot \delta(t_2 - t_1), \tag{4.26}$$

  we calculate the corresponding correlations, and cross-correlations, of $\hat{a}$ and $\hat{b}$.

We have performed these calculations, and took into account the simplifications that our experiment allows. To remind the reader, these simplifications are due to the fact that $\gamma \ll \{g_-, g_+\} \ll \kappa$. Without going into the process of calculations themselves, we instead will focus on one example.

Assuming that only the read light is active (i.e. $g_+ = 0$), corresponding the a beamsplitter interaction, we can compute the autocorrelation $\langle \hat{a}^\dagger \hat{a} \rangle$. Note that we're considering the *intra*cavity field, as the result is slightly different for the field that eventually gets picked up by the detector. Here is the autocorrelation in the steady-state regime:

$$\langle \hat{a}^\dagger(t_0 + t)\hat{a}(t_0)\rangle = \exp(-\kappa|t|/2) + \gamma\bar{n}_{th} \cdot \exp\left(\frac{-2g_-^2|t|}{\kappa}\right) \tag{4.27}$$

$$= \exp(-\kappa|t|/2) + \gamma\bar{n}_{th} \cdot \exp\left(-\frac{\Gamma_{opt}|t|}{2}\right) \tag{4.28}$$

Where in the last equality we used the expression for Γ_{opt} in the sideband-resolved regime. Note the prominent appearance of the mechanical term: that's the phonons being transformed into photons!

Let us now skip ahead to the main results of Galland et al. (2014), which will be the the main guidelines for our single-photon experiments. We will just change the notation a little bit and define $\Gamma = 4g^2/\kappa$, which corresponds to optical broadening when red-detuned, and to the exponential growth factor when blue-detuned. With this, we follow Hofer et al. (2011) and Galland et al. (2014) and introduce temporal optical read modes:

$$\hat{A}_{r,in}(t) = \sqrt{\frac{\Gamma}{e^{\Gamma t} - 1}} \int_0^t dt' \cdot e^{\Gamma t'/2} \hat{a}_{r,in}(t') \tag{4.29}$$

$$\hat{A}_{r,out}(t) = \sqrt{\frac{\Gamma}{1 - e^{-\Gamma t}}} \int_0^t dt' \cdot e^{-\Gamma t'/2} \hat{a}_{r,out}(t') \tag{4.30}$$

and similarly for the write modes,

$$\hat{A}_{w,in}(t) = \sqrt{\frac{\Gamma}{1 - e^{-\Gamma t}}} \int_0^t dt' \cdot e^{-\Gamma t'/2} \hat{a}_{w,in}(t') \tag{4.31}$$

$$\hat{A}_{w,out}(t) = \sqrt{\frac{\Gamma}{e^{\Gamma t} - 1}} \int_0^t dt' \cdot e^{\Gamma t'/2} \hat{a}_{w,out}(t') \tag{4.32}$$

All of these modes are based on eigensolutions to the Langevin equations for this system after adiabatic elimination has been performed. These modes are also the ones that will contain the photons of interest.

Now we turn our attention to the state evolution in the context of counting. Our initial conditions are the following:

- Mechanical oscillator in thermal state with occupation $\bar{n}_{th} \ll 1$, brought there by optical cooling.

- No photons in the cavity.

In this state, the mechanical oscillator is, more specifically, in a mixed state given by

$$\hat{\rho} = (1-p)\sum_{n=0}^{\infty} p^n \left|n\right\rangle \left\langle n\right| \tag{4.33}$$

where p is defined in a conventional way as

$$p \equiv \frac{\bar{n}_{th}}{1+\bar{n}_{th}} \tag{4.34}$$

Now we turn on the writing pulse for a time T_w. During that time, a certain number of photons is emitted into the cavity (and an equal number of phonons is created in the mechanical oscillator), given by:

$$N_{herald} = (e^{\Gamma T_w}) \cdot (\bar{n}_{th} + 1) \tag{4.35}$$

After detecting a photon (that inevitably leaks out of the cavity since κ is so much bigger than all other rates in the system), the system gets projected into a (hopefully) non-classical state given by the conditional density matrix

$$(1-\bar{p}) \cdot \sum_{n=0}^{\infty} \bar{p}^2 (n+1) \left|n+1\right\rangle \left\langle n+1\right| \tag{4.36}$$

where we have defined $\bar{p} \equiv p \cdot \exp(-\Gamma T_w)$. For small enough $\bar{p}$, this state approaches a single-phonon state, which is the reason why whenever we choose a write pulse strength (and/or duration), we tend to the weaker side to make $\bar{p}$ as small as experimentally feasible, with considerations of noise and acquisition time. More on that in the experimental section, especially in Chapter 10.

4.6 PRACTICAL OPTOMECHANICAL THEORY

For now, all that is left to do is to present some more results that are very useful in everyday calculations, but without much proof. As before, we refer the reader to (Aspelmeyer, Kippenberg, and F. Marquardt 2014) and (Bowen and G. J. Milburn 2015), from which most of these results were adapted.

One of the most important experimental metrics is the optomechanical broadening. It is easy to measure both using OMIT (covered later in Chapter 6), or by observing spectral densities. Optomechanical broadening in a general case is given by the following expression:

$$\begin{aligned}\Gamma_{opt} &= \bar{n}_{cav} g_0^2 \left(\frac{\kappa}{\kappa^2/4 + (\Delta+\Omega_m)^2} - \frac{\kappa}{\kappa^2/4 + (\Delta-\Omega_m)^2} \right) \\ &= \frac{4\bar{n}_{cav} g_0^2}{\kappa} \cdot \left(L\left(\Delta+\Omega_m;\kappa\right) - L\left(\Delta-\Omega_m;\kappa\right)\right) \end{aligned} \tag{4.37}$$

Note an interesting fact: Γ_{opt} can be negative or positive. When it's positive, which happens when the laser is red-detuned with respect to the cavity, it is broadening in the full sense: the measured spectrum of mechanical motion will be $\Gamma_{\mathrm{eff}} = \Gamma_{\mathrm{opt}} + \Gamma_{\mathrm{m}} \geqslant \Gamma_{\mathrm{m}}$. When it is negative, however, it is possible to reach regimes where $\Gamma_{\mathrm{eff}} \leqslant 0$. In that case, what happens is an exponential growth of energy in the mechanical oscillator. In our experimental case, Γ_{m} is very small, so for us it is difficult **not** to excite the membrane in the blue-detuned regime, even if the blue detuning is almost negligible.

It is quite useful to distinguish between sideband-resolved ($\kappa \ll \Omega_{\mathrm{m}}$) and sideband-unresolved ($\kappa \gg \Omega_{\mathrm{m}}$) regimes. In the sideband-resolved regime, when we are red-detuned by Ω_{m}, the broadening takes a simple form:

$$\Gamma_{\mathrm{opt}}^{(\kappa \ll \Omega_{\mathrm{m}})} \longrightarrow \frac{4\bar{n}_{\mathrm{cav}} g_0^2}{\kappa} \tag{4.38}$$

Likewise, in the sideband-unresolved regime, when we are red-detuned by $\kappa/2$, the broadening is:

$$\Gamma_{\mathrm{opt}}^{(\kappa \gg \Omega_{\mathrm{m}})} \longrightarrow \frac{4\bar{n}_{\mathrm{cav}} g_0^2}{\kappa} \cdot \frac{2\Omega_{\mathrm{m}}}{\kappa}, \tag{4.39}$$

where the factorization was done to emphasize the parallel to the sideband-resolved case. An important note to make here is to realize that *broadening* does not necessarily reflect the *coupling strength*, as it is possible to be exactly resonant with the cavity, where $\Gamma_{\mathrm{opt}} = 0$, but the coupling is still strong. This regime is where, for example, QND measurements are often done.

Another important quantity for us is the mechanical occupation that we can reach, given a certain broadening. In a general case, but in absence of extra noise, this occupation is given by:

$$\bar{n}_{\mathrm{m}} = \frac{\Gamma_{\mathrm{opt}} \bar{n}_{\mathrm{min}} + \Gamma_{\mathrm{m}} \bar{n}_{\mathrm{th}}}{\Gamma_{\mathrm{opt}} + \Gamma_{\mathrm{m}}} \approx \bar{n}_{\mathrm{min}} + \frac{\Gamma_{\mathrm{m}} \bar{n}_{\mathrm{th}}}{\Gamma_{\mathrm{opt}}} \tag{4.40}$$

where in turn $\bar{n}_{\mathrm{min}}$ is defined by the sideband resolution regime. It is equal to $(\kappa/\Omega_{\mathrm{m}})^2/16$ in sideband-resolved regime, where the optimal detuning has been chosen. In the unresolved regime, the best attainable occupation is, on the other hand, equal to $\bar{n}_{\mathrm{min}} = \kappa/(4\Omega_{\mathrm{m}})$,

On that note, let us look at this optimal detuning. For any regime of operation, both resolved-sideband and unresolved-sideband, there exists an optimal detuning that minimizes $\bar{n}_{\mathrm{min}}$, and is given by:

$$\Delta_{\mathrm{optimal}} = \sqrt{\kappa^2/4 + \Omega_{\mathrm{m}}^2} \tag{4.41}$$

As a fun little exercise, we can find approximations to this optimal detuning. Remember that in the case of sideband-resolved operation, $\kappa \ll \Omega_{\mathrm{m}}$. In the sideband-unresolved regime, the opposite is true. Therefore,

$$\Delta_{\mathrm{optimal}} \approx \Omega_{\mathrm{m}} + \frac{\kappa^2}{8\Omega_{\mathrm{m}}} \text{ (resolved)} \tag{4.42}$$

$$\Delta_{\mathrm{optimal}} \approx \frac{\kappa}{2} + \frac{\Omega_{\mathrm{m}}^2}{\kappa} \quad \text{(unresolved)} \tag{4.43}$$

4.7 TRANSITION RATES IN EQUILIBRIUM

In addition to the previous results, it is highly useful to calculate the intensity of sidebands leaving the cavity. This provides intuition on what to expect during either photon counting, or heterodyne/homodyne detection. Transition rates can be calculated from the requirement of equilibrium and detailed balance (Aspelmeyer, Kippenberg, and F. Marquardt 2014). These requirements lead to the following

$$(\bar{n}+1)(A^+ + A^+_{th}) = \bar{n}(A^- + A^-_{th}) \tag{4.44}$$

A^+ corresponds to the process of scattering photons towards the red sideband, i.e. a process that *increases* the number of phonons (note: it is suppressed in red-detuned resolved sideband regime). Inversely, A^- corresponds to the cooling process. The A coefficients are rates in the quantum mechanical sense. To obtain the actual numbers of photons in the sidebands, we have to multiply them by $\bar{n}$:

$$n_+ = (\bar{n}+1)A^+ \tag{4.45}$$

$$n_- = \bar{n}A^- \tag{4.46}$$

For simplicity, we will consider the regime where $\Gamma_{opt} \gg \Gamma_m$, which is nearly always the case with the exception of extremely low optical power, practically irrelevant for us. With some simple algebra, we obtain that:

$$n_{BSB} = \frac{A^-}{A^- - A^+}(A^+ + \bar{n}_{th}\Gamma_m) \tag{4.47}$$

$$n_{RSB} = \frac{A^+}{A^- - A^+}(A^- + \bar{n}_{th}\Gamma_m), \tag{4.48}$$

where n_{BSB} and n_{RSB} are photon rates in the blue- and red-scattered light. Next, we can introduce the "sideband resolution" parameter $r \equiv (A^-/A^+)$ which grows as we approach the resolved sideband regime (given the correct detuning):

$$n_{BSB} = \frac{r}{r-1}(A^+ + \bar{n}_{th}\Gamma_m) = \frac{r}{(r-1)^2}\Gamma_{opt} + \frac{r}{r-1}\bar{n}_{th}\Gamma_m \tag{4.49}$$

$$n_{RSB} = \frac{1}{r-1}(A^- + \bar{n}_{th}\Gamma_m) = \frac{r}{(r-1)^2}\Gamma_{opt} + \frac{1}{r-1}\bar{n}_{th}\Gamma_m \tag{4.50}$$

This parameter lets us clearly see what happens when we go to the resolved-sideband regime ($r \gg 1$):

$$n_{BSB} \rightarrow \bar{n}_{th}\Gamma_m \tag{4.51}$$

$$n_{RSB} \rightarrow 0 \tag{4.52}$$

4.7.1 Output light field

We have determined the photon flux in each sideband. Since the output flux of photons from the cavity must be equal to their generation rate (minus losses), we then know the corresponding output fluxes. For heterodyne detection, this is enough to obtain the measured spectrum. However, for direct or homodyne detection it is necessary to obtain the phase of these sidebands with respect to the drive field. This phase is calculated in the Appendix of (Gorodetsky et al. 2010), and we will just use the normalized result. But first, we show an auxiliary result.

4.7.2 Intensity for drive + sidebands

We assume an input field amplitude of the form

$$E = 1 + e^{i\phi_m}(a e^{i(\Omega t+\phi)} + b e^{-i(\Omega t+\phi)}) \tag{4.53}$$

This corresponds to a drive with two sidebands with arbitrary phases. $\phi_m = (\phi_1 + \phi_2)/2$ is the mean of the two phases, while $\phi = (\phi_1 - \phi_2)/2$. a and b are real. After some algebra, we obtain the resulting intensity. Since we are not interested in the phase of the intensity oscillations and are only interested in the DC component and the AC component rotating at Ω, we obtain:

$$I_{DC}^2 = 1 + a^2 + b^2 \tag{4.54}$$

$$I_{\Omega}^2 = 2(a^2 + b^2 + 2ab\cos(2\phi_m)) \tag{4.55}$$

For example, for the case of phase modulation in free space (such as an EOM), $\phi_m = \pi/2$ and $a = b$, so that

$$I_{\Omega}^2 = 0 \tag{4.56}$$

which is exactly what we would expect: no intensity modulation as everything is in phase quadrature.

4.7.3 Phase of sidebands

According to (Gorodetsky et al. 2010), the sidebands have the following normalized complex multiplier with respect to the drive:

$$L(\omega) = \frac{i\sqrt{1 + 4(\delta + \omega)^2}}{1 - 2i(\delta + \omega)} \tag{4.57}$$

where we have defined $\delta = 2\Delta/\kappa$ and redefined $\omega = 2\omega/\kappa$.

4.7.4 Special case: sideband-resolved regime

While the phase for arbitrary values of sideband resolution can be calculated easily(10) from 4.57, it's instructive to look at the case of sideband-resolved regime. There, given the correct detuning ($\Delta = -\Omega_m$), we obtain that $L(+\Omega_m) = i$, $L(-\Omega_m) = -1$, which corresponds to phases $\phi_1 = 90°$ and $\phi_2 = 180°$, which corresponds to $\phi_m = 135°$.

(10) tediously, that is

This phase information is not necessary, as one of the sidebands is highly suppressed in this regime. The intensity signal in this case is simply (assuming that the sideband is much weaker than the drive)

$$I_{DC}^2 = 1 \tag{4.58}$$

$$I_{\Omega}^2 = 2a^2 \tag{4.59}$$

4.8 Afterword

We have concluded listing the bulk of the most important theoretical results that are applicable to our system. Needless to say, many other results were omitted for brevity. As we have mentioned before, there exists a plethora of excellent literature on optomechanics, and quantum optics in general. The reader is encouraged to look at the resources cited in the above text.

Part III

PRACTICE

CHAPTER 5

OPTOMECHANICAL HOLDER

Arguably the center of our experiments, the optomechanical sample holder stands tall as the battleground of many discussions on the best way to keep the optomechanical system in one piece. It's optomechanics holding optomechanics, after all. The reason why this piece in particular is, perhaps, the single most important piece of copper in a radius of 10 m around our experiment. It has to satisfy several properties:

1. Mechanical stability. With the finesse of our OM cavity being on the order of 20 000, a mirror displacement of only 20 pm corresponds to the width of a whole optical resonance. With a cavity length of, say, 18 mm, and copper modulus of elasticity of 120 GPa, an equivalent g-force that would result in such a shrinkage of a solid copper block is merely (1) $0.002 \cdot g$. And that is solid copper, mind you. We have to design a system that is robust to external vibrations, and reduce those vibrations as much as possible.
2. Good thermalization. As our experiments run at liquid helium temperatures, we need to ensure that our system takes advantage of that, and remains as thermally coupled to its cryogenic environment. That includes not only the sample holder itself, but the membrane and the mirrors as well, which are notoriously difficult to properly thermalize.
3. Ease of assembly and disassembly. With tight requirements on the beam position with respect to the membrane, angular misalignment, and stability, this is a formidable task, and discussions stil continue about the best way to do it.

We will soon see that these requirements are very tight when combined together, even to the point of being slightly self-contradictory. Being a work-in-progress, we shall not go into many historical remarks, and will instead focus on the current design, with its advantages and disadvantages. The topics of membrane holding, mirrors, thermalization, and stability are somewhat

(1) These are back-of-the-napkin Fermi estimates to illustrate the point.

intertwined, so consider reading them in several "passes" to build a better mental picture.

5.1 MECHANICAL CONSTRUCTION

As we stated, the system needs to be thermally conductive at a cool 4 K. Many materials that are thermally conductive at room temperature become much less so at cryogenic temperature. Stainless steel, for example, goes from a somewhat reasonable 10 W/(m K) to a measly 0.2 W/(m K) at 4 K (Duthil 2014)(2),(3). For this reason, our current design uses oxygen-free copper, which retains its good conductivity in the cryogenic domain.

For the adjustability, we followed the footsteps of Jürgen Appel, Christoffer Bo Østfeldt, and the rest of the folks at the "Hybrid" experiment. The approach pioneered by them (Østfeldt 2022)(4) consists in using two flexure stages made out of copper, and based on the Thorlabs CP1XY flexure adjustment plate. These two adjusters allow us to tweak the XY position of both mirrors in the optomechanical cavity, which in turn enables us to change the beam offset and tilt, as shown in Fig. 5.1.

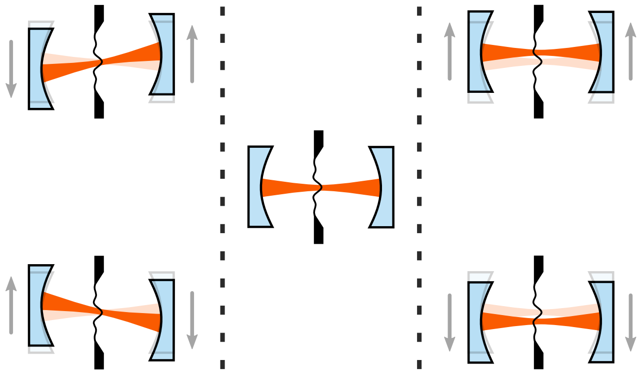

Figure 5.1: Adjustment of optical mode position with respect to the membrane. Left side of the figure shows tilt adjustment where mirrors are moved in opposite directions, while the right side shows shift adjustment, with both mirrors moved in the same direction.

Another feature of this design is the piezoelectric actuation of both mirrors, which allows one to adjust the relative position of the optical standing wave with respect to the membrane by driving the piezos in the same direction, and adjustment of the cavity length (i.e. resonance frequency) by moving them in opposite direction, as shown in Fig. 5.2.

If the reader is interested in more technical details on the cavity construction specifically, we refer them to the relevant PhD thesis (Østfeldt 2022)(5). For us, it will suffice to provide a brief description of the assembly shown in Fig. 5.3.

- The membrane chip is held against the copper using an appropiately sized o-ring made of rubber, which provides even pressure.
- The mirrors are held inside of copper cups. To prevent mechanical coupling of their own motion at 1.4 MHz, they are "sandwiched" between

---

(2) P Duthil (2014). “Material Properties at Low Temperature”. DOI: 10.5170/CERN-2014-005.77. arXiv: 1501.07100. URL: https://cds.cern.ch/record/1973682.

(3) It is used as an thermal insulator in cryogenic devices for this very reason.

(4) Christoffer Østfeldt (2022). “Quantum Optomechanics for Hybrid Spin-Membrane Entanglement”. Niels Bohr Institute, Faculty of Science, University of Copenhagen.

(5) Christoffer Østfeldt (2022). “Quantum Optomechanics for Hybrid Spin-Membrane Entanglement”. Niels Bohr Institute, Faculty of Science, University of Copenhagen.

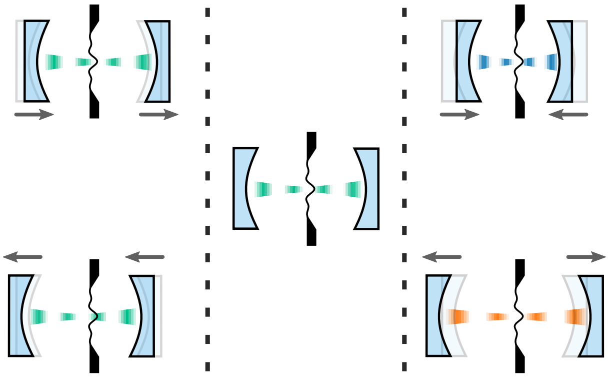

Figure 5.2: Adjustment of relative position between membrane and standing wave (left), or adjustment of cavity length (right).

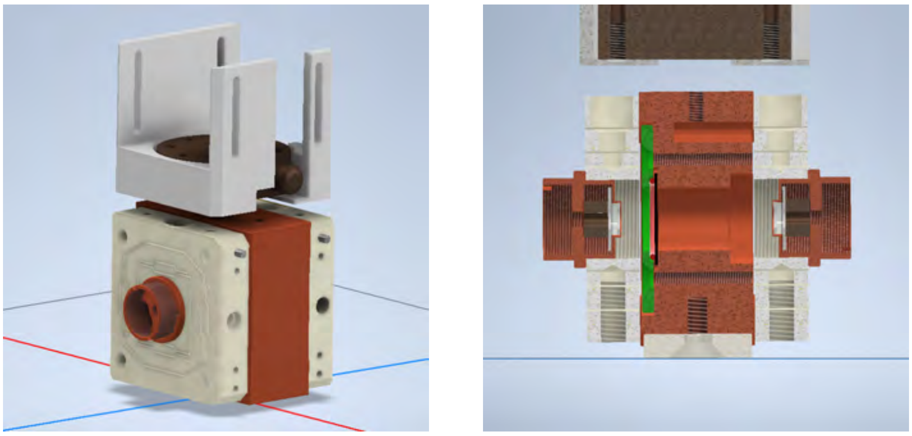

(a) Isometric view of the cavity assembly, showing the XY stages, the mirror cups centered on them, and the copper spacer that increases the cavity length to our desired levels. On top you can see the cryostat mounting adapter that allows us to suspend the cavity from springs.

(b) Half-section view of the optomechanical cavity assembly. The membrane (black line next to the green hold-down piece) is held against the copper. Small mirrors, located at the ends of the mirror cups, are sandwiched between PTFE pieces that decouple them from external mechanical vibrations. On the bottom, we positioned a strong neodymium magnet, discussed in the main text.

Figure 5.3: CAD renders of the optomechanical assembly used in our experiment. Heat straps and springs not shown.

two teflon plates. On top of the mirrors, we place piezotransducers, as we mentioned before.

- The copper cups themselves are screwed into the XY stages to be able to adjust their transversal position for optical mode control.

We take a small pause now to provide context to the description that follows. In contrast to many other membrane-in-the-middle systems, ours is significantly larger. This choice was done due to a number of constraints, the primary being sideband-resolved operation with the set of mirrors that we had on hand. As a result, the length of our resonator is about 18 mm, which needed a bigger overall sample holder, with the bulk of it being roughly a cube with sides of 40 mm. Being so physically large made is much more susceptible to external vibrations to the point of not being workable. Due to this, we took the radical decision of suspending it on springs

5.2 SUSPENSION

The decision to put our optomechanical cavity on a spring suspension came chronologically after our success with spring suspension of the filter cavities (Chapter 8), and was in part inspired by that success. In the case of optomechanics, however, we had a few extra challenges that we didn't have with the filters:

1. Thermalization. The optomechanical cavity needs to be thermally linked to the cryostat to be able to cool down.

2. High-vacuum compatibility. We cannot allow any outgassing material in our system, as the membrane is very sensitive to both contamination and gas damping.

The second challenge is not as big of a deal, as we do not require any damping for very low frequencies of vibrations. However, thermalization is a beast: we need a thermal link between the systems, but *without conducting vibrations*. This last bit is particularly nefarious: mechanical contact can easily be made without conducting heat, but macroscopic heat conduction always requires a mechanical contact of some sort, at least in practice. The best we can do is to make that mechanical contact flexible. Enter heat straps.

Heat straps are simply braids made of thin strands of some conductive material, usually copper. They are often used in practical applications as flexible low-inductance electrical grounding connections, which is why they are mostly marketed as such. In our case we use their heat conductivity and flexibility to our advantage, connecting our spring-suspended assembly to the cryostat with short segments. A balance has to be struck: longer straps are more flexible, but have a proportionally higher heat resistance. Additionally, the space constraints in our cryostat prevent us from using any big number of them, so we settled with one bent strap between the cavity and cryostat, as shown in Fig. 5.4. The work on heat straps was performed by Georg Enzian, our former lab member.

The results of our efforts paid off, with the optomechanical cavity finally being stable enough to be locked. A downside of our constraints was a somewhat low thermalization. We have installed temperature sensors on both the cold finger and the cavity. While the cold finger would always reach the target liquid helium temperature of $\approx$ 4.2 K, the suspended cavity would usually be a little warmer, with typical temperatures in the range of 7.5 K to 8.5 K. While this is suboptimal, it is still low enough to perform the majority of our experiments.

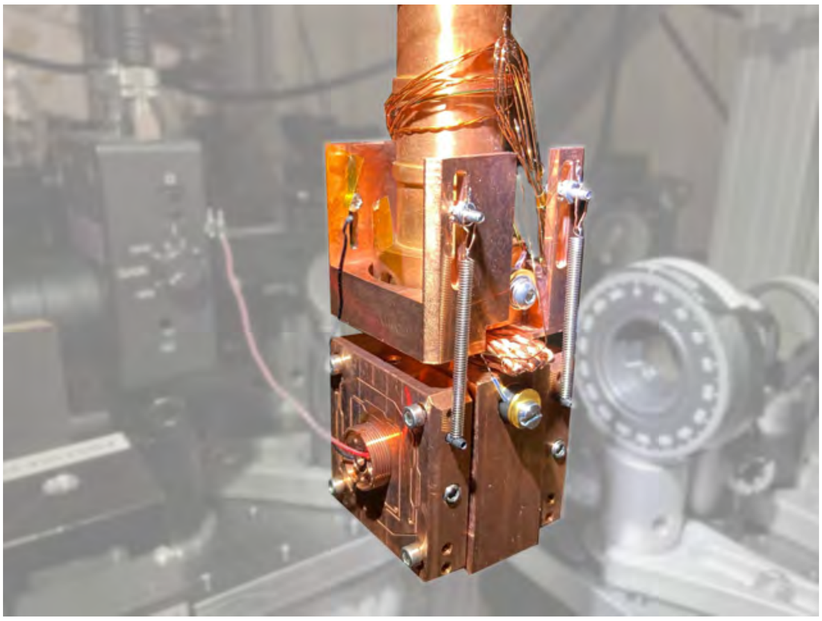

Figure 5.4: Photo of the optomechanical cavity suspended on springs the heat strap is visible between the suspended cavity and the cryostat mounting adapter. This assembly was later gold-plated in order to reduce its emissivity, therefore decreasing the radiative heat transfer from the environment.

5.3 MEMBRANE

Ah yes, The Membrane, the undisputed centerpiece of our experiment, primary source of our joys and sorrows. Anyway, the phononic crystal membrane is the "mechanics" in "optomechanics" for us. Its design and fabrication are an exceptional achievement. For a detailed and thorough explanation of its intricacies, we refer the reader to the comprehensive PhD thesis (Yeghishe Tsaturyan 2019)(6), and (Y. Tsaturyan et al. 2017)(7). Design and fabrication of soft-clamped membranes were pioneered in our group by Yeghishe Tsaturyan, with subsequent work now performed by Anders Simonsen, Eric Langman, and others. For us it will suffice to quickly motivate this particular design, and list their most important properties.

The first optomechanical experiments in our group were performed with commercial membranes manufactured by Norcada Inc. They consist of a layer of silicon nitride (Si_3N_4) deposited on a silicon chip of about 10 mm × 10 mm. A window is etched in the silicon, but not the nitride, creating a suspended square "drum", with a thickness of Si_3N_4 on the order of hundreds of nanometers. Interestingly, their main application is windows for x-rays that separate a vacuum system from its surroundings. The remarkable ultimate tensile strength of Si_3N_4, well over 1 GPa, allows it to withstand large forces. The fabrication process usually yields tensioned Si_3N_4 due to differential thermal contraction between silicon and silicon nitride (the deposition is done at elevated temperatures).

This "drum" will have high-frequency vibrational modes, and the transparency and high refractive index of Si_3N_4 allow us to interact with them

(6) Yeghishe Tsaturyan (2019). "Ultracoherent Soft-Clamped Mechanical Resonators for Quantum Cavity Optomechanics". Niels Bohr Institute, Faculty of Science, University of Copenhagen.

(7) Y. Tsaturyan et al. (Aug. 1, 2017). "Ultracoherent Nanomechanical Resonators via Soft Clamping and Dissipation Dilution". In: *Nature Nanotechnology* 12.8, pp. 776–783. ISSN: 1748-3395. DOI: 10.1038/nnano.2017.101. URL: https://doi.org/10.1038/nnano.2017.101.

optically. Due to the large mismatch between the mass of the spacer and membrane, the drum vibrations are also highly contained, which can lead to Q factors in excess of 1×10^6. The simplicity of these devices, however, has downsides. Since the spacer has vibration modes of its own, sometimes the frequency of these modes overlaps with those of the membrane, which creates mechanical mode hybridization, the effect of which is an opening of additional channels through which mechanical energy can escape from the membrane, effectively damping. The modes of the spacer are also highly dependent on the clamping conditions inside of the assembly, rendering them somewhat unpredictable.

With this in mind (and skipping a few historical steps), a new design has emerged. Its concept is to modify the spacer in a way that creates a phononic shield - a structure that has no mechanical modes in a relevant frequency range. These devices were fabricated by Yeghishe Tsaturyan specifically for our application. The size of the membrane was shrunk down so that its fundamental mode was now the mode with which we worked, instead of using a higher-order mode as was the case with Norcada membranes. This membrane, anchored to a small central feature, forms the "defect" of the phononic crystal.

A little intermezzo on nomenclature. Whenever we use the word "defect" in reference to membranes, we refer to the concept of crystallographic defects. The "defect" is indeed a very precisely engineered structure, placed very deliberately where it has to go.

Continuing our discussion, we shall call the structure around the defect "the phononic shield" or "phononic crystal". Composed of an array of larger elements connected by thin interlinks, it effectively forms a 2D set of masses and springs, the parameters of which are tuned such that at the frequency of oscillation of the defect, the shield has an no modes of oscillation in a range of frequencies. We shall refer to that range as "phononic bandgap". This new construction of membranes removed the dependence on clamping conditions by shielding external modes away. This also led to a substantial and repeatable increase of the Q factor up to previously unprecedented levels of 25×10^6 (Møller et al. 2017)(8), which in turn was instrumental in achieving exceptional scientific results.

But the progress does not stop here! There was still one outstanding issue that limited the quality factor of the membrane resonators. The root of this problem lies in the fact that the very thin Si_3N_4 membrane is rigidly anchored to its surrounding silicon frame. At these points of contact, silicon nitride experiences severe bending forces relative to the rest of the membrane, resulting from its rigid boundary conditions. This bending or, in other words, curvature, leads to a number of processes that create dissipation. The exact physics of these process is rather intricate, for which we again refer the reader to (Yeghishe Tsaturyan 2019)(9).

The breakthrough method of *soft clamping* allowed the quality factor to be pushed to levels previously unheard of. The idea is deceivingly simple: instead of incorporating the phononic shield in the silicon spacer, make it part of the membrane itself! Not only is this, in author's opinion, a more elegant and streamlined approach, but it also solves the problem with bending-induced losses. Now, the central defect is no longer rigidly clamped, but is instead attached to the same kind of structure: the same thin slab of Si_3N_4.

(8) Christoffer B. Møller et al. (July 2017). "Quantum Back-Action-Evading Measurement of Motion in a Negative Mass Reference Frame". In: *Nature* 547.7662, pp. 191–195. ISSN: 0028-0836. DOI: 10.1038/nature22980. URL: http://www.nature.com/doifinder/10.1038/nature22980.

(9) Yeghishe Tsaturyan (2019). "Ultracoherent Soft-Clamped Mechanical Resonators for Quantum Cavity Optomechanics". Niels Bohr Institute, Faculty of Science, University of Copenhagen.

This allows its vibrations to softly (evanescently) decay, as shown in simulation in Fig. 5.5, and experimentally in Fig. 5.7.

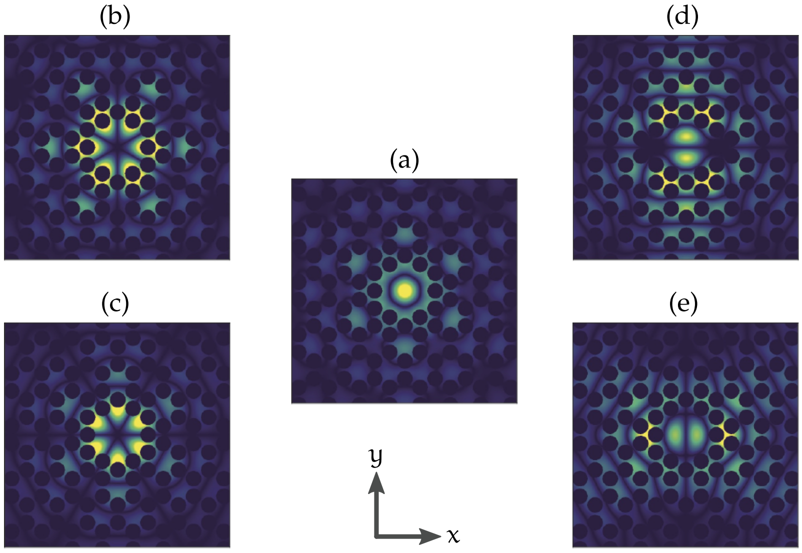

Figure 5.5: Simulated displacement color map of localized defect modes in a phononic-shield membrane. Figure adapted from (Y. Tsaturyan et al. 2017).

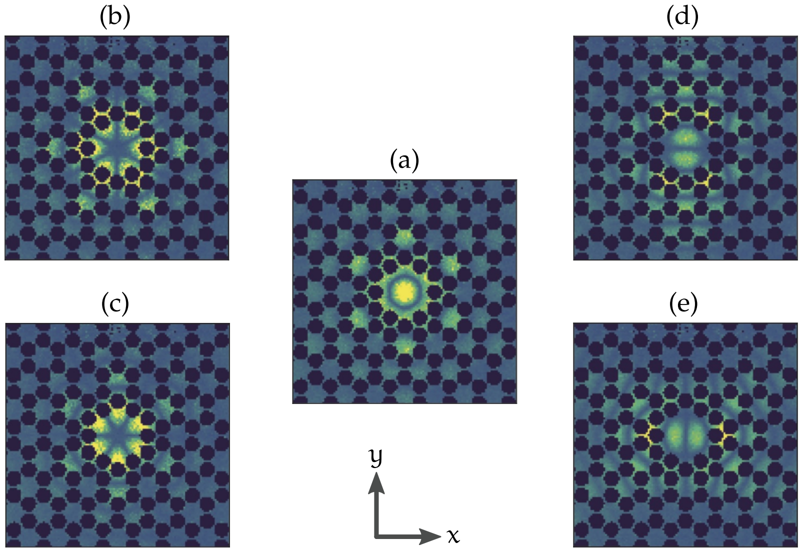

Figure 5.6: Measured mode shapes of localised defect modes (top) with frequencies $\{f_A, f_B, f_C, f_D, f_E\} = \{1.4627, 1.5667, 1.5697, 1.6397, 1.6432\}$ MHz for a device with a lattice constant of $a = 160\,\mu\mathrm{m}$. Figure and description adapted from (Y. Tsaturyan et al. 2017).

This last change is crucial for keeping the quality factor high. The jump was so significant, that even earlier devices showed

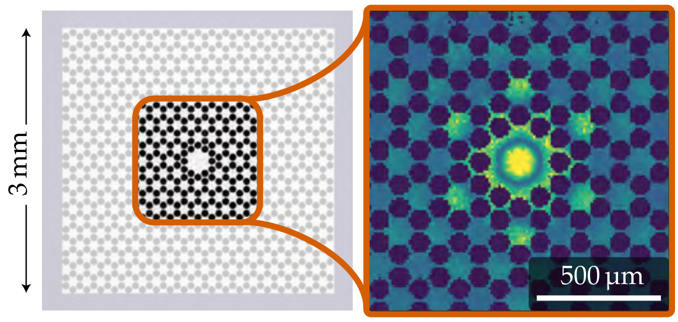

Figure 5.7: Phononic structure of our mechanical oscillator (left) and experimentally measured displacement pattern of the main mode (right), showing the scale of the device. Adapted from (Zwettler 2019), in turn adapted from (Y. Tsaturyan et al. 2017).

5.4 Mirrors in optomechanics

The mirrors form the optical cavity, which in turn creates the resonance necessary for our experiments. Mirror selection is a critical choice that dictates many other choices that have to be made with regards to experimental design. The requirements are those for any high-finesse optical cavity, but their use with optomechanics places additional constraints:

1. High reflectivity with low loss. The finesse resulting from the mirrors' reflectivities defines the length of the cavity for a given target linewidth, which in turns defines the strength of our optomechanical coupling. Any non-transmission loss results in a decrease of quantum efficiency, as the signal generated by the optomechanics gets irreversibly attenuated.

2. Low mechanical noise. This is an unusual requirement for mirrors, but it is yet another factor that is exceptionally important to us. Any vibrations of the mirrors that couple to the light beam at the frequency of our main mechanical mode around 1.4 MHz will be transduced into fluctuations of intra-cavity intensity(Gorodetsky et al. 2010), which will result in an increased phonon occupation. Additionally, the broad nature of mirror noise can lead to additional photon counts, even if it is practically undetectable in a spectral density.

3. Overcoupling of the cavity. This is somewhat related to the first point, but places additional restrictions on the reflectivities. We want our optomechanical signal to leave preferentially through one of the two ports of the cavity, so that we can collect it. While it's in principle possible to collect light emanating from both ports, combining it for, say, single-photon counting would be a big and unnecessary effort.

4. Beam size at the membrane. Since the membrane defect, which hosts our mode of interest, is relatively small ($\approx$ 200 µm), the beam needs to be small enough to "fit" without clipping. By "clipping" we refer to some of the beam power hitting the edges of the defect, which results

> in distorted optical modes, additional loss, lower coupling to the mechanical mode due to poor overlap, and possibly additional heating. This requirement places constraints on the radii of curvature for both mirrors.

Formidable work (Mathiassen 03/Dec/2019) on simulations of mechanical motion of mirrors has been performed by one of the members of QUANTOP, and a former member of our experiment, Jonas Mathiassen. The conclusion from that work, and many other discussions, was the decision to buy mirrors whose dimensions are small enough to space apart mechanical modes, creating regions with low enough mirror noise level. In practice, their dimensions are a diameter of $\approx 5\,\mathrm{mm}$, and a thickness $\approx 1\,\mathrm{mm}$. We shall refer to them as "small mirrors" for hopefully obvious reasons.

These mirrors were coated by FiveNine Optics, with substrates provided by Perkins Precision Developments. Their clamping requires special attention, as we need to minimize their interaction with the holder. Such interactions typically lead to shifts in the frequency of the mirror’s modes, in addition to broadening. In the end, the approach that we settled upon was to use thin plates of PTFE. This approach, while effective at softly holding the mirror and preventing mechanical coupling, has the disadvantage of severely reducing the thermal contact between the mirror and its cryogenic environment, which is one of the hypotheses for explaining spurious heating that we observe in our system (discussed further in this work). Work is still ongoing for determining the best practices for mirror holding.

Chapter 6

OMIT (OPTOMECHANICALLY-INDUCED TRANSPARENCY)

One of the most important experimental techniques for us is the optomechanically-induced transparency, or OMIT for short. In our experiment, OMIT serves as a very convenient tool for characterizing the mechanical response of the oscillator, together with the optical response of the optomechanical cavity. It is a close relative to electromagnetically-induced transparency (EIT) pioneered by Chien Liu and others in Lene Vestergaard's group (Liu et al. 2001). While EIT does require a quantum treatment due to the nature of atomic transitions, OMIT can be treated fully classically. At its core lies the interaction between mechanical motion and two light beams. For a full treatment of OMIT, we refer the reader to (Nielsen 2016)⁽¹⁾ and (Østfeldt 2022)⁽²⁾, while we will describe its core principles and consequences.

Let us start by describing the experimental procedure for obtaining an OMIT response, as this will later guide our exposition:

1. We begin with a single, relatively strong optical tone applied to the cavity, typically red-detuned. We will refer to this beam as "carrier", a standard term in RF circles.

2. A relatively weak phase modulation is applied to this beam, typically with an EOM, which creates a pair of sidebands separated by ω to either side of the carrier. The modulation has to be chosen such that other, higher-order sidebands, are negligible. By extension, this also guarantees that the sidebands are significantly weaker than the carrier itself.

3. The transmission of the cavity is being monitored using a detector in direct detection, i.e. simply observing the intensity signal at the output of the system.

(1) William Hvidtfelt Padkær Nielsen (2016). "Quantum Cavity Optomechanics with Phononic Bandgap Shielded Silicon Nitride Membranes". University of Copenhagen. 160 pp.

(2) Christoffer Østfeldt (2022). "Quantum Optomechanics for Hybrid Spin-Membrane Entanglement". Niels Bohr Institute, Faculty of Science, University of Copenhagen.

4. The frequency of phase modulation is swept in a suitable range. For characterizing the mechanical response ("narrow OMIT"), such range is typically between $\Omega_\mathrm{m} - 3\Gamma_\mathrm{opt}$ to $\Omega_\mathrm{m} + 3\Gamma_\mathrm{opt}$. For the overall cavity response ("broad OMIT"), we usually choose the lower frequency to be about 200 kHz, and the higher frequency to be $\Delta + 2\kappa$, mostly for technical reasons.

5. Using a vector network analyzer such as NanoVNA, or an equivalent device (Red Pitaya, for example), the magnitude of coherent intensity oscillations of the output intensity is recorded for each modulation frequency ω. This recorded data is later fitted to an analytical model, from which we recover all parameters of interest.

A little note on notation: in our group, we often refer to "broad OMIT" and "narrow OMIT". As we stated above, "broad OMIT", strictly speaking, has nothing to do with mechanics, and is a property of any optical resonator, with or without a mechanical oscillator inside. "Narrow OMIT", on the other hand, is the real thing. But since both measurements are practically obtained in one go, we gave them similar names.

Another important note is that our version of OMIT differs somewhat from its canonical definition. As introduced in (Weis et al. 2011)(3), the experiment consisted of a *probe beam*, which we call "carrier", and a *single* "control beam", which in our case is replaced by a pair of sidebands. This difference changes the observed response function somewhat, but the core principle remains. Another difference from the canonical definition is that we are observing the output in *transmission*, not reflection. Indeed, while the experiment of Weis et al. (2011) observes a peak in the reflectivity of their resonator, corresponding to overall "transparency", our measurements instead show a rather strong "dip", as the reflection redirects away from the transmission port. In that sense, we might call our technique "optomechanically-induced rejection", but that doesn't pack quite the punch.

The mathematics of OMIT are a bit tedious, if anything. The core principle, however, is rather simple: the input sidebands, originally in the phase quadrature of the incoming carrier, are transduced into intensity fluctuations inside of the optical cavity. These intensity fluctuations drive the mechanical oscillator. Since the oscillator is now moving, it itself starts to scatter the carrier into its "own" sidebands, which can interfere destructively or constructively with the "original" sidebands inside of the cavity. The net effect is a change in the amplitude fluctuations as seen on the output of the cavity in transmission (which effectively amounts to sampling the intracavity field).

When performing a sweep as described above, a signal illustrated in Fig. 6.1 is obtained, where we take the magnitude squared of the signal, as phase information is rarely important enough. With a fit of our analytical model, we obtain the majority of experimentally relevant parameters, in particular the optomechanical cavity's decay rate and detuning (κ and Δ), optical broadening Γ_opt, and by extension the linearized interaction strength g, which can be used (with extra calibration) to determine the single-phonon coupling g_0. The almost single-shot measurement of all these parameters is the reason why we use OMIT very extensively, and it is a routine calibration procedure.

(3) S. Weis et al. (2011). "Optomechanically Induced Transparency". In: *2011 Conference on Lasers and Electro-Optics Europe and 12th European Quantum Electronics Conference, CLEO EUROPE/EQEC 2011* 58.22, pp. 23236–23246. ISSN: 0036-8075. DOI: 10.1109/CLEOE.2011.5943657. pmid: 21071628.

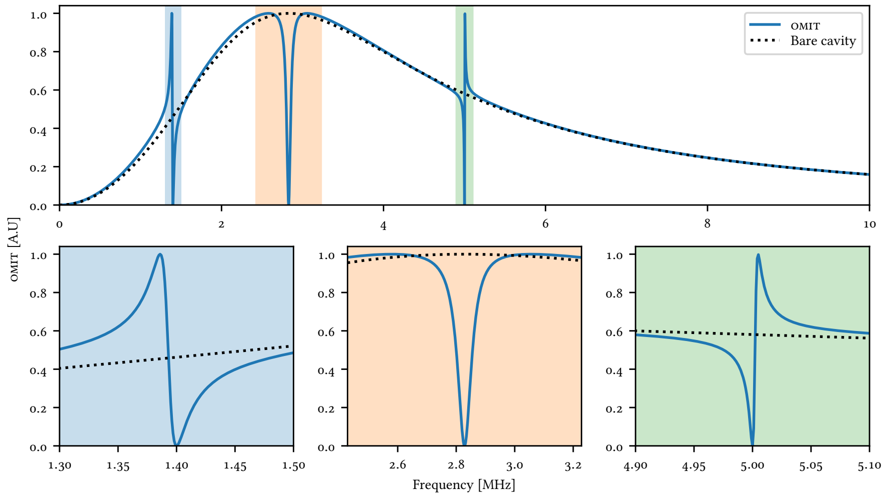

Figure 6.1: OMIT signal. Top panel: bare cavity ($g_i = 0$, dotted line) and full OMIT response with three mechanical modes for illustrative purposes. Bottom row: zoom in on the resonances. All traces are normalized to the maximum response for the empty cavity. $\kappa/2\pi = 4\,\mathrm{MHz}$, $\Delta/2\pi = -2\,\mathrm{MHz}$, $\gamma_{0,i}/2\pi = 1\,\mathrm{mHz}$, $g_i/2\pi = 200\,\mathrm{kHz}$, $\omega_0/2\pi \in \{\,1.4\,\mathrm{MHz}, \sqrt{\Delta^2 + (\kappa/2)^2}\,/2\pi{\sim}2.83\,\mathrm{MHz}, 5\,\mathrm{MHz}\,\}$. Figure and description reproduced with permission from Østfeldt (2022)

Part IV

RESULTS

CHAPTER 7

PHASE NOISE CANCELLATION WITH A DELAY LINE

> Noise proves nothing. Often a hen who has merely laid an egg cackles as if she laid an asteroid.
>
> MARK TWAIN

This chapter is based on and includes figures from our publication (Parniak et al. 2021)

7.1 OVERVIEW OF CLASSICAL PHASE NOISE

To remind the reader, our optomechanical system operates in the sideband-resolved regime. One of the consequences of that is that phase fluctuations of input light get transduced almost directly into light intensity fluctuations inside of the cavity. What this means in practice is that phase noise on the input light becomes mechanical force noise acting upon our membrane. This noise is inevitably present in all real lasers, but can also be worsened by thermorefractive noise of optical fibers, noisy electro-optic modulators, and any other device capable of acting on the phase of light. Such noise prevents us from cooling the mechanical oscillator it to the theoretical limit, and from performing quantum-limited measurements.

It's important to note that titanium-sapphire lasers already have a rather low phase noise at our frequencies of interest. For example, the laser that we are using(1) has a phase noise floor of approximately −155 dBc at an offset of 1.5 MHz (Parniak et al. 2021). While for many experiments such level of noise is more than sufficient, our system is a particularly picky eater. Due to the need for sideband resolution and our technical constraints, our optomechanical cavity is approximately 19 mm long, which means that the

(1) MSquared SolsTiS

optomechanical coupling strength is low ($g_0 < 10\,\mathrm{Hz}$). That is the same as saying that perturbations of mechanical position translate to smaller changes in the frequency of the cavity, when compared to similar MIM systems. Therefore, to achieve the same broadening and the same interaction strength as for shorter cavities, we have to increase the laser power, i.e. increase the intracavity photon number. Because classical phase noise increases as laser power is increased, we'll see a larger intracavity intensity noise, which will "jiggle" the mechanical oscillator. If left untreated, this would prevent us from cooling the mechanical mode to desired occupations of less than 0.2 phonons, necessary for non-classical heralded state preparation (Galland et al. 2014)(2).

There are many ways in which one can counteract phase noise in laser systems. One such approach is to filter the laser light by passing it through a dedicated filter cavity. There, the narrow resonance width of the cavity rejects noise that of its passband. But as with anything in experimental science, there are strings attached. Remember that mirrors used in optical cavities are not completely passive objects: they have a temperature and show thermal fluctuations in the surface of the mirrors, leading to phase noise, as shown in Fig. 7.1.

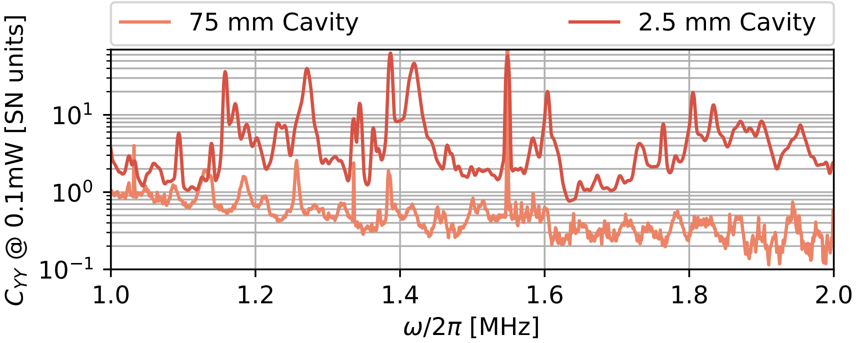

Figure 7.1: Mirror-dominated phase noise of light exiting a cavity for different lengths of the resonator. While the mirrors used are different, the general trend of reduced influence of mirror noise with larger lengths is visible. Figure used with permission from Zwettler (2019)

Practically, unless one is willing to cryogenically cool the mirrors, they will be at room temperature, and their noise will be non-negligible. Yep, it's optomechanics again. In this case though, light does not affect the motion of the mirrors (unless you're LIGO), but the motion of the mirrors does affect light. For example, for a cavity of 15 cm om length, and standard-issue 12.7 mm mirrors, these fluctuations are just as big as the phase noise of the laser. Therefore, while the phase noise of the laser will get reduced, the filter itself will imprint its own noise onto the light, and we're not much better off, as shown in Fig. 7.2. Of course, one can solve the problem by making the filter cavity longer and longer (therefore decreasing the strength of these optomechanical effects). But that's difficult to maintain, requires continuous locking, and places restrictions on the maximum optical power due to intracavity intensity build-up.

(2) Christophe Galland et al. (2014). "Heralded Single-Phonon Preparation, Storage, and Readout in Cavity Optomechanics". In: *Physical Review Letters* 112.14, pp. 1–6. ISSN: 10797114. DOI: 10.1103/PhysRevLett.112.143602. pmid: 24765960.

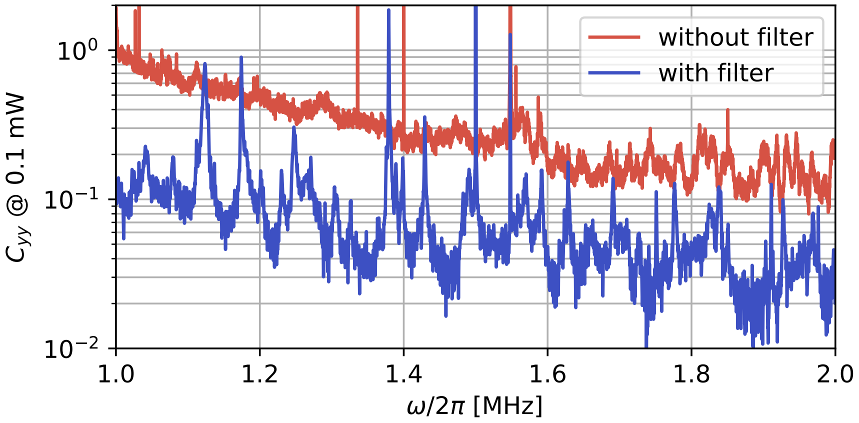

Figure 7.2: Comparison of laser phase noise before and after being filtered by a 150 mm cavity, and measured by our delay line. Reproduced from Zwettler (2019)

But there is another way! There exist systems that are capable of measuring the phase noise of the laser. We can then use the measured phase noise and apply a correction using an EOM, for example. One could use a cavity as a way to transduce phase fluctuations into detectable amplitude fluctuations. But notice that this has the same problem as a filter cavity there, where mirror noise will result in additional noise being imprinted onto the output light, so we're not gaining anything. Another method involves using a highly imbalanced Mach-Zehnder interferometer, where one of the arms is "long enough". "Long enough" means that by the time that the light propagates through this long arm, the phase of phase noise (yes, it's a tautology) gets shifted enough to interfere constructively with the undelayed light. This sounds a bit convoluted, so let us look at an example that's oddly similar to the system that we actually use.

Take a Mach-Zehnder interferometer where one arm is essentially zero length, while the other is $L \approx 70\,\mathrm{m}$ long, equivalent to a time delay τ. At the input of the interferometer we have our noisy light, with phase fluctuations $\varphi(t)$. The light gets split into two beams, where one is delayed by τ, while and other is not delayed. The two beams are combined again, and measured on a balanced photodetector, as shown in Fig. 7.3. This produces a signal proportional to $\varphi(t) - \varphi(t - \tau)$.(3) This is equivalent to the following frequency-dependent transduction function, illustrated in Fig. 7.4

$$G(f) = 1 - \exp(-i\tau\omega) \tag{7.1}$$

Looking at the absolute value squared, one can see that $|G(f)|^2 \propto \sin^2(\tau\omega/2)$. That is, phase fluctuations will be translated into intensity fluctuations, with maxima of sensitivity occuring at $\omega = (n + 1/2)\pi/\tau$, with integer n. Then, a 70 m-long delay line will produce its first maximum of sensitivity at around 2.1 MHz, while at our frequency of interest of 1.4 MHz the sensitivity is about 76 % of the maximum, which is plenty good. In practice, creating such long optical delays is practical using optical fibers. In our case, the light to be delayed propagates through 50 m of fiber, and then returns back to the

(3) We assume that the interferometer is operated in the usual Mach-Zehnder way, with the two output beams being equal in average optical power

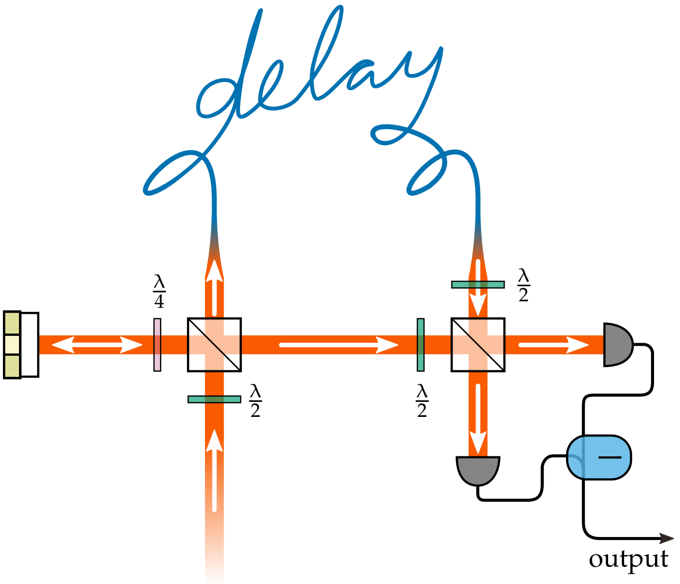

Figure 7.3: Schematic of a single delay-line Mach-Zehnder setup for phase noise measurements. The piezo on the left is necessary to lock the relative phase of the two arms and guarantee balanced operation

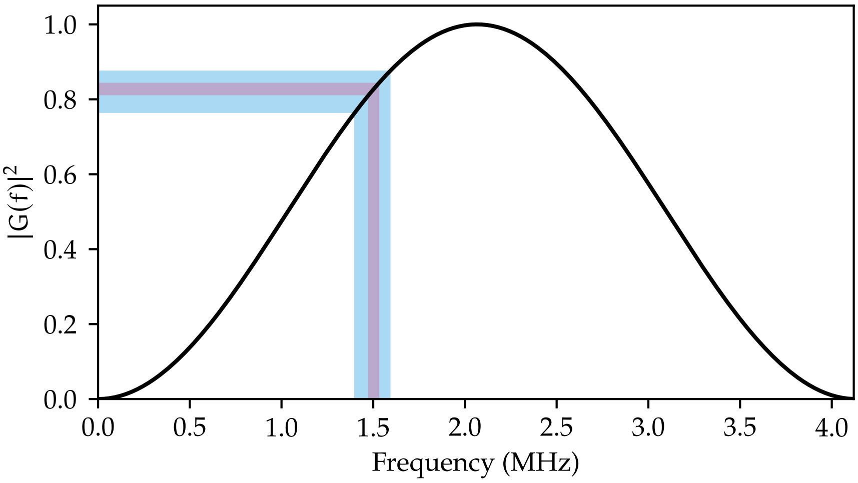

Figure 7.4: Magnitude squared of delay line response to phase fluctuations of external light. Blue color highlights the range of frequencies where our membranes typically have their main mode, while the pink color shows a band of 60 kHz to demonstrate the region where a membrane with $\Omega_m = 2\pi \times 1.5\,\text{MHz}$ any non-negligible sensitivity to noise.

interferometer. Common optical fibers have a refractive index of $\approx$ 1.45 at our wavelength of 852 nm, which is why were mentioning an optical length of 70 m.

In the end, we're capable of measuring the phase noise of the laser quite well. Next, we use that signal to feedback on the light in order to cancel this noise. It might seem a bit counterintuitive that something involving the word "delay" can be used for this purpose at high frequencies, as delays are the natural enemy of feedback. But there is a catch: for feedback purposes what matters is the *bandwidth* of the feedback, and not its absolute frequency. Also remember that not all light is delayed: the short arm lets half of the light to reach the detector, and also contains the phase noise. The long arm serves as a memory of sorts, to "remember" the state of the light as it was "50 meters of fiber ago". This is even more evident if one looks at the *time* response of this system to a step in the phase of the input light, where the instantaneous response is evident, as shown in Fig. 7.5.

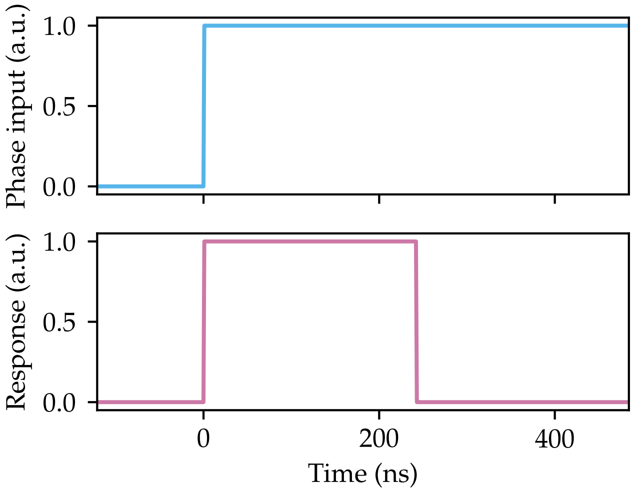

Figure 7.5: Step response of the delay line setup with respect to a step change of the input light phase. Notice that the initial response is instantanous.

Note that the shape of the response function is not great for very-broadband cancellation of phase noise at all frequencies simultaneously. This system displays a constant group delay of $\tau/2$, so the maximum achievable feedback bandwidth would be limited by that. Fortunately for our system, it is not necessary to have fully broadband cancellation, as the main mechanical mode has a bandwidth on the order of 10 kHz(4). By focusing the cancellation in a narrow range around $\Omega_m \approx 1.4\,\mathrm{MHz}$, we can use a scheme that is effectively a phase-controllable electronic bandpass filter. For this purpose, a Red Pitaya performs the following actions, all integrated into a single, highly useful, "iq module":

1. Demodulate the measured phase noise at Ω_m, obtaining the I and Q quadratures.(5)

2. Lowpass both quadratures with a lowpass filter, typically with a 20 kHz cutoff.

(4) When optically broadened

(5) I and Q are standard notation in electrical engineering, where they represent terms proportional to $\sin(\omega t)$ and $\cos(\omega t)$, respectively. ω is the demodulation frequency

3. Multiply the resulting filtered quadratures again by their corresponding sin and cos, but shift the phase of these functions by a controllable amount. This phase shift is determined empirically to produce the best response.

4. Output the signal.

Finally, the resulting signal is sent to a free-space EOM placed just after the laser. We use a free-space EOM because it handles well high powers at the output of the laser and does not require fiber coupling. The high $v_\pi \approx 600\,\mathrm{V}$ poses no problem for us, as the necessary strength of the feedback signal is pretty much negligible. As a matter of fact, we even attenuate the signal coming from the Red Pitaya by 20 dB. This allows the Pitaya to generate larger signals, which avoids problems with digital discretization. Fig. 7.8, later in our exposition, shows the in-loop spectrum with and without cancellation.

7.2 Extracting phase noise

To know the performance of our system, we need to compare the phase noise with and without the feedback enabled. Before, a bit of nomenclature: "in-loop" means we are measuring the effects of the feedback loop, as seen by the loop itself. Interestingly, you can see that the measured noise can dip even below shot noise. "Unfortunately"(6), this does not imply that any light outside of the loop will be sub-shot-noise. It's simply a property of feedback.

(6) One can't complain about physical laws being as they are.

To actually know that our scheme is working, we have constructed a second identical setup, using another 50 m fiber delay line, as shown in Fig. 7.6. This setup, however, is not used in feedback, but simply measures resulting phase noise externally. There are several hizzards in the way, though:

- The two feedback loops will have different sensitivities due to different detectors, fiber lengths, optical powers, and acquisition channels.
- The shot noise and electronic noise are uncorrelated between the two setups.
- The fiber noise (more on that later) is also uncorrelated between the setups.

Due to all of the above, we created a scheme where we can disregard sensitivity differences, and get rid of the inevitable uncorrelated noise in order to see the pure phase noise. Now, we cannot simply make all this noise go away (unfortunately). However, we can compensate for them during statistical analysis "post-mortem". This procedure is divided into two parts: sensitivity calibration, and noise separation via cross-correlation.

7.3 Sensitivity calibration

As we said, the two measurement setups will have slightly different sensitivities to phase noise, which we need to make equal. This is how we do it:

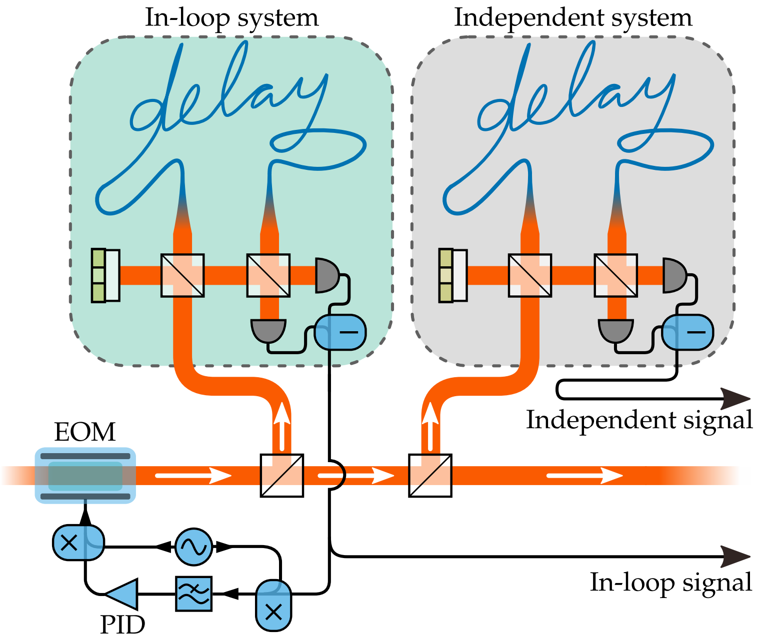

Figure 7.6: Schematic of the double system that we use for characterization of phase noise cancellation.

First, we turn off phase noise cancellation, as we need the "raw" response of both setups. Then, we apply a small square-wave modulation to the free-space EOM. Remember that a square wave has many spectral components, consisting of multiples of its base frequency (harmonics). All these narrow peaks in the spectrum serve as a "calibration comb", equally affecting light seen by both setups. Additionally, since each one of these peaks is very narrow in the frequency domain, but contain sufficient power, they will "protrude" through the spectrum, as shown in Fig. 7.7. We then look at the how both setups transduce these peaks, which shows us the differences in their sensitivity to phase noise, which allows us to compensate for them during subsequent analysis.

7.4 CROSS-CORRELATING SIGNALS

We are acquiring both signals simultaneously on our DAQ card and saving them as time traces, so we can compute a cross-correlation between the two signals. Cross-correlation has this nice property of removing any kind of noise that is not common to both systems, i.e. uncorrelated. This includes light shot noise, fiber noise, and electronic noise. We are then left only with phase noise. To be more concrete, let us describe the spectral properties of our measurements. We will follow the approach of our publication, Parniak et al. (2021). First of all, the spectral density of any one of the systems is, when feedback is disabled, given by

$$S = \eta \bar{P}^2 |G(f)|^2 S_{\varphi\varphi} + \eta \bar{P}^2 S_{\varphi_f \varphi_f} + 2h\nu\bar{P}, \tag{7.2}$$

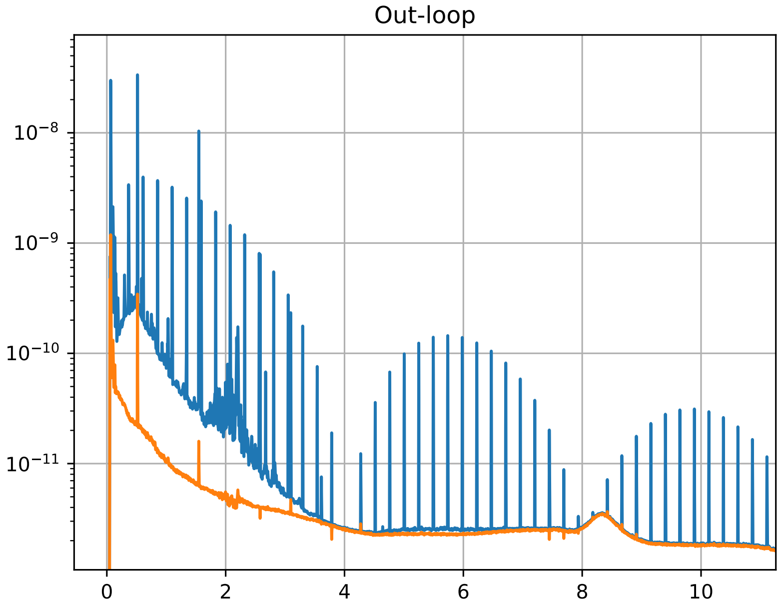

Figure 7.7: Effect of calibration peaks produced by the free-space EOM during the sensitivity calibration procedure. Blue trace shows the measured noise, while the orange trace shows background noise, dominated by phase and fiber noise. Notice the fiber's mechanical peak at ≈ 8.2 MHz. Figure reproduced from Parniak et al. (2021)

where we denote the average laser power as $\bar{P}$, laser phase noise as $S_{\varphi\varphi}$, detection efficiency due to interferometric visibility as η, and fiber noise as $S_{\varphi_f\varphi_f}$. Note that fiber noise is transduced at all frequencies, as it originates only in one arm of the interferometer (delay line). The last term is simply shot noise of light.

The other delay line will have the same response, as we have already performed the sensitivity calibration, and assume the same power and efficiency in both setups (in practice we measure and compensate for power and efficiency differences where necessary). As we have mentioned before, the only signal "shared" between the systems is the laser phase noise, so if we compute the cross-correlation of signals obtained simultanously from the two setups, we obtain:

$$S^{12} = \eta\bar{P}^2|G(f)|^2 S_{\varphi\varphi}. \tag{7.3}$$

Note how remarkably simple this expression is, directly proportional to laser phase noise. From this, we extract that refined cold-pressed extra-virgin phase noise, as shown in Fig. 7.2 and Fig. 7.1. As a bonus, this allows us to obtain only the incoherent noise in each setup by simple subtraction, $S_{\text{incoh}} = S - S^{12}$, which is useful for determining fiber noise later.

After we have characterized the sensitivity in this way and obtained spectra without feedback, we can finally turn the feedback back on. As you can see, the phase noise measured by the out-of-loop detector is improved very considerably, almost 10 dB in the region of interest! A comparison of performance at different feedback gains is shown in Fig. 7.8, as seen both in-loop and out-of-loop. A wise reader will ask, "why stop there, why not improve the cancellation even more?". Well, there's this whole other can of worms called fiber noise.

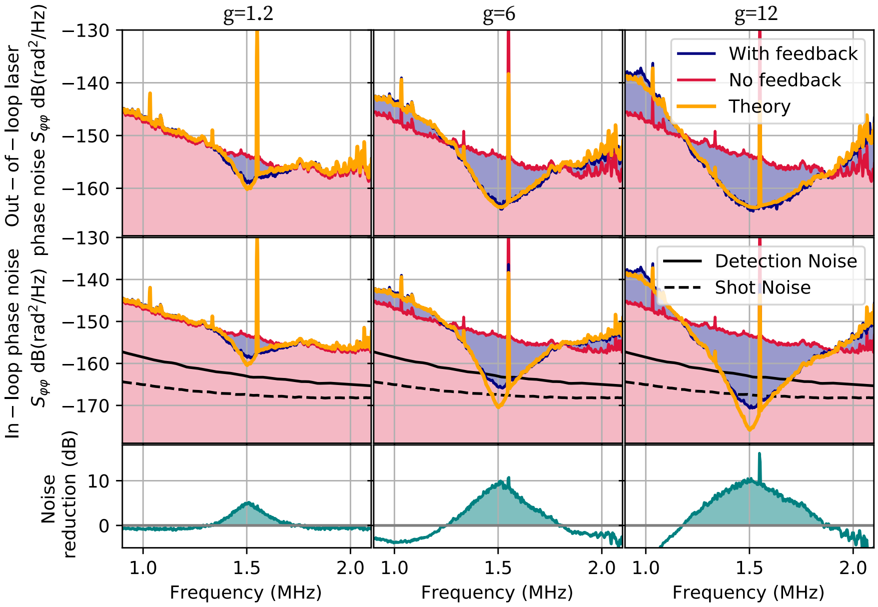

Figure 7.8: Performance of the delay line noise cancellation, measured both in-loop and outside of the feedback loop. Reproduced from Parniak et al. (2021)

7.5 FIBER NOISE

Optical fibers have a phase noise of their own. At our frequencies of interest, thermal fluctuations in the fiber core and cladding produce minute changes in the refractive index of the fiber material (Duan 2012), thermoconductive noise being the dominant for us. We expect our noise to be of the following form, derived by (Duan 2012) and (Foster, Tikhomirov, and Milnes 2007), and applied to our scenario in (Parniak et al. 2021):

$$S_{\varphi_f\varphi_f} = \frac{4\pi^2}{\lambda^2}\left[\left(\frac{dn}{dT}+n\alpha\right)^2 L^2 S_{\delta T}(\omega)\right] \tag{7.4}$$

$$= \frac{2k_B T^2 L}{\lambda^2 \kappa}\left(\frac{dn}{dT}+n\alpha\right)^2 \operatorname{Re}\left[\exp(2\pi i f r_0^2/2D)E_1(2\pi i f r_0^2/2D)\right] \tag{7.5}$$

$$\approx \frac{4D^2 k_B T^2}{\kappa}\cdot\frac{1}{r_0^4\lambda^2}\cdot\left(\frac{dn}{dT}+n\alpha\right)^2\cdot\omega^{-2}\cdot L, \tag{7.6}$$

where the last approximation is valid for high enough frequencies (approximately > 200 kHz), perfectly applicable to our case of ≈ 1.4 MHz, as shown in Fig. 7.9. The material constants are those of silica, and are listed in Duan (2012). Notice, however, the inverse dependence on the *fourth* power of the mode radius, r_0^{-4}, and the inverse scaling with frequency squared. Also note the dependency on T^2. This is not a mistake: fiber noise is driven not only by bare temperature fluctuations, but by diffusion also. The combination of these processes yields the quadratic dependence.

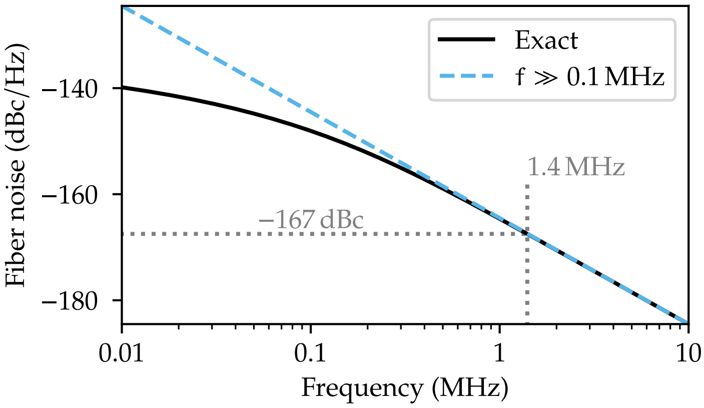

Figure 7.9: Analytical expectation of fiber noise, with full model from (Duan 2012), and high-frequency approximation from (Foster, Tikhomirov, and Milnes 2007). Note the vertical unit of dBc/Hz, which characterizes the optical power scattered from the main laser frequency ("carrier") by phase noise. As it happens, the magnitude of that scattered spectral density is exactly equal to the carrier power multiplied by phase noise density expressed in rad^2/Hz. From this point, we treat these two units as synonymous.

Thermoconductive noise is dominant, but we should notice that fibers also have intrinsic mechanical noise due to longitudinal or bending mechanical modes (at lower frequencies), or transverse mechanical modes (at higher frequencies). One example of such modes is the first transverse mode, shown in Fig. 7.7 around 8.2 MHz. We disregard that noise, as in our frequency regime these kinds of noise are not present. Thermoconductive noise, however, sets a limit to our best achievable phase noise performance, as one can see in Fig. 7.9. Due to the extreme sensitivity to the radius of the optical mode (which itself is mostly proportional to the fiber core diameter), if we could obtain a fiber even with a marginally larger mode diameter, we could reduce this fiber noise even further. Unfortunately, such fibers are not really available, or are rather expensive (photonic air-core fibers). However, 10 dB of noise reduction is already sufficient for us to not be a strong limitation in our experiments.

As a sidenote, one possible approach to reducing fiber noise, and therefore increasing the phase noise cancellation even further, is to cryogenically cool the fiber itself. Not only would this reduce the noise simply by virtue of reducing diffusion and thermal fluctuations, but also the thermo-optic and thermo-refractive coefficients of the fiber, leading to a very substantial reduction of overall fiber phase noise. We have attempted this approach briefly by submerging the fiber loop into liquid nitrogen. Unfortunately, bubbles, uneven cooling, and other perturbations made the system very unstable, and we decided to continue working at room temperature, as the current performance level is completely acceptable.

Related to the fiber noise, the cross correlation technique discussed above has the curious side effect of allowing us to look at the fiber noise of each system separately. And an interesting result is that we can see not only the predicted fiber noise at low frequencies that tapers off when approaching higher frequencies, but also the high-frequency transversal mechanical modes of the fiber. As can be seen in Fig. 7.7, there is a mechanical peak at ≈ 8 MHz in the one of the setup, with a similar peak in the other setup. The interesting thing is that their frequency is not exactly the same. We believe this to be due to differing core sizes of the two fibers, as some variability is inevitable in manufacture. We therefore chose the fiber that had a lower frequency of this first mechanical mode, which should indicate a larger core diameter, beneficial to phase noise performance at our frequencies.

7.6 CONCLUSIONS AND OUTLOOK

As we have mentioned before, the results of this chapter were published (Parniak et al. 2021). Interestingly, before our publication(7) there were no investigation into this frequency regime of fiber phase noise, with most work concentrated around low frequencies (relevant for optical metrology, where fibers are routinely stabilized), or very high frequencies (Brillouin scattering, relevant for telecommunications).

(7) to the best of our knowledge

The main result, of course, was showing that phase noise of an already quiet laser system can be improved substantially. For us, this is and will continue to be instrumental in achieving low optomechanical occupation via sideband cooling. We have achieved a reduction of almost 10 dB of phase noise at our frequency of interest of 1.4 MHz to 1.5 MHz, which is equivalent to a reduction of phase noise influence on phononic occupation by a factor of ≈ 3 (if the occupation is completely limited by the laser phase noise).

In our future work, this reduction might prove to be insufficient. However, since the phase noise reduction is essentially limited by fiber noise only, we should be able to achieve a significanly better result by cryogenically cooling the fiber loop. For this we might need to develop a technique for cooling that does not affect the overall stability of the fiber loop, but we might be able to achieve this with better mechanical design that involves an unjacketed fiber.

CHAPTER 8

FILTER CAVITIES

> A filter can make anything look good, but it's what's underneath that counts.(a)
>
> UNKNOWN / CHATGPT

(a) Please note what I did here.

We present the history, design, construction, debugging, and performance of our ultra-narrowband filtering system. These results were one of the major points of our publication, (I. Galinskiy et al. 2020a), from which we take several of the figures and some text.

8.1 INTRODUCTION

We need filter cavities in our experiment because the photons produced by the optomechanical system are mixed together with the pump photons, which is the unscattered laser light. When we send light to the optomechanical system, the probability of scattering is rather low. For a mechanical system in the ground state, this probability will be only one in 1 billion, which means that for every billion photons coming out of the system, only one will be a signal photon. Moreover, pump and signal photons are very close together in the frequency domain. Typically, they are separated by the mechanical frequency, which lies in the range of 1.4 MHz to 1.5 MHz, depending on the membrane that we're using. For context, this corresponds to about *1 billionth* of the base laser frequency that we're using (450 THz for 852 nm light).

8.2 OVERVIEW OF FILTERING TECHNIQUES

The need to separate the different frequency components is required by the fact that we are sending them to a single photon counter, a device incapable of distinguishing different frequencies of light. There are different ways of filtering light in optics. Some familiar examples are optical filters that one can buy off the shelf.

A common and well known example are colored glass filters, used for very rough filtering. For example, if one wants to disregard all the "daylight" from normal lighting in the lab, while keeping infrared laser light, one can use an infrared-specific colored glass filter. These filters have the advantage of being inexpensive and broadband. Unfortunately, this comes at a cost of a low efficiency, with 90 % transmission in the passband being a common trait(1).

Dielectric filters are a better option where efficiency matters. These devices consist of a stack of dielectric materials of different indices of refraction, where light interference is the main mechanism that creates a well-defined spectral response. A typical example is a dichroic mirror, a device that lets selected components of light through, while reflecting other frequencies. These mirrors can display very high transmission efficiencies, 99 % not being uncommon in the premium varieties(2). In addition, it is possible to engineer a rather narrow passband. Models exist with a selectivity of only 1 nm (so-called "line filters"), which are often used in Raman spectroscopy, where a strong pump laser is scattered in frequency by the molecular motion of a material under test. A line filter then allows to discard the pump light, while retaining Raman-scattered signal that might be analyzed by a spectroscope. Filtering is required in this case, since Raman scattering is a low-probability process in most materials, necessitating the use of a powerful excitation light source. If not filtered, the pump light will inevitably saturate or damage the sensitive spectroscopic equipment downstream. Later, we will see that optomechanical processes in our experiment are precisely Raman processes.

Bragg gratings are even more selective elements, consisting of a piece of dielectric material with an internal structure that displays a periodically varying refractive index, akin to the usual dielectric filters. Their performance comes from their construction, where a physically larger space accomodates a much greater number of refractive index "layers". This layered structure is not created by sequential deposition, but rather through a process that allow one to "record" the structure in an existing piece of material. Notice the similarity to acousto-optic modulation, where an strong acousting wave creates a varying index of refraction in a crystal. Volume Bragg gratings can can be made very efficient and selective, with a passband down to tens of gigahertz. Another advantage is the possibility of tuning the center frequency of the passband by varying the incidence angle of the incoming light. Nevertheless, 10 GHz of selectivity is still too broad for the requirements of our experiment, where we require strong rejection of light only megahertz away.

Finally, we come to the category of optical filters that rely on optical resonance. This category is uniquely rich, with device sizes ranging from microfabricated ring resonators(3), all the way up to the massive 16 m-long filter cavities at LIGO that take up entire rooms(4). For our purposes, we will restrict the attention to **Fabry-Pérot free-space optical cavities**. As we

(1) For example Thorlabs FGL780M, used for daylight suppression

(2) For example Thorlabs FBH850-10, which we use in our experiment prior to single-photon counting

(3) Barwicz et al. 2004.

(4) McCuller et al. 2020.

have descibed in the chapter on optical resonator basics, these seemingly simple contraptions consist of two high-reflectivity mirrors separated by a precise distance, often finely controlled by a piezo actuator which allows one to tune that separation on a picometer scale to maintain resonance. Our requirements typically lead to a construction that is "highly macroscopic" and employs low-loss mirrors, leading to narrow kHz-scale resonances. For a concrete example, our system's resonators have a bandwidth of only ≈ 30 kHz.

8.3 FROM A SINGLE CAVITY TO A CASCADE

8.3.1 Motivation

To reiterate, our experiment needs strong rejection of better than ≈100 dB at a detuning of 1.5 MHz (and some rejection for the nearby mechanical modes, but more on that later). A first approach would be to use only one filter cavity, but with a very narrow bandwidth. For example, one could make a physically large Fabry-Perot resonator with ultra-high-reflectivity mirrors, leading to a linewidth of, say, 10 Hz. Problem solved? Unfortunately, no. Such narrow response comes with a cost. First of all, experimentally, it's difficult to create such devices: the stability of a large mechanical system gets worse and worse as the size increases. And even if we disregard that limitation, we're confronted by the fact that a Fabry-Pérot cavity with a very narrow linewidth has, by the very definition, a narrow bandwidth. Optomechanically scattered light, on the other hand, has its own bandwidth. Typically it's on the order of 10 kHz during our experimental runs. This mismatch of bandwidths would lead to severe inefficiency, where we would **lose** 99.9 % of our signal and make measurements effectively impossible .

The solution to this problem, as this section's title suggests, is to have a cascade of filters, where light passes sequentially through several separate resonators. What we have in our system is a system of four cavities, each one having a linewidth of 30 kHz. That linewidth is quite larger than the bandwidth of the signals that are being generated and processed (10 kHz). Even more importantly, the rejection of the system as a whole grows *exponentially* with the number of cavities. Four cavities, each with a rejection of 30 dB, would lead to an overall rejection of 120 dB! And to top it all off, the time delay introduced by a cascade increases only *linearly* with the number of cavities.

All of the above makes the decision to use a multi-cavity filter system a "no-brainer". Let us now talk about how this system was built.

8.3.2 First generation, or the forgotten bandgap

In this section, we will describe the first version of our filter cavity system that we dubbed "Fermi's Paradox" (because one of the solutions to Fermi's Paradox is the concept of Great Filters). As we mentioned above, this is not the version currenly in use in the experiment. Nevertheless, the core ideas and techniques were transferred almost without change to the next version. Therefore, a thorough description of this first version will make subsequent information much easier to grasp. Without furter ado, let us begin.

As we said earlier, we require approximately 100 dB of attenuation for the ≈1.5 MHz-detuned pump, as compared to signal. With 4 cavities, this results in a maximum bandwidth of ≈100 kHz for each cavity. The technical challenges to be solved can be split into two broad categories, and further split into subtasks (it's an engineering fractal all the way down):

1. Design of individual filters:
    a) Mirrors: the main components of optical cavities. We require high-reflectivity, low-loss mirrors to achieve high finesse. "High finesse" in this case is necessary to be able to construct cavities with a manageable physical length, as for a given bandwidth, the length of a cavity is inversely proportional to its finesse.
    b) Spacer: the mechanical support for the mirrors. While often omitted from theoretical considerations, having a robust and mechanically stable way of mounting the mirrors is as crucial as the mirrors themselves. A "shakey" or "driftey" spacer will make the cavities impossible to stabilize, leading to joy not being sparked.
    c) Piezo actuators: the way to maintain resonance. With our finesse values, a change of merely ≈50 pm of cavity is the difference between being on resonance (100 % relative transmission) and being 2 linewidths off-resonance (only 6 % transmission). For this reason, we need a way to finely tune that length, which is where piezo actuators come into play.
    d) Suspension, crucial for preventing the cavities from succumbing to the unrelenting force of gravity, and falling onto the floor. A proper way to fixture the components can make-or-break an optical system, and our resonators are no exception.
2. Interplay between individual filters in a composite system:
    a) Inter-cavity isolation. Contrary to early experiments in the field of optics, the coherent fields and modes in our work make interference a double-sided coin. Interference enables our experiments. When not accounted for, however, *everything* wants to be an interferometer. It is crucial to prevent interference from happening in non-controlled areas of the experiment, in this case between the cavities.
    b) Mode-matching. To properly propagate through a cavity, its input light has to match the resonator's own mode.
    c) Multi-cavity locking. While many techniques exist for stabilizing ("locking") a single optical cavities, most of them need to be modified, or straight-up abandoned, to be useful in a cascaded arrangement. Custom electronics and logical schemes allow us to maintain the filter cascade locked on a single frequency.

We will tackle these problems one at a time, roughly corresponding to the chronological order in which they were developed.

8.3.2.1 Mirrors

We have discussed the theory of optical Fabry-Perot resonators before. To reiterate, a high-finesse, high-transmission cavity requires mirrors with the following properties:

1. High reflectivity. This directly translates into finesse.
2. Low loss. As we defined before, "loss" is all the light energy that has not been reflected or transmitted through the dielectric coating. This includes absorption and scattering.
3. Radius of curvature. This is a design choice more than a property, and can be selected during a mirror's fabrication. It is still important to keep it in mind, as a poor choice of the ROC can, in the worst case, lead to an impossible cavity geometry. More realistically, a "wrong" mirror ROC can severely limit one's ability to change the cavity geometry in the future, and flexibility is of paramount importance in the experimental science.

With all that in mind, we have chosen Layertec GmbH as our supplier, and ordered mirrors with the following specifications:

- Standard "half-inch" substrate with on outer diameter of 12.7 mm, center thickness of 6.35 mm, ROC 700 mm
- Transmission of ≈380 ppm at 852 nm. Note: we ordered 600 ppm transmission, and Layertec "overdelivered". While we didn't expect such a transmission, this ended up helping us in the long term.
- AR-coated on the other surface, with R <0.05 % at 852 nm.

To confirm the company's test report, we directly measured the transmission at a series of wavelengths, and obtained matching results, shown in Fig. 8.1.

More accurate measurements are obtained in a cavity using the Quasi-Ringdown technique, indicating an intracavity *loss* of (365 ± 2) ppm per mirror for the LF01-LF02 mirror pair. An example of such a measurement is shown in Fig. 8.2.

All of the above shows that the mirrors are performing according to specifications.

8.3.2.2 Spacer

There is a whole area of research out there dedicated to designing spacers for optical cavities. A lot of that research is focused on highly sophisticated reference cavities used in quantum metrology, going as far as fabricating spacers out of single crystals of silicon, with cryogenic cooling and optical fiber suspensions(5). Other research looks into making exceptionally stable and isolated cavities out of ultralow expansion glass with triple thermal shields in ultrahigh vacuum. We do none of that.

Our cavities require neither year-long stability nor consider thermal noise effects on the resonance frequency of the filters. We are simple people:

(5) W. Zhang et al. 2017.

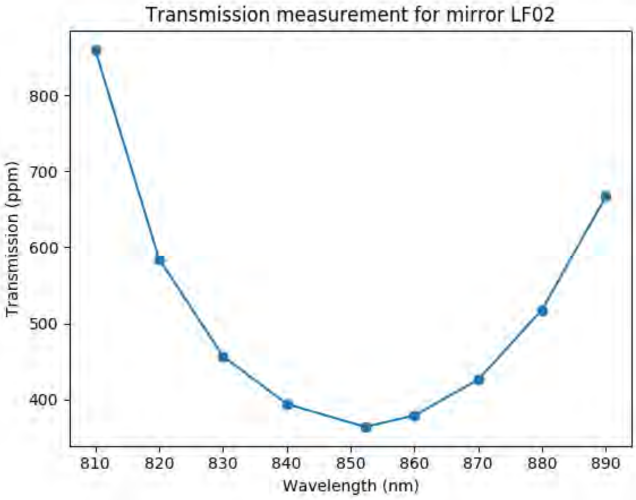

Figure 8.1: Directly measured transmission of a high-finesse mirror from Layertec. Minimum transmission is achieved at 852 nm

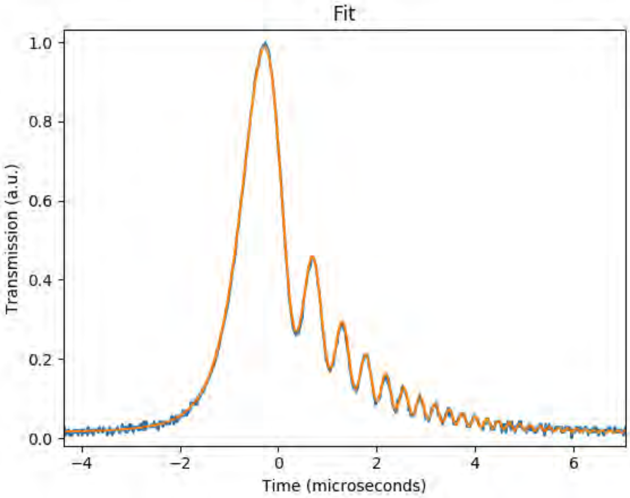

Figure 8.2: Typical oscilloscope trace during a QuasiRingdown sweep. The transmission of the cavity oscillates as its internal field interferes with the frequency-swept incoming light.

we see not shake - we happy. The design we went for is as uncomplicated as a crowbar. To be a bit more precise, let us list the thoughts we had during design:

- Mechanical stiffness. With a length of 15 cm, simply using a thick enough rod of some metal is enough.

- Thermal stability. This is the slighly exotic part of our approach, where we opted for an invar-based design. Invar is a Nobel-prize-winning alloy of iron and nickel that displays a surprisingly low coefficient of thermal expansion of less than 1.5 ppm/K. Compare that to steel (≈15 ppm/K) or aluminium (≈20 ppm/K). Additionally, it is nearly as stiff as stainless steel(6).

- Ease of fabrication. Metals are worked much more easily than glass, are much cheaper, and are readily available off-the-shelf.
- Ease of assembly and disassembly (ominous foreshadowing). With so many unknowns, it is crucial for us to be able to service our cavities for modifications, cleaning, and other changes.

In the end, our design is mostly an invar tube with a cylindrical bore in the center, and mounting fixtures on the ends. When assembled and mounted on the table, it looks like shown in Fig. 8.3.

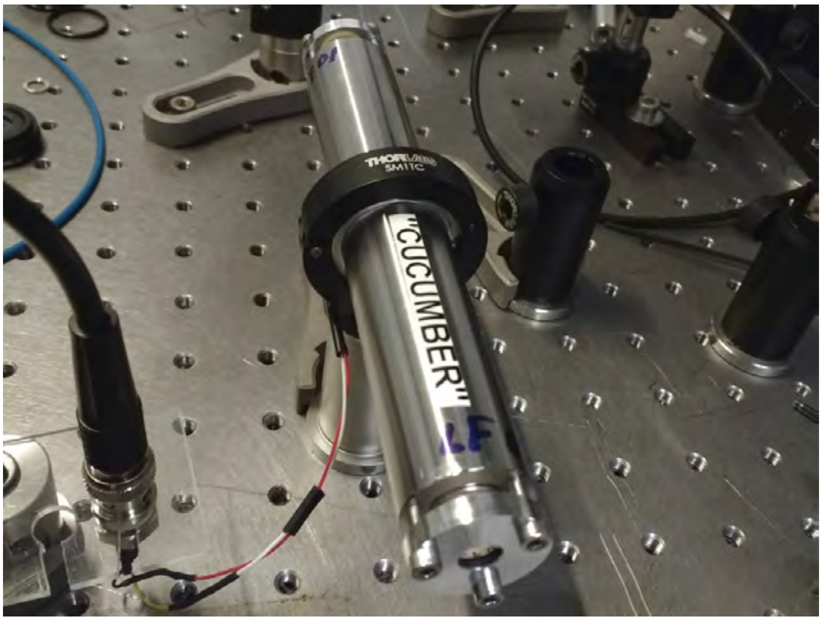

Figure 8.3: A first-generation filter cavity in its natural habitat, mounted by the center to minimize vibration. One can see the end clamps that hold a mirror on each end, plus a piezo on one of the ends. Piezo cables are visible. Name "Cucumber" was chosen as it starts with "C", indicating it's our third cavity, chronologically speaking. In the filter system, it's the first cavity in series.

The mounting ends are simple as well. They are composed of the following, left-to-right:

1. Clamp piece made of aluminium. This piece is not part of the cavity length, and can therefore be made without regard to thermal expansion.
2. Rubber o-ring that evenly distributes the load on the mirror, dampens the vibrations of the clamp, and prevents scratching of the mirror by the aluminum.

(6) Different manufactures provide slightly different numbers, but they are all close enough for our requirements

3. The mirror itself. Due to its radius of curvature, it only contacts the spacer body on its circumference, which allows us not to worry about any scratches on the reflective surface.

4. Three mounting holes for screws that keep it all together. Note that we chose 3 holes instead of the more conventional 4-hole arrangement. This is due to the fact that 3 mounting points always define a plane. Therefore, tightening any one of the screws does not lead to any of the other screws becoming loose

The other end of the cavity is similar, but also includes a piezo actuator "sandwiched" between the spacer and the mirror, therefore allowing for cavity length tuning. Here, the o-ring plays an additional role: being relatively soft, it does not significanly impede the micrometer-level motion of the mirror, while applying an even preload that makes the piezo response more linear.

8.3.3 Suspension of the first generation of filters

As mentioned above, unsuspended cavities tend to fall down under typical experimental conditions (7). We will now briefly describe the suspension design for this first generation of filters. Since the suspension for the second generation of filters is quite different, we shall not go into too much detail here.

The main considerations when mounting any sort of optical system is the long-term stability of the mount, and the resistance of this system to vibrations and other extraneous perturbations. We have chosen an approach common in high-stability reference cavities, which is clamping in the middle of the cavity. Of course, high-stability reference cavities require a much deeper understanding of internal stresses, aging, and the precise way in which external forces affect the system. But as stated before, our needs are not nearly as strict. For our practical purposes, this way of suspending has two main advantages:

- A single mounting point ensures that external mechanical vibrations from the optical table are "sampled" only at a single point, therefore preventing any stretching or bending modes of the table from affecting the cavity.

- When suspended from the middle, vibrations along the axis of the cavity result in stretching of one half, but also a corresponding shrinking of the other half. This results, under ideal conditions, in a net zero change of cavity length(8). This is the main reason why this technique is popular in metrology-grade reference resonators(9).

In practice, cavities mounted in this way displayed great stability and were easy to operate, even in presence of vibrations on the table due to people working with the optical setup at the same time. This suspension is shown in Fig. 8.3.

(7) citation needed

(9) Jie Zhang et al. (Mar. 7, 2013). "Design of an Optical Reference Cavity with Low Thermal Noise Limit and Flexible Thermal Expansion Properties". In: *The European Physical Journal D* 67.2, p. 46. ISSN: 1434-6079. DOI: 10.1140/epjd/e2013-30458-2. URL: https://doi.org/10.1140/epjd/e2013-30458-2 (visited on 02/25/2023).

(9) Also valid for non-static displacements, as a perfectly centered suspension will not excite any odd mechanical modes, therefore not changing the length of the cavity under idealized conditions.

8.3.4 Locking

Finally we come to the crux of the biscuit. A high-finesse optical cavity is not trivial to stabilize to the laser light. We will reiterate the technical challenges:

1. The high finesse ($\approx$ 8800 in our case) implies that a single resonance only spans a tiny fraction of the full spectral range (FSR).
2. The absolute length of the cavity can vary over time due to thermal drifts and other effects. Therefore, we need to be able to adjust the length by at least half of an FSR. In practice, being able to adjust the length by several FSRs is necessary for prolonged stability and ease of operation. This means that a single resonance is an even smaller proportion of the whole scan range.
3. Cavities with a small linewidth are particularly susceptible to any frequency noise of the laser source, needing prestabilization even for relatively "quiet" lasers.

These challenges require us to be very careful with noise and other spurious signals coming from the outside (more on that later). Additionally, locking 4 cascaded cavities comes with extra complications:

1. Pound-Drever-Hall locking cannot be used, as the sidebands necessary for the error signal would be filtered already at the first cavity. Adding additional modulators between the cavities could be one solution, but it would increase the losses of the whole system, as well as being rather expensive and bulky.
2. Side-of-fringe locking cannot be used either, as on-resonance locking is not really possible. Settling for slightly off-resonance locking would, again, increase losses substantially.
3. Injecting locking light into each cavity independently would require us to have many shutters, increasing the complexity.

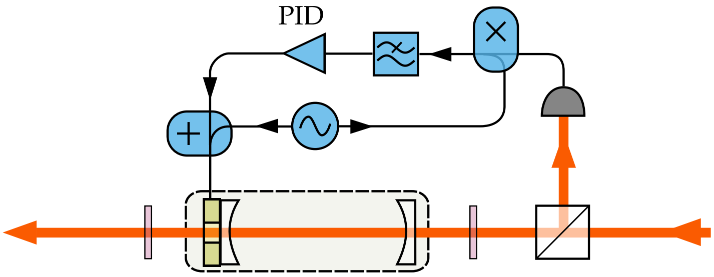

Figure 8.4: Scheme for locking a single cavity. Adapted from the supplementary material of (I. Galinskiy et al. 2020b)

Fortunately, there exists a different technique that we call "dither locking", and it is used in other experiments where external modulation is impractical. We will first describe its use on a single-cavity lock, since the multi-cavity case is a straightforward extension of this method. The concept, illustrated in Fig. 8.4, is rather simple:

1. A low-frequency, low-amplitude modulation is applied to the cavity's piezoactuator. This results in a periodic variation of the cavity length. The amplitude of this modulation is low enough such that the cavity does not change its resonance frequency by any significant amount when compared to the resonance linewidth.
2. This periodic variation results in a variation of cavity reflection (or transmission). Assuming low enough modulation, we are effectively sampling the *derivative* of the transfer function. This derivative is zero both when on resonance and far away from resonance, while displaying a steep slope around the resonance, as shown in the figure below.
3. The resulting variation of reflection is measured by a photodetector, converted to an electronic signal, and then demodulated, therefore recovering the derivative. This is our error signal used for locking, which we call "dither signal". Our goal is to maintain this signal as close to zero as possible

An experienced or attentive reader will notice that this signal cannot be easily used for locking per-se, since it is close to zero both on resonance, and far away from it. We are now in position to show the full locking sequence that addresses this limitation:

1. The cavity's piezo (for brevity, we will only refer to the "cavity" in subsequent text) is swept across the entire range, while recording the reflection as function of control signal. This locates all the resonances, which appear as narrow spikes in the trace.
2. A target resonance is chosen close to the center of the sweep. This gives plenty of "wiggle room" for long-term drifts to both sides. The height of the resonance is recorded.
3. A finer, smaller sweep is performed around this chosen resonance, and the height of the resonance is corrected, as a fast sweep can make this height appear smaller due to ring-up/ring-down effects and the limitations of data acquisition speed.
4. The setpoint is set to half-fringe, with reflection being the error signal. A slow "catching sweep" is initiated on one side of the resonance, a safe distance away. The lock then free-drifts ("integrator drift") until the lock "catches" the side of the fringe.
5. If the successful lock capture is confirmed, and is stable, modulation is turned on at a frequency between 1 kHz and 2 kHz. The resulting demodulated signal is recorded, and its strength is used for gain calculations.
6. Now we are in range of dither-locking. The locking electronics are commanded to transfer the lock to dither mode, and the cavity is stabilized on resonance. If this condition remains stable, the lock is deemed

successful. If something goes wrong, the entire sequence is performed again.

All of the above typically takes about 10 seconds and is fully automated. Ironing out the dither locking of a single cavity was the most labor-intensive part of the control electronics, where we tackled noise, resolution, stability. The codebase, composed of Python for high-level computer control, and C++ for the embedded counterpart, ended up being more than 1500 lines of code. Bloody, sweaty code. I'm mentioning that because if I were to redo the experiment, I would go for a different approach based on Red Pitayas. However, back in that time I lacked some experience and knowledge, so I ended up going the long route. Live and learn.

8.3.5 Multi-cavity lock

As we said, the above was the hardest part of the lock design. To lock several cavities in series, the previous concept is taken almost as-is, but with following additions:

1. The dither frequency of each cavity has to be different from the other ones, as otherwise modulations would be indistinguishable from each other.
2. Locking has to be performed *sequentially*. All cavities, with the exception of the first, rely on light already propagating through the previous filters. Therefore, we wait until a cavity is fully locked before attempting to lock the next one

Other than that, the locking process is the same. We will now describe the next generation dubbed "NQLBS", or "Not Quite LIGO, But Still". The name will be evident soon.

8.4 NQLBS, OR THE REMEMBERED BANDGAP

Remember how we wanted to reject the pump beam? That is still the case, but we have forgotten something: the bandgap of the membrane. It is true that the bandgap is a pretty quiet area around the high-Q mechanical resonance. However, the width of the bandgap is finite. Here's the problem: low-Q mechanical modes just outside of that bandgap are **too close to the high-Q mode**. This means that when the filter system is centered on the main mode, **they still allow scattered light from the low-Q mode to leak through the** 100 kHz **cavities**. To be honest, we simply overlooked this fact, thinking of the membrane as a simple harmonic oscillator (which it absolutely is not, containing a myriad of modes). The result? The photon rates were way too high and dirty.

The weak signal from the main mode was overwhelmed by the signals from those other modes. Of course, they are much weaker than the unscattered light of the laser, but they are also much closer in frequency. Since a single-photon counter, by definition, cannot distinguish between different light frequencies, we thought for a long time about how we could improve the situation without building a new set of filter cavities. In the end, however, no easy solution was found. And by "simple" I mean a solution that would filter the unwanted components **without** introducing noise. We considered schemes like EIT, which can be used to produce very narrowband filtering. Unfortunately, in addition to the complexity of an atomic system capable of producing EIT, the nature of atomic transitions is such that the atoms would still create some photons due to decoherence, which would contaminate our filtered signal, precisely the problem we are trying to avoid. In the end, we decided to "bite the bullet", and build a system of cavities with a much narrower linewidth. That is, longer filters.

8.4.1 The long boys

Fortunately, we could reuse the mirrors from the previous system, but now made the cavities 4 times larger. To remind you, first system had 15 cm long cavities, and ≈110 kHz of bandwidth. The new cavities are 60 cm long, which is pretty big by optical bench standards. But the linewidth is now ≈30 kHz. So they would transmit our signal just as efficiently, while rejecting the nearby out-of-bandgap modes quite well:

A little bonus is that they reject the pump light even more (>155 dB), though that is completely overkill.

8.4.2 Fabrication

Let us go into the nitty-gritty of actually making NQLBS real. The sheer size of these filters is such that it was no longer possible for the university's mechanical workshop to make them out of a single piece of material. Imagine drilling a 60 cm-long hole of only 5 mm in diameter in the steel-like invar. Sure, it's possible using some relatively exotic fabrication techniques like electrical discharge machining, but after consulting with people at KU's mechanical workshop, especially Dennis Westphal Wistisen, we decided to split each cavity into three pieces. As before, invar is our material of choice. However, the separated segments still need to be assembled, for which we use threaded connections:

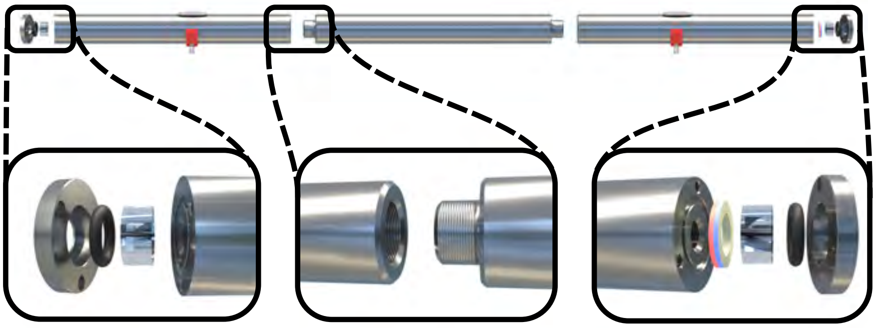

Figure 8.5: Construction of a full-sized 60 cm filter cavity

At the same time, the ends of the cavities remained effectively unchanged, with only a few quality-of-life features for easier positioning of the mirrors.

8.4.3 Mechanical stability: problem and desperate solution

Such long cavities come at a cost. In a nutshell: the longer a beam of material is, the lower its stiffness, and the lower are the frequencies of the mechanical eigenmodes of vibration of that system. As a matter of fact, the stiffness of uniform beam of material(10) is inversely proportional to the **square** of the length of that object: making a cavity 4 times longer makes it 16 times less stiff (more "bendy"). In practice, that means we are suddenly much more sensitive to vibrations coming from the environment, vibrations of the optical table, fluctuations of air pressure, sounds, and so on. This resulted in not being able to lock these cavities when they were simply mounted on the optical bench.

After a bit of unsuccessful attempts at locking them, we realized that we needed to protect the cavities from the environment, both mechanically and acoustically. For acoustic protection, we built a system of vacuum tubes, into which we slide the cavities. Then, we pumped them down to a medium vacuum to remove any kind of acoustic coupling. As a somewhat unexpected bonus, their linewidth improved by 1 kHz to 2 kHz. It turned out that oxygen has a non-negligible absorption of light at 852 nm. Note that this also removed the effect of air pressure fluctuations due to atmosphere, wind, and even as little as closing and opening the door in the lab.

8.4.4 Spring suspension

Turns out acoustic isolation alone was not enough to be able to lock the cavities. There still remained a strong susceptibility to external noise at about ≈ 220 Hz, which was the first bending mode of the very long tube. Therefore, we needed to isolate them from the mechanical vibrations of the optical table. But note now that these cavities are quite heavy (about 2 kg each). This is where harmonic oscillators come into the picture again.

By placing a mass on a spring, vibrations of its support are suppressed above the resonant frequency. This idea was then to place the individual resonators on soft springs inside of the vacuum tubes. Such an arrangement forms a low-frequency mechanical oscillator with a frequency of approximately 10 Hz. Such an approach very effectively suppresses external vibrations at 200 Hz or above, and prevents them from reaching the filter cavity. As an attentive reader might expect, however, now we have a new kind of vibrations: the mass-spring vibrations at 10 Hz. In a way, we traded one problem for another. However, low frequencies are easier to manage, so we have decided to dampen them.

We introduced a damping material between the vacuum tube, and the cavity inside of it. Our first attempt was to use polyurethane foam, which worked very well in suppressing these vibrations, so we could finally achieve a stable lock of the cavities. Our joy was short-lived, as we noticed a progressive degradation of cavity linewidths. As it turned out, polyurethane outgasses in vacuum, creating a thin film of contamination on the mirrors.

After one week of cleaning the mirrors, which involved us trying five different techniques, including ultrasonic acetone baths, and multiple iterations of First Contact™, we finally managed to restore their reflectivity. For that, we used the good old "tissue with acetone and wipe with the finger" techni-

(10) James M. Gere and Barry J. Goodno (Jan. 1, 2012). *Mechanics of Materials*. 8th edition. Stamford, CT: Cengage Learning. 1056 pp. ISBN: 978-1-111-57773-5.

que. As a matter of fact, this latter approach actually increased the finesse beyond what the mirrors had "out of the box", likely indicating that there was some contamination either from the factory, or from our handling (more likely). We observed linewidths of 28 kHz.

We still needed to find a new material to dampen the 10 Hz vibrations, but without outgassing in vacuum. Now, there exist materials specifically engineered for similar purposes (targeted at space applications), but they are rather exotic and unavailable for many places. In the end, we decided to simply try a couple of other materials. As expected, we ended up contaminating the mirrors a few more times, but at least we knew how to clean them.

Finally we found the material that worked, and it came from an unlikely source. It was simple cotton (cellulose) bought in a pharmacy(11). Before using it, we washed it with several solvents, to be sure that we removed as much volatile material as possible. Then we placed the cotton in a dedicated vacuum chamber to outgas anything that remained, particularly remainders of solvents from the wash. Finally, we placed little pieces of cotton on top of our optical resonators and covered them with Kapton tape to prevent them from getting loose. With this, the cavity system was finally stable and lockable. The suspension is shown schematically in Fig. 8.6, and each cavity has two suspension points, positioned at its Airy points to prevent mirror tilting during vibrations(12)

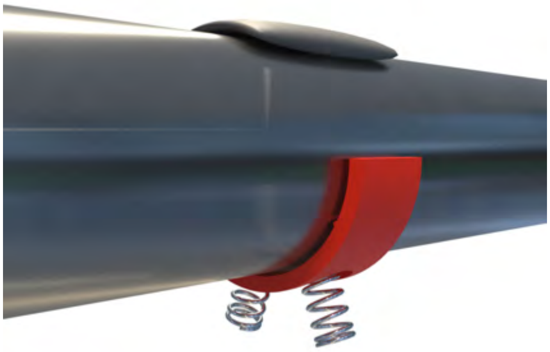

Figure 8.6: Schematic of damped spring suspension for filters. Adapted from (I. Galinskiy et al. 2020b)

8.4.5 Optical arrangement

In the discussions above, we have skipped some details on the actual optical arrangement of the system. We have several Fabry-Pérot cavities in series, which means that one has to take care not to create interference *between* the cavities, as that will destabilize the whole setup. The issue here lies in the fact that a system of 4 cavities in series is actually a series of 7 cavities, if one

(11) Nørrebro Apotek, Nørrebrogade 8, 2200 København, Denmark

(12) Airy points are support points on a beam that minimize angular deflection of the beam's ends under vertical loads. For an application, see e.g. J. Zhang et al. (2013)

counts the inter-cavity spaces. As our mirrors are high-reflectance, and we strive for as little loss as possible, these inter-cavity spaces form resonances of their own. In contrast to the actual cavities, however, the inter-cavity spaces are not controlled, and are in open space. Even if they were controlled, we would find ourselves in a situation where we would have to control 7 *coupled* resonators, which is a formidable task.

The solution to this issue is to isolate the individual filters. One way to do it would be to straight-up place Faraday isolators between the cavities, but that comes at a disadvantage of added loss (isolators are rarely more efficient than 92 %(13)) and literal cost. The technique we use is simpler and, though not as "general" as the symmetry-breaking Faraday isolators, is much more efficient and cheap. We call it "the poor man's isolator", which consists of a simple arrangement of a polarizing beamsplitter (PBS for short) and a quarter-wave plate. It is a well-known technique in quantum optics, but we shall look at it in the context of inter-cavity application, as illustrated in Fig. 8.7.

(13) *NIR Free-Space Isolators (690 - 1080 Nm)* (2023). URL: https://www.thorlabs.com (visited on 02/24/2023).

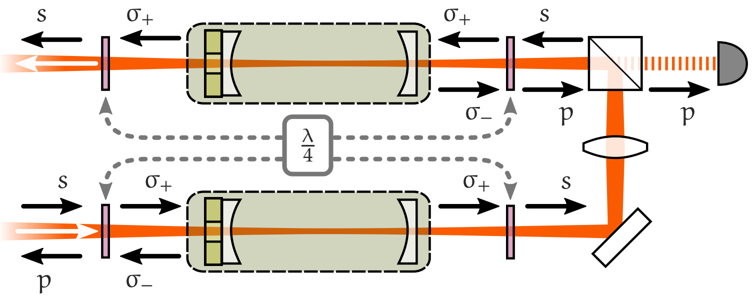

Figure 8.7: Schematic of inter-cavity coupling and isolation. Assuming light coming in from the bottom, as indicated by the white arrows, it passes through the bottom cavity, and is converted into s-polarization, which is reflected by the polarizing beamsplitter into the second cavity. Any reflections from that second cavity are converted into p-polarized light, and transmitted though the beamsplitter onto the photodetector, therefore preventing any inter-cavity interference. Circular polarizations σ_+ and σ_- are chosen for concreteness, but can be swapped without affecting functionality.

The principle of operation is based on the fact that upon reflection, a circular polarization flips (i.e. changes from right circular to left circular, or vice-versa), and was discussed previously. The beamsplitter also acts as a mirror, redirecting the light into the second cavity. As a bonus, polarizing beamsplitters are typically highly efficient (> 99 %) when operating in reflection, which is useful for keeping the overall efficiency as high as possible. A little sidenote: this high efficiency comes at a lower polarization extinction, but is of no issue to us, as the incoming light is already rather pure s-polarized light. With this setup in place, interference between different cavities disappears and makes them independent, which is a requisite for locking, and also has the pleasant side-effect of redirecting the reflected light onto a detector, so there is no need to sample the beam separately, which is always a lossy process.

Another sidenote for the those interested: this scheme would not work as well if the cavities had any birefringence in them. Birefringence splits the optical resonances, and effectively introduces undesired frequency-dependent polarization changes, which would compromise the "poor-man's isolator" performance. In free-space optical cavities, this birefringence happens due to birefringence in the mirrors or their coatings, usually due to some stress produced by the fabrication process. Fortunately for us, we do not observe such effects, and can consider the cavities to be isotropic with regards to polarization.

8.4.6 Input to filter system

Before letting the light into the filtering system, we need to make sure that it has access both to the locking beam, and the signal beam coming from optomechanics. We do it in a simple way, as illustrated in Fig. 8.8. Both beams, initially in orthogonal linear polarizations, are combined on a polarizing beamsplitter, where the signal is reflected(14) into the common beam, while the lock beam is transmitted. The combined beam is then passed through a half-wave plate, which we adjust such that the polarizations are almost swapped, such that the signal beam becomes almost completely p-polarized. On the next PBS, the polarization is collapsed onto its p-state, which allows most of the signal beam to pass through, while dumping the majority of the lock light. Since lock light is "cheap", we can always compensate for it by increasing the level of lock light input. In the end, the combined lock and signal beams have the same polarization, and can be "fed" into the filter cavity system.

It is worth noting that this arrangement might seem a bit crude for the task, as we do not need to have both beams enabled at the same time, so one could use a scheme using some kind of optical switch, like an acousto-optic modulator, or a Pockels cell. However, the amount of lock light needed for our operations is rather low, on the order of 10 µW. That means that by starting with about 1 µW of lock light input, we can obtain an efficiency of 99 % for the signal beam (apart from other inevitable losses). This is the reason why we didn't go with any more involved scheme.

In the single-photon measurement stage, the lock beam is blocked by a shutter, as shown in Fig. 8.8, after which the signal shutter is open. When the cavities are being locked, the reverse happens: the signal is blocked, and the lock is open again. Notice that it is not strictly necessary to block the signal beam during locking. However, the lock beam has the nasty property of being *exactly* resonant with the optomechanical cavity, by definition. If even a tiny bit of it gets back to the optomechanics (and it does), the membrane gets excited, which is exceptionally annoying. For this reason, the signal shutter was installed, and it keeps our systems much more isolated.

8.4.7 Shutters

We have already mentioned that our cavities operate in a sequenced fashion, with locking "frozen" during single-photon counting, followed by a short period where the locking light is on, and the lock is restored. Needless to say, we cannot allow this relatively strong locking light to propagate to the single photon counters, as it would instantly saturate them (SNSPDS) or destroy them (APD). The only practical way to reduce a "macroscopic" beam of light

(14) PBSs are much more efficient in reflection

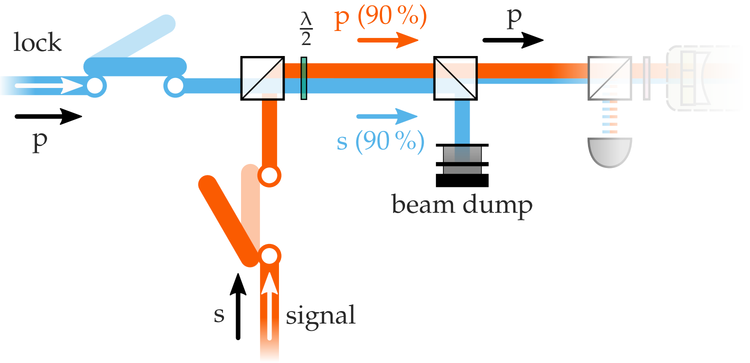

Figure 8.8: Input to filter system. The switch-like symbols represent optical shutters, with the default state solid (locking), and counting state as semitransparent. All beamsplitters are polarizing. The quantity of 90 % is only indicative, as we routinely operate at higher efficiency levels.

from its nominal level of $\approx 4 \times 10^{12}$ photons per second to less than one photon per second, is to use a mechanical shutter.

We based our design heavily on the work of (G. H. Zhang et al. 2015)(15), who designed a 3D-printed mount and blade, and used a cheap small DC motor for the actuation. Interestingly, this DC motor is nothing special: if turned on, it will simply spin normally. Their design incorporates stops in the 3D-printed mount, stopping the rotation of the blade at determined positions. During switching, the motor is briefly overdriven to quickly move it to the other position. In order not to overheat it during idle times, a simple parallel resistor-capacitor network is used. The capacitor allows for fast transients necessary for switching, while the resistor maintains a constant "maintenance" current that keeps the blade in its desired position.

Since our initial experiments with the original design from (G. H. Zhang et al. 2015), we have adapted the design to be a bit more quiet in the vibration sense, incorporating a "wiggly leg" that serves as a spring to prevent kicks of the shutter from propagating to the optical table. Additionally, we increased the size of the blade, and removed the aperture to allow for easier alignment, as shown in Fig. 8.9.

We discovered that a simple 3D-printed blade cannot block light in its entirety, even when printed with a black filament. Therefore, we made the shutter blade as a scaffold (Fig. 8.9a) onto which we later apply aluminum-backed blackout tape(16), which solves this problem (shown installed in Fig. 8.9b).

8.4.8 Lock freezing and passive stability

We have established that having the locking beam on during single-photon measurements is a big no-no, as it would overwhelm the single-photon counter. There are ways of going around this:

1. Using a vastly different wavelength of light for locking, allowing it to be filtered out prior to photon counting. This filtering can be done

(15) Grace H. Zhang et al. (2015). "Note: Fast Compact Laser Shutter Using a Direct Current Motor and Three-Dimensional Printing". In: *Review of Scientific Instruments* 86.12, p. 126105. DOI: 10.1063/1.4937614. eprint: https://doi.org/10.1063/1.4937614. URL: https://doi.org/10.1063/1.4937614.

(16) Thorlabs T205-1.0

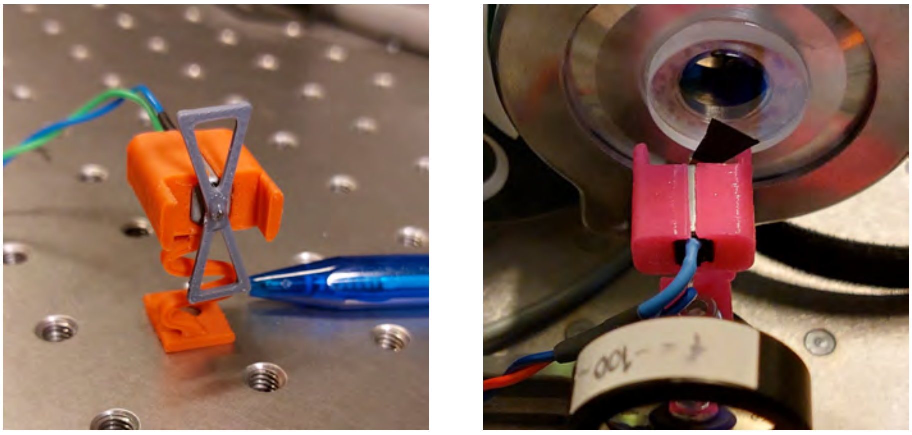

(a) Bare shutter, showing the 3D-printed structure and blade. No blackout material is installed yet to display the construction of the blade. Ballpoint pen for scale.

(b) Same version of the shutter in different colour, with blackout tape applied. Shutter is installed after the output of the filter cavity system.

Figure 8.9: Photos of the new design of shutters, currently used in the experiment

e.g. dichroic filters. The downside to this solution is the need to keep the locking light at a constant frequency offset from the desired offset, with a kHz-scale error at most. This task is highly nontrivial, requiring either a transfer cavity (17), optical comb, or some other technique. Additionally, the filter cavities are not exactly the same length, so their resonances will overlap very rarely.

(17) See e.g. Li et al. (2020)

2. Simply turning off the lock light. This requires the cavities to stay stable during this period, which we call "freeze". The disadvantage is that during that period, we are essentially "blind", and cannot know how far away these cavities have drifted. Also, they have to be periodically relocked. We chose this approach.

From here, we will use some text from the supplementary material of I. Galinskiy et al. (2020a). In the lock-freeze regime, active piezo feedback is paused and the reference lock light is disabled. The cavities' length then evolves freely, and it is crucial that all cavities remain sufficiently close to their resonances during the relevant timescale. The invar construction and vacuum environment reduces temperature drifts, and removes air pressure effects. Nevertheless, drifts still happen on a longer timescale. To compensate for these drifts, the electronic locking system not only pauses the locking, but continues to drift with the same speed as the drift before the lock freeze, which buys us some more stability time. For this purpose, we use a double feedback loop consisting of a primary loop that performs the locking, and a secondary "drift compensation" loop.

Drift compensation works in a rather simple way. The motivation for its operation is as follows: if there is some constant drift of our system, then the output of the primary loop will be drifting with it. If we differentiate the *output* of the primary loop, we will obtain the rate at which this drift occurs.

By integrating this drift rate, we recover the drift, which can be added to the output. Note that we are differentiating and then integrating, so effectively we are simply multiplying the signal by some constant during continuous operation. In practice, we add a lowpass filter to this second loop to remove high-frequency components, as we are only interested in long-timescale drifts. To perform the freezing, the configuration changes somewhat, as illustrated in Fig. 8.10

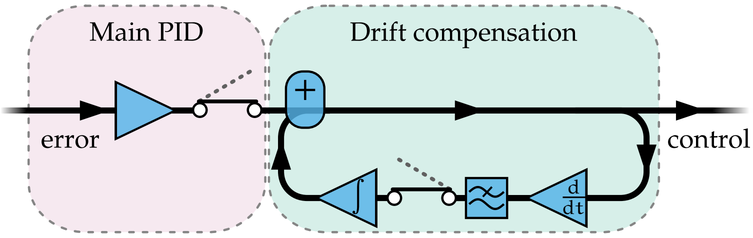

Figure 8.10: Diagram of the full lock for the filter cavities. The drift compensation section is engaged continously. During a freeze, the "switches" are open, disabling active locking, while the drift keeps getting compensated. The entirety of this functionality is implemented digitally using an Arduino Due board and an Analog Devices AD5780 digital-to-analog converter.

The lock beam is turned off by either disabling the AOM drive that produces it, or by physically closing it with a shutter. The latter was implemented later in the setup. As the AOM drive was already set up for this operation, nowadays we do both things, making *really* sure that no locking beam reaches the cavities.

As for the stability during lock freeze, we characterized it by simply leaving the lock beam on and measuring how the transmission decays as a function of time. Of course, the single photon counting was closed for this characterization. We performed the freeze sequence many times to accumulate statistics.

As we stated in the supplementary material of I. Galinskiy et al. (2020a), the relative transmission of the entire filter system decays to 50 % in more than 4 seconds, as shown in Fig. 8.11, and in 90 % of the cases, the relative transmission of the full filter system stays above 80 % for approximately 1 second.

8.5 CONCLUSIONS AND OUTLOOK

With all of the above, the reader will hopefully appreciate the effort that went into the design and construction of our filter systems. They were, perhaps, the most intricate single setup that the author had to construct, enabling us to do single-photon counting of signals painfully close to their noisy neighbors. With that said, there is still plenty of room for improvement. We will list several areas of this setup that still need some love and attention:

- Efficiency. While the current mirrors set an upper bound to the overall transmission efficiency of our system to approximately 50 %, there are other limitations at play. Mode matching, locking stability (partially

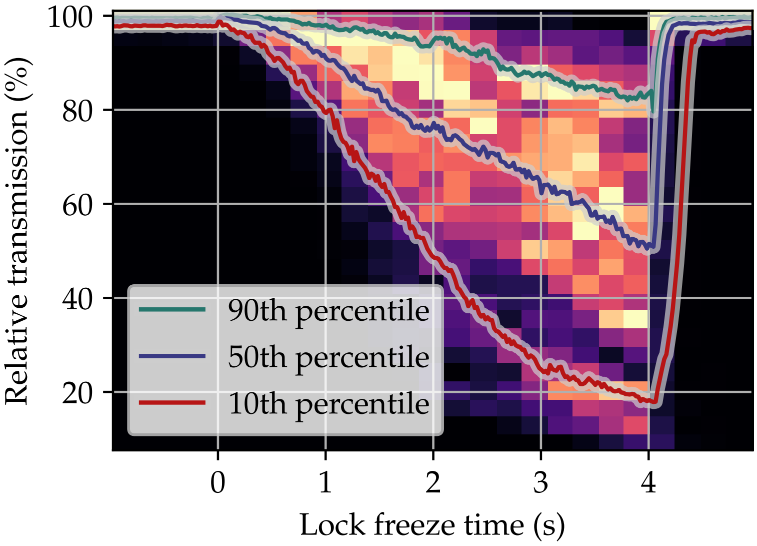

Figure 8.11: Transmission of the four-cavity filtering system over 4 s after freezing the locking feedback loop. Feedback is active for times before 0 s and after 4 s, showing the high passive stability of the system during lock freeze. The background color plot corresponds to the probability density of relative transmission. Figure reproduced from the supplementary material of I. Galinskiy et al. (2020a).

related to the stability of the laser), losses during fiber coupling and interconnections, and mechanical stability all add up quickly when there are four cavities, such that a realistic transmission is approximately 25 %. This results in longer acquisition times, especially for two-time and three-time correlations, whose rates degrade as the square and cube of transmission, respectively.

- Convenience of operation. Even though at the current stage the system is already quite automated, only requiring a single click to perform a full lock of all four cavities, better integration into our networked lab infrastructure will allow us to run the experiment with even less supervision, which is crucial during long acquisition runs.

Fortunately, all of the above can be solved with a bit of "elbow grease". The author hopes to get to that task as soon as more pressing and less explained issues are solved, which are described in subsequent chapters.

CHAPTER 9

THERMAL PHONON COUNTING

> Heat has a funny way of making you forget how to count - especially when it comes to calories and the number of drinks you've had.
>
> UNKNOWN / CHATGPT

This chapter is heavily based on our manuscript (I. Galinskiy et al. 2020a), and presents results in conversion of phonons into photons with their subsequent statistical analysis

9.1 INTRODUCTION

We shall now talk about our first successful experiment involving phonon counting. After we have completed the construction and debugging of the second generation of filter cavities, everything was in place to do some proof-of-principle work that would show the operational capacity of our overall system. In this experiment, we did not have pulsing, and our system was not completely in the sideband resolved regime, with $\Omega_m = 2\pi \cdot 1.48\,\mathrm{MHz}$ and $\kappa = 2\pi \cdot 2.75\,\mathrm{MHz}$. Even in this regime, however, ground-state sideband cooling is possible, although not to the level that sideband-resolved operation can allow. Instead, we focused on studying the statistics of photons that are created by the optomechanical system in steady-state read, and on confirming the level of "full-stack" performance that we have. The results were promising, and we published our findings in (I. Galinskiy et al. 2020a). In this chapter, we will use some of the figures and text of (I. Galinskiy et al. 2020a).

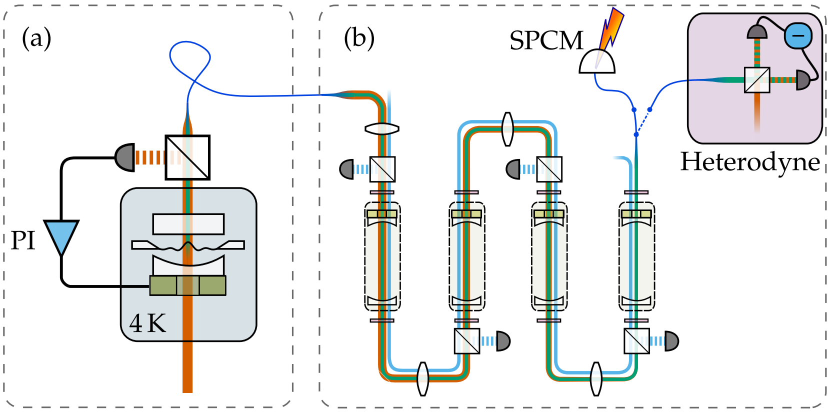

Figure 9.1: Experimental setup showing (a) the optomechanical cavity optically coupled to (b) four narrowband filtering cavities and subsequently directed to the single-photon detector (SPCM) or a balanced heterodyne detector. The optomechanical cavity is locked using a small portion of transmitted drive light (orange), with feedback provided by a PI controller connected to a piezo transducer. Filtering cavities are locked using an auxiliary beam (light blue). The filtered light (green) can be detected with photon counting (SPCM) or heterodyne detection. Figure adapted from (I. Galinskiy et al. 2020a).

9.2 THEORETICAL RECAP

While we have covered this topic previously in Chapter 4, we shall reiterate its results, relevant for this set of experimental results.

Thanks to cavity-based engineering of the optomechanical coupling, the interaction of light and mechanics is effectively dominated by a beamsplitter-like interaction between phonons and anti-Stokes photons:

$$\hat{H}_{BS} \propto \hat{b}\hat{a}^{\dagger}_{AS} + \hat{b}^{\dagger}\hat{a}_{AS}\,, \tag{9.1}$$

which leads to an exchange of optical and mechanical quanta, equivalent to anti-Stokes scattering of pump photons. This strong conversion of phonons into photons is the mechanism that both cools the mechanical resonator and maps its state onto light. Due to finite sideband resolution of the optomechanical cavity, there exists a small amount of two-mode squeezing interaction between phonons and Stokes photons ($\propto \hat{b}^{\dagger}\hat{a}^{\dagger}_{S} + \hat{b}\hat{a}_{S}$). This process introduces a small amount of heating that limits the minimum possible occupation of the mechanical oscillator under optical cooling Peterson et al. 2016. In practice, however, frequency-resolved detection of Stokes and anti-Stokes photons, particularly for low-frequency mechanical oscillators, is challenging due to the presence of numerous nearby mechanical modes and a strong optical pump field

The transition rates for the mechanical system can be calculated following Refs. (Wilson-Rae et al. 2007; F. Marquardt et al. 2007; Aspelmeyer, Kippenberg, and F. Marquardt 2014) as:

$$A_{\pm} = g_0^2 \bar{n}_{cav} \frac{\kappa}{(\Delta \mp \Omega_m)^2 + \frac{\kappa^2}{4}}, \tag{9.2}$$

where + (−) denotes upward (downward) transitions in the quantum harmonic oscillator ladder. The expected Stokes and anti-Stokes rates are then given by:

$$\Gamma_{\mathrm{AS}} = \bar{n}A_{-}, \quad \Gamma_{\mathrm{S}} = (\bar{n}+1)A_{+}, \tag{9.3}$$

with the dynamical optical broadening given by $\Gamma_{\mathrm{opt}} = A_{-} - A_{+}$. Remarkably, in the ground state ($\bar{n} = 0$) the rates become highly asymmetric, regardless of $A_{\pm}$. The ratio between Stokes and anti-Stokes count rates is unaffected by the overall system efficiency, thus we can estimate the residual phonon occupancy from these rates as:

$$\begin{aligned} \bar{n}_{\mathrm{est}} &= \frac{RA_{+}}{A_{-} - RA_{+}} \\ &= \frac{R((\Delta+\Omega_{\mathrm{m}})^2 + \kappa^2/4)}{((\Delta-\Omega_{\mathrm{m}})^2 + \kappa^2/4) - R((\Delta+\Omega_{\mathrm{m}})^2 + \kappa^2/4)}, \end{aligned} \tag{9.4}$$

with $R = \Gamma_{\mathrm{AS}}/\Gamma_{\mathrm{S}}$. Notably, both g_0 and the cavity photon number $\bar{n}_{\mathrm{cav}}$ cancel out in the estimator. Other parameters of the cavity are found via OMIT measurements, as described in great detail in (Nielsen 2016). The theoretical prediction for the expected final phonon occupancy can be calculated as:

$$\bar{n} = \frac{A_{+} + \bar{n}_{\mathrm{th}}\Gamma_{\mathrm{m}}}{\Gamma_{\mathrm{opt}} + \Gamma_{\mathrm{m}}}. \tag{9.5}$$

In our case of $\Gamma_{\mathrm{opt}} \gg \Gamma_{\mathrm{m}}$, two regimes can be distinguished. In the thermally-dominated regime, corresponding to $C_q \ll 1$, the ratio between the rates is determined only by the cavity response, leading to $R \to ((\Delta-\Omega_{\mathrm{m}})^2 + \kappa^2/4)/((\Delta+\Omega_{\mathrm{m}})^2 + \kappa^2/4)$ and $\Gamma_{\mathrm{AS}} = \bar{n}_{\mathrm{th}}\Gamma_{\mathrm{m}}(1 - 1/R)^{-1}$. In the sideband-resolved regime, $R \to \infty$ and the anti-Stokes rate becomes equal to the phonon flux into the mechanical resonator coming from the thermal bath. In the other extreme (i.e. $C_q \gg 1$) the two rates equalize and we have $\Gamma_{\mathrm{S}} \approx \Gamma_{\mathrm{AS}} \longrightarrow g_0^2\bar{n}_{\mathrm{cav}}\kappa/(4|\Delta|\Omega_{\mathrm{m}}) \propto C_q$, which shows that the scattering rates of two processes become equal and are dominated by quantum back-action.

9.3 DETECTION OF FILTERED MECHANICAL SIDEBANDS

Unfiltered optomechanical spectra can be easily and efficiently measured using direct detection, i.e. using a single photodiode placed directly at the output of the optomechanical cavity. This is due to the fact that the cavity transduces membrane motion into light intensity fluctuations when the optical drive is correctly detuned (Aspelmeyer, Kippenberg, and F. Marquardt 2014). As seen in Fig. 9.3a, the spectrum consists of the main high-Q mode surrounded by a phononic bandgap and dense regions of modes outside of the bandgap.

In order to confirm the performance of the filtering system, we apply it to the output of the OM cavity and detect the filtered light with a heterodyne measurement. The effect of filtering on the light spectrum is easily seen on Figs. 9.3b,c, where we tune the filter to be resonant with distinct parts of the spectrum. When the filter is tuned to the main mechanical mode [Fig. 9.3b], it efficiently isolates it from closely neighboring out-of-bandgap modes, which is a necessary condition for single-photon-based measurements. We can also select a part of the spectrum containing many out-of-bandgap modes, as in Fig. 9.3c, which clearly reveals the envelope of the filter system's response.

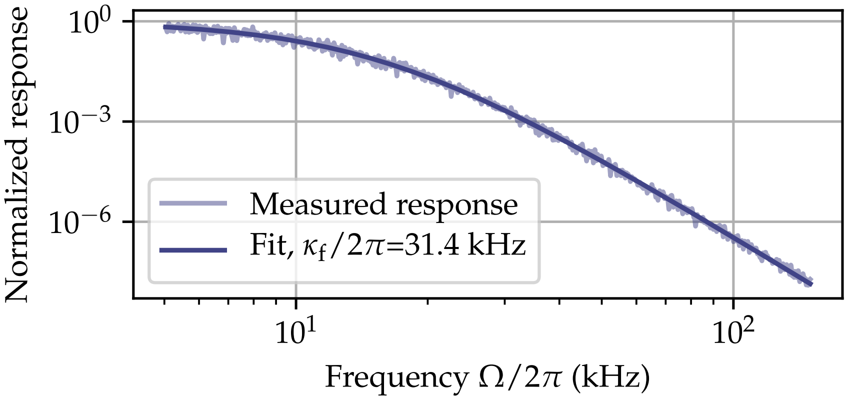

Figure 9.2: Rejection of the cascaded filtering system as a function of detuning, where the $L(\Omega)^4$ model (violet) closely follows the measured response (gray). For frequencies above 200 kHz the heterodyne signal becomes too weak to measure, but is expected to continue following the $L(\Omega)^4$ response.

In a different measurement, we direct the output of the filtering system to the SPCM and lock the center frequency at different detunings across the bandgap (Fig. 9.4). We observe greatly reduced photon scattering rates inside the bandgap, and large scattering when approaching low-Q out-of-bandgap modes that are strongly coupled to the thermal bath. As a consistency check, we estimate the expected count rates by convolving the $L(\Omega)^4$ response of the filters with a directly measured spectrum, where shot noise has been subtracted. The predicted and measured rates are in good agreement, with visible uncertainty only inside of the bandgap, where the scattering is low and shot noise level estimation errors can lead to increased uncertainties in the predicted count rate, as shown in Fig. 9.4. The residual discrepancy at 1.51 MHz is due to one of the higher-order defect modes that is very weakly damped by light and prone to mechanical excitation due to e.g. unstable liquid helium flow through the cryostat. This mode does not affect the measurements of the main mode, as shown on Fig. 9.3b, as it is being suppressed by the filter systems by 30 dB (see Fig. 9.2). Importantly, when the filters are tuned to the main mechanical frequency, the relative photon flux contribution of out-of-bandgap modes is expected to be less than 1% compared to the photon flux due to the main mechanical mode.

9.4 RAMAN-RATIO PHONON THERMOMETRY

An asymmetry between Stokes and anti-Stokes sidebands is a direct signature of near-zero occupation of the mechanical mode responsible for these sidebands. In particular, the ratio of powers in the two sidebands can be

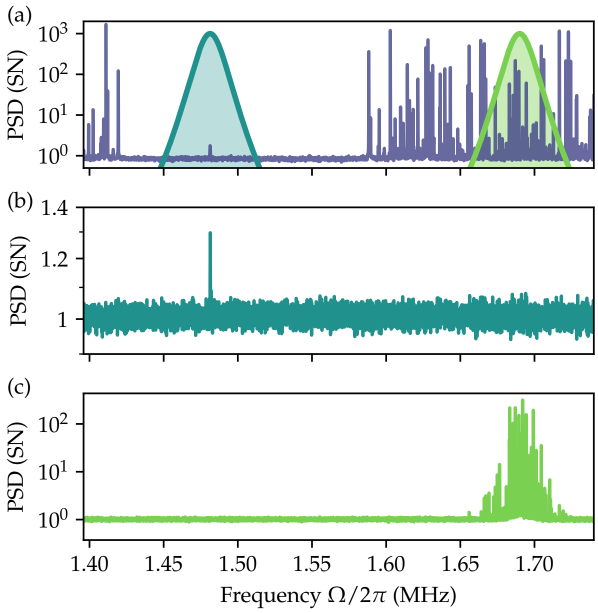

Figure 9.3: Filtering verified by heterodyne detection of filtered light. (a) Power spectral density (PSD) of light emitted directly from the cavity as registered by the direct-detection photodetector. PSD is calibrated in shot noise (SN) units. The spectrum shows the bandgap (between roughly 1.42 MHz and 1.59 MHz) provided by the phononic crystal structure and the high-Q mechanical defect mode at $\Omega_m = 2\pi \cdot 1.48$ MHz. The overlaid shaded curves are transmission functions $L(\Omega - \Delta_f)^4$ of the filtering system positioned at $\Delta_f = \Omega_m = 2\pi \cdot 1.48$ MHz and at $\Delta_f = 2\pi \cdot 1.69$ MHz. (b) and (c) show the PSD of filtered light, with the filter centered on the high-Q mechanical defect mode frequency, (b) and on the dense out-of-bandgap part of the spectrum (c). Note the different scale between (b) and (c).

directly used to infer the residual phonon occupation or, equivalently, the mode temperature. For mechanical resonators in the MHz frequency range, the most commonly employed method for measuring sideband powers has been heterodyne detection (Purdy et al. 2015; Peterson et al. 2016; Underwood et al. 2015; Chowdhury et al. 2019). In particular, it is fully sufficient to perform heterodyning of photons scattered from red-detuned cooling light. In this case, as cooling increases, the two sidebands move from being asymmetric due to the optomechanical cavity response, to being equally strong, indicating the balance of Stokes and anti-Stokes scattering in the quantum back-action dominated regime.

In the GHz mechanical frequency range, a more direct method of measuring sideband power based on photon counting (and thus effectively phonon counting)(1) has been demonstrated, where Stokes and anti-Stokes photons are filtered and subsequently detected by a single-photon detector. This method is not affected by the local oscillator noise (Weinstein et al. 2014), although it may suffer from dark counts of the photon counting detectors Cohen et al. (2015). The calibration-free nature of Raman-ratio thermometry, in both resonant and red-detuned cases, is one of its advantages as compared

(1) Cohen et al. 2015; Meenehan et al. 2015.

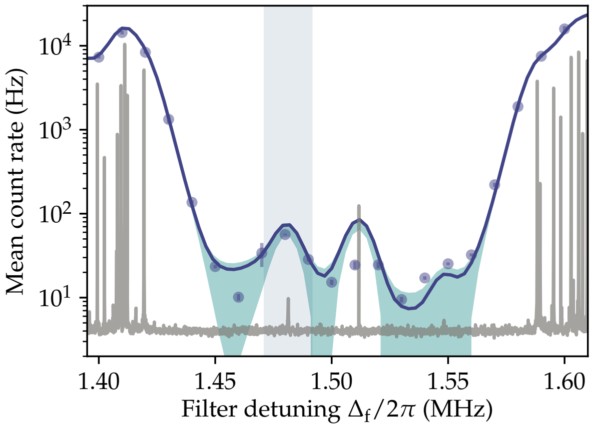

Figure 9.4: Photon counting of anti-Stokes sidebands, as a function of filter detuning, with count rates registered by the SPCM (blue dots), predicted count rates (solid blue line) with uncertainty (shaded teal area) and scaled directly-measured PSD (gray) for visual reference. The bandgap is effectively observed via photon counting. The shaded gray vertical strip shows the region surrounding the main mechanical mode.

to the more commonly employed technique based on spectral calibration using external phase modulation (Gorodetsky et al. 2010). In particular, one does not need to pre-calibrate the optomechanical single-photon coupling rate strength g_0. In the context of our work, phonon counting thermometry demonstrates the feasibility of efficient counting of single-phonon excitations, a fundamentally non-Gaussian operation.

Here we apply the phonon counting thermometry technique to our $\Omega_m = 2\pi \cdot 1.48$ MHz-frequency mechanical mode. A single beam detuned from the optomechanical cavity resonance by approximately optimal detuning $\Delta = 2\pi \cdot -1.85$ MHz, is used to both cool the membrane motion by dynamical back-action and simultaneously probe the system as it reaches the quantum back-action dominated regime.

We now proceed to demonstrate this behavior in our experimental setting. Figure 9.5a demonstrates the measured Stokes and anti-Stokes rates both growing with the intracavity photon number, quantified in terms of induced optical broadening Γ_{opt} measured using OMIT. For the lowest broadening of $\Gamma_{opt} = 2\pi \cdot 255$ Hz we observe sideband scattering rates of 20 Hz for Stokes and 100 Hz for anti-Stokes, corresponding the the ratio $R = 5$. As we increase the broadening to $\Gamma_{opt} = 2\pi \cdot 11$ kHz, the detected rates arrive at 215 Hz for Stokes and 260 Hz for anti-Stokes corresponding to a ratio of $R = 1.2$. Increased optical broadening also leads to reduced transmission through the filter setup, as compared with raw rates given by Eq. (9.3), which is due to the optically-broadened scattered light getting slightly "clipped" by the filtering system response. We model this loss by integrating a normalized Lorentzian spectrum with a width Γ_{opt} centered around Ω_m with

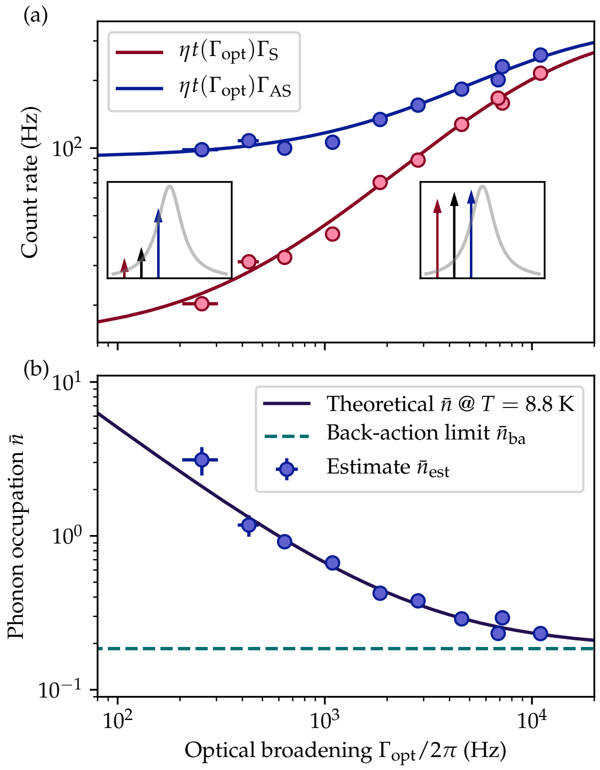

Figure 9.5: Ground-state cooling measured by photon counting. (a) Measured Stokes (red) and anti-Stokes (blue) scattering rates as a function of optical broadening Γ_{opt} of the mechanical mode and theoretical prediction with calibrated efficiency, as given in the legend. At lower driving powers, corresponding to smaller broadenings, the rates are set by the Lorentzian cavity response (left inset). At higher driving powers we observe that asymmetry is reduced due to the mechanical oscillator approaching the ground state (right inset), with scattering dominated by the quantum back-action. (b) Inferred thermal occupation $\bar{n}_{\mathrm{est}}$ of the mechanical mode, along with the theoretical prediction (for bulk thermalization temperature of $T = (8.8 \pm 0.5)\,\mathrm{K}$, which is the only free parameter in the fit) and the back-action limit $\bar{n}_{\mathrm{ba}}$ (dashed horizontal line). Error bars are inferred from statistical uncertainties from photon counting and fitting of other parameters used in Eq. (9.4).

$L(\Omega - \Omega_m)^4$:

$$\begin{aligned} t(\Gamma_{\mathrm{opt}}) &= \int L(\Omega - \Omega_m)^4 \frac{2}{\pi \Gamma_{\mathrm{opt}}} \frac{\Gamma_{\mathrm{opt}}^2/4}{(\Omega - \Omega_m)^2 + \Gamma_{\mathrm{opt}}^2/4} d\Omega \\ &= \frac{\kappa_f \left(5\Gamma_{\mathrm{opt}}^3 + 20\Gamma_{\mathrm{opt}}^2 \kappa_f + 29\Gamma_{\mathrm{opt}}\kappa_f^2 + 16\kappa_f^3\right)}{16(\Gamma_{\mathrm{opt}} + \kappa_f)^4}. \end{aligned} \tag{9.6}$$

This reduction is the same for Stokes and anti-Stokes sidebands, and thus it does not affect the ratio R. We find that the optical spring effect shifting the effective mechanical resonance frequency is below 3 kHz has a negligible effect on count rates for a fixed detuning of the filter system. In all cases we subtract the independently measured dark count rate of (15.5 ± 0.5) Hz. The overall detection efficiency of the entire system is estimated to be $\eta \approx 2.5\%$, consisting of optomechanical cavity outcoupling (75%), fiber transmission/coupling (60%), filtering system (30% for cavities and 50% for incoupling/outcoupling) and SPCM efficiency (35%). We note that the room for improvement of these efficiencies lies mostly in optics of the filtering system and SPCM efficiency.

Finally, we calculate the ratio R and estimate the mean phonon occupancy as given by Eq. (9.4) and plotted in Fig. 9.5b. The estimated phonon occupation $\bar{n}_{\mathrm{est}}$ is accurately described following a fit of Eq. (9.5). The mechanical occupation finally reaches a value of $\bar{n}_{\mathrm{est}} = 0.23 \pm 0.02$ at $\Gamma_{\mathrm{opt}} = 2\pi \cdot 11.0\,\mathrm{kHz}$ corresponding to $C_q \approx 22$, as estimated from calibrated parameters. The only free parameter of the theory is the the temperature of the phononic bath, determined to be $T = (8.8 \pm 0.5)\,\mathrm{K}$, which is consistent with previous works involving similar mechanical systems (Rossi et al. 2018). The minimum occupation achievable with sideband cooling, often referred to as the back-action limit, lies at $\bar{n}_{\mathrm{ba}} = (A_-/A_+ - 1)^{-1} \approx 0.185$ for our case. We thus observe a strong suppression of the classical sideband asymmetry due to the mechanical oscillator motion being primarily driven by the radiation-pressure shot noise.

9.5 PHONON CORRELATION INTERFEROMETRY

Lastly, we concentrate on statistical properties of light emitted from the high-Q mechanical mode. We set $\Gamma_{\mathrm{opt}} = 2\pi \cdot 2.1\,\mathrm{kHz}$ and park the filter at the anti-Stokes sideband. We collect a total of 18×10^3 counts at a count rate of 90 Hz, and look at coincidences between counts as a function of the delay time τ. Since we only use a single detector, we reject the events for which $|\tau| < 500\,\mathrm{ns}$, in order to avoid effects of dead time of the SPCM and afterpulsing. This time is still much shorter than any dynamics present in the system, and thus we can extrapolate our results on the coincidence rate to the zero-delay value. We analyze the coincidences in terms of the second-order Glauber correlation function

$$g^{(2)}(\tau) = \frac{\left\langle \hat{a}^\dagger(0)\hat{a}^\dagger(\tau) \cdot \hat{a}(0)\hat{a}(\tau)\right\rangle}{\left\langle \hat{a}^\dagger(0)\hat{a}(0)\right\rangle \cdot \left\langle \hat{a}^\dagger(\tau)\hat{a}(\tau)\right\rangle} \tag{9.7}$$

Light scattered by a single mechanical mode in thermal equilibrium has thermal statistics, as described by the following second-order correlation function:

$$g^{(2)}(\tau) = 1 + A\exp(-2|\tau|/\tau_C) = 1 + A\exp(-\Gamma_{\mathrm{opt}}|\tau|), \tag{9.8}$$

where $\tau_C = 2/\Gamma_{\mathrm{opt}}$ is the coherence time of light, with $g^{(2)}(0) = 2$ for $A = 1$. For a multimode thermal state, one would expect a multi-exponential or oscillatory decay. Our measurement, shown in Fig. 9.6, shows a single-exponential decay with a decay time matching the optically-broadened linewidth and exhibits $g^{(2)}(0) = 1.88 \pm 0.08$ (obtained from a fit of Eq. 9.8 with A and τ_C as free parameters), which is close to the theoretical value of 2, indicating the high purity and single-mode behavior of the measured thermal state of light. The optical coherence time of $\tau_C = (143 \pm 18)\,\mu\mathrm{s}$ (corresponding to an optical linewidth of $(2.2 \pm 0.3)\,\mathrm{kHz}$), closely matches the optical broadening of the mechanical oscillator, independently measured by OMIT to be $\Gamma_{\mathrm{opt}} = 2\pi \cdot 2.1\,\mathrm{kHz}$. This feature confirms our system's potential for producing non-Gaussian quantum states of light and of motional degrees of freedom. We attribute the residual discrepancy to the dark counts that exhibit Poissonian counting statistics.

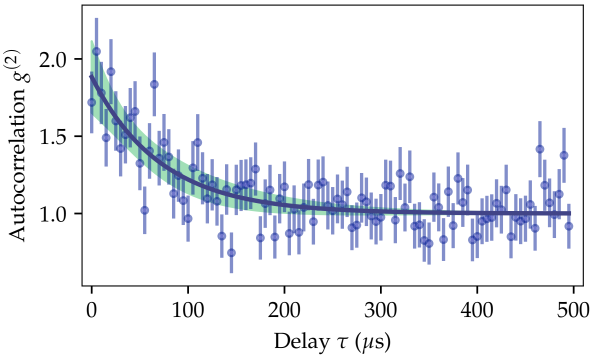

Figure 9.6: Second-order autocorrelation measurements of the spectrally-filtered anti-Stokes photons from the high-Q mechanical mode. We estimate $g^{(2)}(0) = 1.88 \pm 0.08$ and optical coherence time $\tau_C = (143 \pm 18)\,\mu\mathrm{s}$. Error bars in the plot are inferred from statistical uncertainties of Poissonian counts, while shading for the fitted curve corresponds to three s.d. confidence bounds.

CHAPTER 10

CAUCHY-SCHWARZ VIOLATION

> “If it ain’t broke, break it!
>
> GEORGE CARLIN[a]

(a) Possibly also Bert Lance, true origin unclear.

We describe preliminary results that strongly suggest the nonclassicality of our system

We have finally arrived to the most recent and non-classical result of our work: violation of Cauchy-Schwarz inequality. While preliminary, it promises a much better result in the future, once some experimental issues are solved. We will quickly reintroduce the main points of Cauchy-Schwarz inequality, and its importance to quantum experiments. Then, we will describe how it is calculated from the data that we acquire in order to showcase challenges. Finally, we will look into how we actually perform the experiment, including details on pulse generation, noise considerations (as usual), and outlook for future experiments.

It is important to note that in many of our results, we stand on the shoulders of giants who, in our group, have paved the experimental way to many of the techniques that we use here. Atomic spin ensembles behave rather similarly to harmonic oscillators, and the work of Dideriksen et al. (2021)(1), for example, is the inspiration for the statistical and experimental approaches that you will see shortly.

10.1 REMINDER OF CAUCHY-SCHWARZ PROPERTIES OF QUANTUM STATES

As we have already discussed in the section on theory, Cauchy-Schwarz inequality can show signatures of non-classical systems. This is due to the fact

(1) Karsten B. Dideriksen et al. (June 17, 2021). “Room-Temperature Single-Photon Source with near-Millisecond Built-in Memory”. In: *Nature Communications* 12.1 (1), p. 3699. ISSN: 2041-1723. DOI: 10 . 1038 / s41467 - 021 - 24033 - 8. URL: https://www.nature.com/articles/s41467-021-24033-8 (visited on 03/15/2023).

that some quantum states cannot be represented as probability distributions in phase space. Now, the Cauchy-Schwarz inequality *has* to be true for any probability distribution, otherwise "something is wrong". If we detect the "wrongness" in our measurements, we can conclude that our system is displaying non-classical properties.

More specifically, Cauchy-Schwarz inequality is valid for probability distributions and their moments. Classical states of light in this case yield the following inequality:

$$\left\| g_{12}^{(2)} \right\|^2 \leqslant g_1^{(2)} \cdot g_2^{(2)}, \tag{10.1}$$

where we have defined a shorthand notation of $g_{12}^{(2)} \equiv g^{(2)}(t_1, t_2)$, and $g_n^{(2)} \equiv g^{(2)}(t_n, t_n)$. It is convenient to define a *Cauchy-Schwarz parameter* that we will denote as R, such that

$$R \equiv \frac{\left\| g_{12}^{(2)} \right\|^2}{g_1^{(2)} \cdot g_2^{(2)}}. \tag{10.2}$$

Therefore, if $R > 1$, then the Cauchy-Schwarz inequality of Eq. (10.1) is not applicable, and we are dealing with non-classical statistics.

We shall present two examples where the Cauchy-Schwarz inequality holds:

1. Coherent states. For a coherent state, or even a pair of two coherent states, $g_1^{(2)} = 1 = g_2^{(2)}$, and $g_{12}^{(2)} = 1$ as well. As is evident, $R = 1$ in this case.
2. Thermal states. If we have two independent thermal states, for example two readouts of the membrane oscillator, separated by more than the decoherence time, then $g_{12}^{(2)} = 1$ (indicating cross-independence), but $g_1^{(2)} = 2 = g_2^{(2)}$, therefore $R = 1/4$, which is well within the inequality.

Note that the knowledge of $g_{12}^{(2)}$ per se is not enough to guarantee non-classicality, as there exist classical sources with strong bunching ($g_1^{(2)} \gg 1$). It is only the Cauchy-Schwarz parameter that can establish non-classicality in this case.

Experimentally, the Cauchy-Schwarz violation is a favorable way of proving nonclassicality, and that has to do with the way that we do our experiments: with photon counting. Our system has a somewhat low detection efficiency, and a low rate of generation of events. While the heralded preparation of single-phonon states with subsequent verification requires effectively acquiring three-time coincidences(2), Cauchy-Schwarz measurements only need two-time coincidences. This is crucial for systems with low efficiencies or event rates (or both, like ours). If we want to accumulate statistics in a reasonable timeframe, there is a big difference between the coincidence count rate of order $O(p \cdot \eta^3)$ (heralded) and $O(p \cdot \eta^2)$ (Cauchy-Schwarz), where p is the probability of excitation during the write pulse, and η is quantum efficiency of the system. This point requires a more careful consideration.

(2) Christophe Galland et al. (2014). "Heralded Single-Phonon Preparation, Storage, and Readout in Cavity Optomechanics". In: *Physical Review Letters* 112.14, pp. 1–6. ISSN: 10797114. DOI: 10.1103/PhysRevLett.112.143602. pmid: 24765960.

10.1.1 Error on estimation of correlations

We shall look at the uncertainty of our estimation of $g^{(2)}$. First, let's consider the two-mode correlation $g_{ab}(0)$ between, say, the read and write pulses (or rather the output produced by them):

$$g^{(2)}_{ab} = \frac{\langle \hat{a}^\dagger \hat{a} \hat{b}^\dagger \hat{b} \rangle}{\langle \hat{a}^\dagger \hat{a} \rangle \cdot \langle \hat{b}^\dagger \hat{b} \rangle} \tag{10.3}$$

Let's assume that the process that we are measuring has a known value of $g^{(2)}_{ab} \equiv \beta$, which means that the above can be rewritten as:

$$\langle \hat{n}_a \hat{n}_b \rangle = \langle \hat{n}_a \rangle \langle \hat{n}_b \rangle \cdot \beta \tag{10.4}$$

These quantities translate directly into photon counting by using numbers of photons in each "sequence", i.e. each experimental shot, and then averaging over all shots. It's helpful to introduce some simplifications applicable to our experimental case. First of all, estimating $\langle \hat{n} \rangle$ is a relatively precise process, as it does not rely on correlations, so we will assume that any instance of $\langle \hat{n} \rangle$ is a known constant for either mode. Second, the experimental shots are statistically independent of each other. Third, and most importantly, given our relatively low quantum efficiency, we can assume that the value of $n_a \cdot n_b$ (actual measured number) is Poissonian-distributed. From the properties of Poissonian distributions we know that, given a distribution with mean λ and m samples drawn from it, the variance (i.e. uncertainty squared) of the estimated mean $\tilde{\lambda}$ is:

$$\operatorname{Var} \tilde{\lambda} = \frac{1}{m} \cdot \lambda \tag{10.5}$$

Applying this to our previous definition, we obtain

$$\operatorname{Var} \langle \hat{n}_a \hat{n}_b \rangle = (\langle \hat{n}_a \rangle \langle \hat{n}_b \rangle)^2 \cdot \operatorname{Var} \beta = \frac{1}{m} \cdot \langle \hat{n}_a \rangle \langle \hat{n}_b \rangle \cdot \beta_0 \tag{10.6}$$

where we abused the notation a little bit and introduced β_0 as the a-priori known $g^{(2)}_{ab}$. In the end, we obtain the variance of the *estimate* of β:

$$\operatorname{Var} \beta = \frac{\beta_0}{m} \cdot \frac{1}{\langle \hat{n}_a \rangle \langle \hat{n}_b \rangle} \tag{10.7}$$

If we now remember the proportionality $\langle \hat{n} \rangle \propto p\eta$, where p is the probability of blue scattering, and η is the quantum efficiency, we can derive a proportionality:

$$\operatorname{Var} \beta \propto \frac{1}{m} \cdot \frac{1}{p^2 \eta^2} \tag{10.8}$$

With a similar treatment, the *autocorrelation* $g^{(2)}_{aa}(0) \equiv \gamma$ can be computed:

$$\operatorname{Var}\gamma = \frac{1}{m}\left(\gamma_0 \frac{1}{\langle\hat{n}_a\rangle^2} + \frac{1}{\langle\hat{n}_a\rangle^3}\right) \approx \frac{1}{m} \cdot \frac{1}{\langle\hat{n}_a\rangle^3}, \tag{10.9}$$

where the latter approximation is due to our low probabilities. Now, it's important to remember that we consider this in context of heralded preparation, i.e. $g^{(2)}_{aa|b}$. The probability of a "click" in the heralding pulse is itself $p\eta$, which essentially increases the amount of necessary experimental shots. On the other hand, since the readout pulse is almost 100 % efficient (before losses η), we can write that $\langle\hat{n}_a\rangle = \eta$. In the end, we get a proportionality as follows:

$$\operatorname{Var}\gamma_{\text{cond}} \propto \frac{1}{m} \cdot \frac{1}{p \cdot \eta^4} \tag{10.10}$$

All of the above shows the advantage of Cauchy-Schwarz statistics in terms of measurement time for a given level of variance required. While the Cauchy-Schwarz inequality does not prove that we have single-photon states, it does prove the nonclassicallity of a system, which is a good stepping stone and a proof of concept. Additionally, for more advanced experiments such as preparation of single-photon states in the context of optomechanics, the sequence for generating Cauchy-Schwarz violations is almost identically the same as the sequence of actions necessary for single-photon generation.

10.2 PULSE SEQUENCE

I will now describe the pulse sequence that we use when measuring Cauchy-Schwarz parameters. The main goals of the sequence are to ground-state cool the mechanical mode, excite it parametrically, and then read out the resulting state back into the light so that it can be counted with the photon counter. Additionally, we need to take care of the idle time between pulse sequences, as these sequences do not run at "full steam" due to reasons that we'll describe later. When talking about the particularities of the sequence and its individual parts, we'll provide a detailed explanation for the experimental limitations that lead to them.

10.2.1 Pre-cool (idle)

Let us begin, as many things go, by describing difficulties first, and then showing our way of going around them. Our new optomechanical assembly (that is, one involving small mirrors and large length) seems to have an odd problem that we denote as "strange heating", "extra heating", and "why is this happening". At the moment of writing, we are not entirely sure of what is the cause, but the symptoms are as follows:

- With large enough optical powers, we observe a slow temperature increase of the membrane. The occupation increases, as evidenced by a larger mechanical peak area and the frequency of the main mode shifts on a timescale of about 0.1 s.

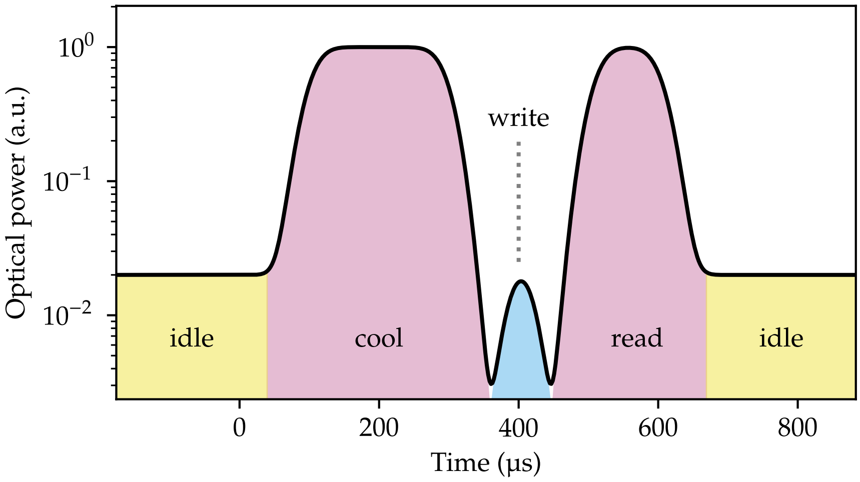

Figure 10.1: Idle-cool-write-read-idle sequence. Displayed on logarithmic scale to emphasize the non-zero idle power. The idle duration is typically much longer than the sequence to keep the average power low, as detailed in main text.

- The structure of cavity's resonances slightly changes, with neighboring FSRs shifting in frequency.

We have several hypotheses of what might be causing the above, but are yet to prove or disprove them:

- The small mirrors are very poorly thermally coupled to their cryogenic environment. They are "sandwiched" between two thin plates of PTFE, which is good for mechanical decoupling, but not that great for thermal conductivity. PTFE is a poor conductor as is at room temperature (0.27 W/(m K)), and only gets worse at low temperatures (0.046 W/(m K) at 4 K)(3). This can lead to mirrors being very susceptible to heating due to laser absorption. In turn, warm mirrors will have increased mirror noise, which can be optomechanically coupled to the membrane motion.
- The large beam diameter impinging on the membrane's center defect can be "clipped" by the edges of the defect. Preliminary results(4) suggest that the edges of the defect can lead to increased light absorption, especially when the beam is offset from the defect's center.

For now, this heating problem is not resolved, and we continue working on straightening it out. Nevertheless, we can make some experimental sacrifices in order to still operate the system satisfactorily. We noted the slow timescale of this heating phenomenon, and its dependence on slowly-averaged total optical power. Therefore, by operating the system in a low-duty-cycle fashion. "Duty cycle" in this context refers to the ratio between the time that is spent doing pulse sequences versus the total time. More specifically, this consists in the following two modifications:

(3) E. D. Marquardt, J. P. Le, and Ray Radebaugh (2002). "Cryogenic Material Properties Database". In: *Cryocoolers 11*. Ed. by R. G. Ross. Boston, MA: Springer US, pp. 681–687. ISBN: 978-0-306-47112-4. DOI: 10.1007/0-306-47112-4_84. URL: https://doi.org/10.1007/0-306-47112-4_84.

(4) Private communications with Mads Bjerregaard Kristensen

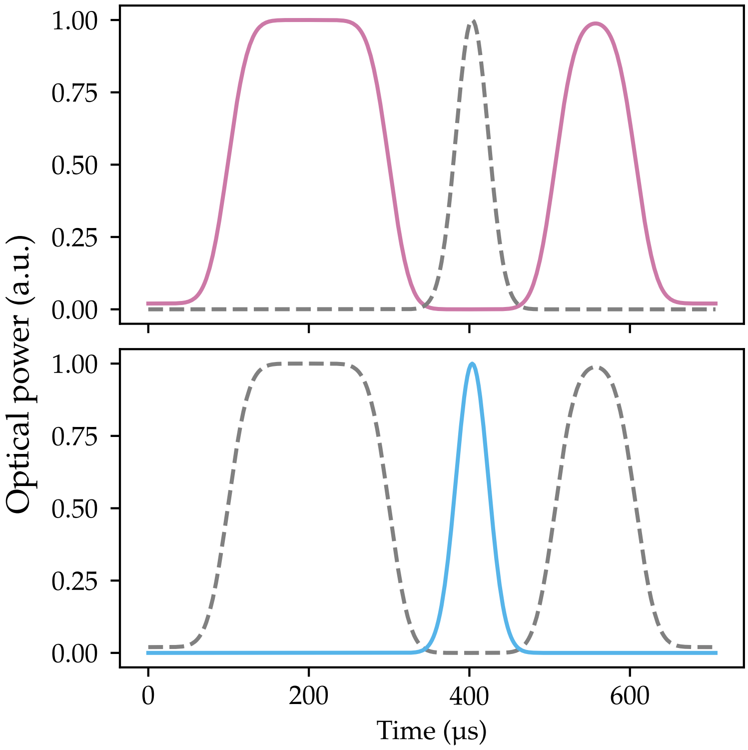

Figure 10.2: Red-detuned (top) and blue-detuned (bottom) pulses. Dotted lines are for comparison, as the blue power is typically much lower, as will be shown below.

1. Between individual sequences, which last on the order of 500 μs, have long idle periods with only cooling light turned down to about 2 % of maximum cooling power. This is done to reduce the average optical power. We do not reduce this power all the way to zero because we would like to keep the membrane in a relatively low occupation state,
2. Reduce both the length of each sequence, and the rate at which they are triggered. In practice, we had to drop the rate of triggering from the maximum of about 2 kHz to a mere 100 Hz or so.

The previous measures of course severely decrease the rate at which events are generated, but make the system operate without the extraneous heating getting in the way.

10.2.2 Smooth transitions

One important aspect of pulsing is transient control. As was shown in (Zwettler 2019)(5) , mechanical oscillators ring when the DC force on them changes abruptly. When optical power is applied to the optomechanical cavity, the radiation pressure on the mechanics has a certain DC component. If we were to turn this light on or off abruptly, the sudden change of radiation pressure would cause the mechanical modes to get coherently excited. As one can imagine, this is a bad thing, as it would translate to an effective increase in

(5) Timo Zwettler (Sept. 16, 2019). "Suppression of Heating Mechanisms for Deep Optomechanical Ground-State Cooling". M.Sc. thesis. Copenhagen, Denmark; München, Germany: Ludwig Maximilians Universität, München; University of Copenhagen.

phonon occupation(6). Now, it is possible to shape the transient in a way that cancels its own effects, but that requires precise knowledge of the system's response function. Such compensation is difficult to achieve in our system, as optical powers are not entirely constant, and the membrane has many modes of oscillation. Luckily for us, there is an easier way to achieve this: Gaussian pulse smoothing.

It is widely known(7) that Gaussian functions, when translated into the frequency domain, are the most "compact". A sufficiently broad Gaussian-shaped pulse will have a narrow spectral representation, which is what matters if we want to minimize its interaction with the mechanical modes, especially the main mode. That being said, pure Gaussian pulses are a bit inconvenient: the length of the pulse is rigidly tied to its "lead-in" and "lead-out" length. That is, the longer the pulse, the slower it ramps up and ramps down. Therefore, we cheat a little bit by creating what we call "pseudo-Gaussians". This shape, as shown in Fig. 10.3, consists of a rectangular pulse, but with the transitions replaced by left or right "halves" of a Gaussian of suitable transition time τ. τ has to be chosen strategically, as we will describe later.

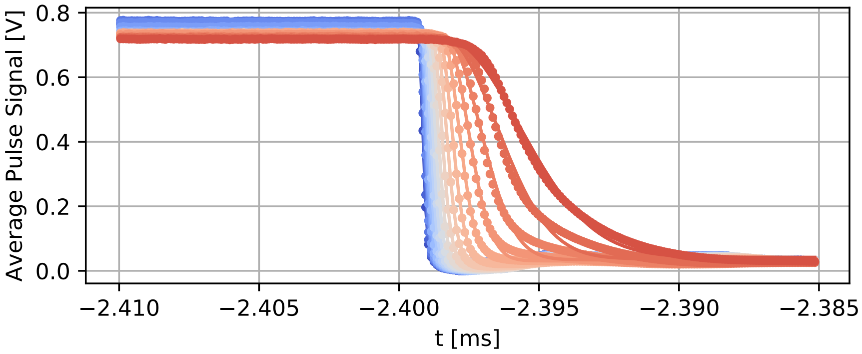

Figure 10.3: Optical power of smoothed pulses for different levels of Gaussian smoothing. Figure from (Zwettler 2019)

Such transitions still perform admirably, as shown in Fig. 10.4 and Fig. 10.5! In practice, we typically go with values of $\tau_a \approx 10 \cdot 1/\Omega_m \approx 10\,\mu\mathrm{s}$.

10.2.3 Cooling

The first "real" part of the sequence is the cooling pulse. Its purpose, as it may be evident, is to cool the main mode of the membrane to its minimum possible occupation. After a long enough idle period, as we described above, we increase the red-detuned optical power to its maximum. The length of this pulse has to be chosen such that the mechanical occupation drops down to its minimum possible value. Strictly speaking, this would require infinite time, as the phonon number only *tends* to this ultimate value. However, the dynamics of this cooldown are exponential, i.e. $n(t) = n_f + (n_0 - n_f) \cdot \exp(-t/\tau_m)$, with τ_m being the broadened decay time ($\tau_m = \Gamma_{\mathrm{opt}}^{-1}$). Under conditions of initial occupation being significanly larger than the final occupation, we simply take the pulse length that is enough

(6) Technically it's still a coherent oscillation, but controlling it in practice is rather tricky

(7) in our narrow field

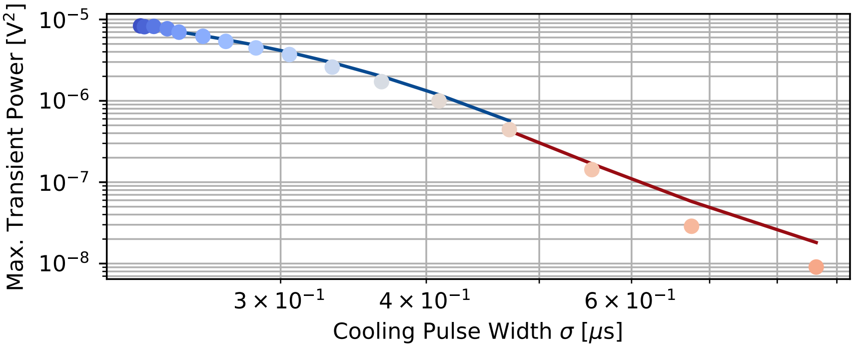

Figure 10.4: Experimentally measured effect of Gaussian smoothing on added power to the main mechanical mode. Figure from (Zwettler 2019)

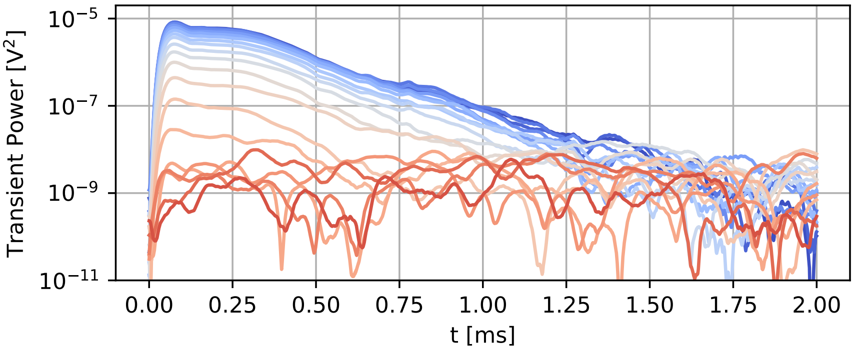

Figure 10.5: Time-dependent demodulated signal of the main mode for different smoothing parameters. Figure from (Zwettler 2019)

to reduce the occupation *almost* to the target value. For a concrete example, let us take some realistic numbers: $C_q = 10$, $\Gamma_{opt} = 2\pi \cdot 2\,\text{kHz}$, $n_f = 0.1$, $n_0 = 10$. n_0 in this case comes from the pre-cooling that we described above. The required pulse time is then simply $\tau_m \cdot \log(n_f/n_0) \approx 4.6\tau_m \approx 370\,\mu\text{s}$. In practice, we usually add a safety margin of $2\tau_m$ to make sure that the decay to final occupation has completed fully, and to compensate for uncertainty in estimating both the final and initial occupations.

10.2.4 Writing, or excitation

After cooling has been done, it is time to perform the *exciting* part of the sequence. First, cooling needs to be switched off, and we do it using the smooth transitions described above and shown in Fig. 10.3. There is a small caveat: since the transition is not instantanous, we have to wait for a certain amount of time until the red-detuned light had decayed enough. It is not necessary to wait too long here, and we are satisfied with a reduction to a level of, say, 5 %, which is equivalent to about $3\tau_a$. The next step is to turn on the excitation light, detuned to the blue side of the resonance. As we have discussed previously, this is what creates a spontaneous parametric down conversion process, which in turns creates photon-phonon pairs.

Same as with the cooling pulse, we need to choose a suitable duration and strength of this pulse. In this case, the area of the pulse determines the probability of excitation, which has to be "dialed-in" correctly. As you might remember, our system does not have a high quantum efficiency end-to-end. Therefore, we are not able to distinguish multiple excitations from single excitations, as the probability of "losing" one of the photons created in the process is very high. This is the main reason why we have to reach for the heralded probabilistic excitation scheme. The excitation probability that we typically choose ranges between 3 % and 10 %. As usual, there is a balance to be struck:

- For high excitation probabilities, the success rate is higher. Unfortunately, so is the chance of generating multiple photon-phonon pairs, which is undesirable in all but the highest-efficiency systems capable of distinguishing different numbers of photons.
- Low probabilities lead to purer single-phonon states in theory. However, we cannot go with an arbitrary low probability because of several reasons. One of them are the dark counts in our detection system. It is true that SNSPDS detectors have remarkably low intrinsic dark count rates, often below 0.1 Hz. The problem is "the everything else". Stray light finding its way in the free-space section, and even leaking into the fiber can easily overwhelm the intrinsic counts. Additional noise from the laser, both in phase and amplitude, can pass through the optomechanical system and filters, and also contribute to non-signal counts. Noise in mirrors or membrane can also overlap with the system's transmission band. Therefore, if the quantum signal is arbitrarily small, these spurious photons will overwhelm the signal and reduce the purity of statistics.

So far, we have achieved the balance between success rate and good statistics by performing several runs of the experiment at different levels of excitation power, and chose ones that provided us with the best statistics. correction. Therefore, this implies that we need to have a pause between the cooling and the excitation and likewise between excitation and reading because we need time for the previous pulse to fully decay and we need time for the subsequent polls to ramp up to full power.

10.2.5 Reading pulse

Finally, once we have excited the mechanics, it is time to read the prepared state and convert it into photons that can be detected. This last step is identical to the cooling pulse actually, as both optomechanical cooling and reading are the same process (beamsplitter interaction, as shown in Section 4.5). This time, however, we are interested in the output photon statistics. Just like before, the first thing is to smoothly turn off the writing pulse. After that is done, we ramp up the red-detuned light once again to full power. In this case, the length of the pulse is much less critical, as we will describe shortly. Additionally, the read-out process is not probabilistic: whatever state is in the mechanics will be read out at this point. In a way, the reading pulse is only needed for *confirmation* of non-classicality, not its generation. This is especially true for heralded single-phonon generation, where the nonclassicality can be confirmed via other methods, like continuous tomography. For Cauchy-Schwarz violation, however, this is our only method of observing the relevant statistics, so it's still crucial. Let us now describe the important aspects of choosing the correct pulse length:

- Read-out efficiency. We want to be sure that the state of the mechanics, whatever it is, is read out completely. The consideration is identical to the cooling pulse: the previous state has to be completely removed. And, just like in the case of cooling, we do it by determining the broadened decay time ($\tau_m = \Gamma_{opt}^{-1}$), and setting our required performance. More concretely, we often choose a read-out efficiency of 95 %. Then, the required pulse length is $\approx -\tau_m \cdot \log(1 - 0.95) \approx 3\tau_m$.

- Extra heating. As we have mentioned above, the "mystery heating" in our system prevents us from using arbitrarily long cooling powers, as this would start to increase the temperature of the membrane through uncertain mechanisms. Therefore, we have to limit ourselves to the "minimum viable pulse length" in order to avoid increasing the average optical power.

All in all, $3\tau_m$ is the usual reading pulse duration that we use. After it has concluded, the power is smoothly decreased back to the idle level of about 2 % and kept there until the next sequence is triggered.

10.3 Photon cross-correlations

It is time to describe the way to calculate the cross-correlations between write and read portions of the sequence. In this section, we will not go into the technicalities of photon detection, recording, and synchronization of time traces. Instead, we will focus on the specifics of data analysis relevant to Cauchy-Schwarz and future single-phonon generation. In broad terms, these steps are required:

1. Starting with a long trace of photon timestamps, extract the individual sequences ("shots") and align them on a shared timebase.

2. Averaging over all the sequences, obtain average count rates for diagnostics.

3. Count coincidences between different time windows. This step is the one that gives us Cauchy-Schwarz parameters, and is the most important.

We shall now describe these steps in detail, with pictures!

(8) In the middle of the night, of course

10.4 SEQUENCE EXTRACTION

An experimental run with photon tagging usually takes a long time, several hours not being unusual(8). The run contains hundrends of thousands, or even millions of repetitions of the sequence that we have described above. Let's call them "reps", a concept familiar to fit people. All those reps are independent from each other in the statistical sense, but have the same underlying pulse sequence. Therefore, the first step of data analysis is to "slice" them up so that they can be analyzed on an individual footing, followed by extraction of statistics. To see this process more visually, refer to Fig. 10.6.

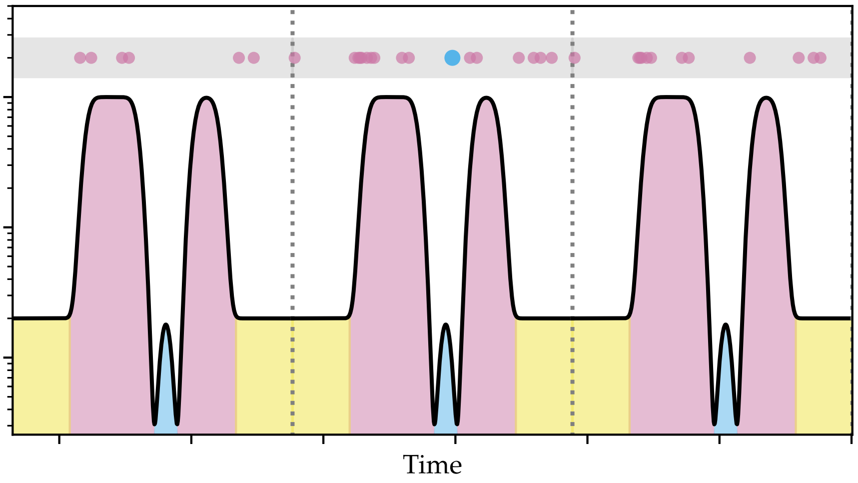

Figure 10.6: Illustration of several experimental repetitions with simulated photon counts shown as circles within the grey band. Red circles correspond to photons produced by the reading process, while the lonely blue circle is a photon produced by the low-probability write process. As we have mentioned in the main text, these photons have the same optical frequency, and are hence indistinguishable.

Our photon traces are synchronized in time with experimental events, such as trigger edges that start each sequence, shutter open-close events and filter lock-freeze events. These events are recorded in a timetrace format similar to that of the photons themselves, which we use to separate the different experimental events and, in a way, stack them together, as shown in Fig. 10.7. We call the resulting slices "windows". Typically, we perform additional filtering steps on those windows to get rid of those slices that occured during closed shutters, optomechanical cavity relocks, etc. With this done, we have our dataset.

10.5 AVERAGING COUNT RATES

With the windows separated and synchronized, we effectively obtain a list of lists, or a set of sets:

$$W = \{ w_i \}, \text{ with } w_i = \{ t_0^{(i)}, t_1^{(i)}, \dots \}, \tag{10.11}$$

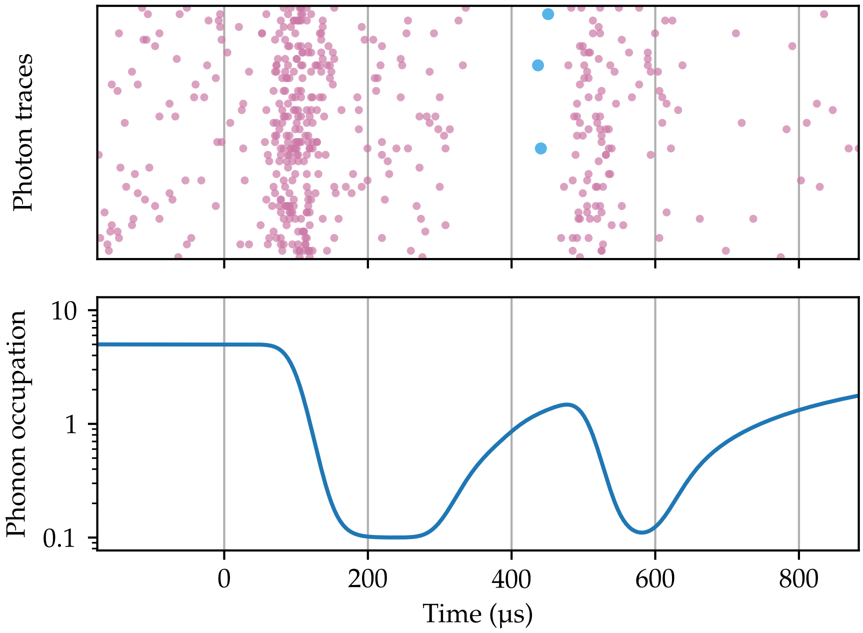

Figure 10.7: Stacked simulated photon traces (top plot), and the corresponding phonon occupation (bottom plot) during an experimental repetition.

with $t_n^{(i)}$ being the n-th photon arrival time in the i-th window. Generally, windows w_i will contain different number of photons. One thing we do before any analysis is converting absolute timestamps to timestamps relative to the beginning of each repetition, i.e. relative to the trigger edge. This places all windows on equal footing. Then, the photon rate can be defined. Note that working with timestamps is a bit different to the more usual(9) continuously-sampled data, as counting replaces most operations. Then, for any given window w, we can define(10) the photon rate as:

(9) at least to the author

(10) omitting window number for brevity

$$r_w(T_1, T_2) \equiv \frac{N\left\{ t_i \mid T_1 \leqslant t_i < T_2, \forall t_i \in w \right\}}{T_2 - T_1}, \tag{10.12}$$

with $T_1 < T_2$ and $N(s) \equiv$ number of elements in set s. Note that we need to specify the range over which we compute this average, in a trade-off between responsiveness and variance. This concept is easily extended to the whole set of windows:

$$r(T_1, T_2) \equiv \frac{N\left\{ t_i^{(k)} \mid T_1 \leqslant t_i^{(k)} < T_2, \forall t_i^{(k)} \in W \right\}}{T_2 - T_1}, \tag{10.13}$$

There is a bit of abuse of notation going on here, but the reader will hopefully "catch the drift". In practice, such counting is normally done by combining all the timestamps into one array, sorting it, and then performing fast counting. As expected, r has units of inverse time, i.e. photon intensity. Physically, it corresponds to the expectation value of the number operator for a travelling field:

$$\langle \hat{a}^\dagger(t)\hat{a}(t)\rangle \approx r(t-\delta t, t+\delta t), \tag{10.14}$$

with the approximation becoming exact when $\delta t \to 0$

10.6 COINCIDENCE COUNTING

We now turn our attention to a more sophisticated statistical measure: the two-time correlations between photons. This time, we will start with the physics first, and then translate them into photon counts. Let us first follow (Galland et al. 2014)(11) to get our definitions straight. First, we define non-normalized correlations between operators

$$G^{(1)}(t) = \left\langle \hat{a}^\dagger(t)\hat{a}(t)\right\rangle \tag{10.15}$$

$$G^{(2)}(t,t') = \left\langle \hat{a}^\dagger(t')\hat{a}^\dagger(t)\hat{a}(t)\hat{a}(t')\right\rangle, \tag{10.16}$$

where normal ordering has been already performed. For conditional single-phonon preparation experiments, we would also list the third-order correlation $G^{(3)}$, but for Cauchy-Schwarz inequality violation, it will be enough with the two correlations listed above, as it is not a conditional measurement. Notice that $G^{(1)}$ is identically the intensity (photon rate) as we outlined before. The quantity that we are interested in is the *normalized* second-order two-time correlation:

$$g^{(2)}(t,t') = \frac{G^{(2)}(t,t')}{G^{(1)}(t)G^{(1)}(t')} \tag{10.17}$$

We already know how to calculate $G^{(1)}$, but the second-order correlation is a bit more tricky. In plain words, the non-normalized second-order correlation computes the *rate of double coincidences*. One way of expressing it, assuming a continuous signal, is:(12)

$$G^{(2)}(t,t') = \langle I(t)I(t')\rangle \tag{10.18}$$

Just to be clear, this is the average of products of intensities at two different times. We then express it in terms of numbers of pairs of photons:

$$\begin{aligned} &G^{(2)}_w(0,t) && (10.19)\\ &\approx N\left\{ \{ t_i, t_j \} \in w,\ \text{where } t_i \in [0,\delta t) \text{ and } t_j \in [t, t+\delta t) \right\} / (\delta t)^2 \\ &\equiv r^{(2)}(0,t;\delta t)/(\delta t)^2 \end{aligned}$$

Note that this quantity has to be computed for each window separately, and *then* averaged. We have set the first time point to zero for simpler notation, but the result is equally valid for any pair of time points $t_1 < (t_2 - \delta t)$.

(11) Christophe Galland et al. (2014). "Heralded Single-Phonon Preparation, Storage, and Readout in Cavity Optomechanics". In: *Physical Review Letters* 112.14, pp. 1–6. ISSN: 10797114. DOI: 10.1103/PhysRevLett.112.143602. pmid: 24765960.

(12) Walls and G. Milburn 2008.

Note also that during counting, one should not count any given pair twice ((t_i, t_j) and (t_j, t_i) are the same pair). Finally, the factor of $(\delta t)^{-2}$ is there to convert the product of integers into a product of intensities (photon rates).

This allows us to finally formulate an expression that specifies how to use photon counting data to produce the normalized correlation function:

$$g^{(2)}(t, t'; \delta t) = \frac{r^{(2)}(t, t'; \delta t)}{r(t; \delta t) \cdot r(t'; \delta t)} \tag{10.20}$$

There exist efficient software packages capable of computing this kind of correlations(13),(14), as counting pairs directly is not efficient. We shall not go into the details of their implementation, but will remark that `photocorr-fock`, developed by Michal Parniak and colleagues, is our tool of choice.

(13) github.com/tritemio/pycorrelate

(14) github.com/Michuu/photonpacket

10.6.1 Experiment and results

With the theory laid out, we can now describe the experiment that we performed. Fundamentally it is not that different from the experiment of thermal phonon counting, with the addition of pulse sequences that perform the idle-cool-write-read-idle procedure, which we have described in detail above.

During this experiment, as it happens most often, we kept a close eye on the operation, as unforeseen disturbances can require manual intervention, even with our highly automated setup (7+ locks at the same time is Serious Business). Apart from that, our low photon rates require long acquisition times on the order of hours.

We shall not mention all the test runs that we performed while tuning and debugging the system. There were two major "physics" runs that culminated in the results that we will demonstrate.

10.6.1.1 Cauchy-Schwarz run

We set the pulsing sequence to a low probability of preparation of approximately 5 %. The idle level, as we mentioned, was set to a low enough value to prevent spurious heating. The photon rate analysis, coupled with a model of mechanical occupation, showed expected dynamic behaviour, as shown in Fig. 10.8.

After accumulating the equivalent of about 200 coincidences, data analysis revealed promising results. First of all, refer to Fig. 10.9, which shows correlation between photons at different times. While the figure itself does not lend itself to simple conclusions, further analysis of photons counts, which included taking proper sections to maximize the overlap with temporal modes that we discussed in Section 4, we obtained a Cauchy-Schwarz parameter of $R = 1.37 \pm 0.26$. While it's not exactly a 6-sigma confidence, it is still highly suggestive, and is definitely much higher than 0.25, which would be its value if there were no correlations at all, or 0.5 if there were only thermal correlations.

10.6.1.2 High-excitation run

Intrigued by the previous result, we decided to increase the probability of excitation, both to explore a different regime of operation, and hoping that

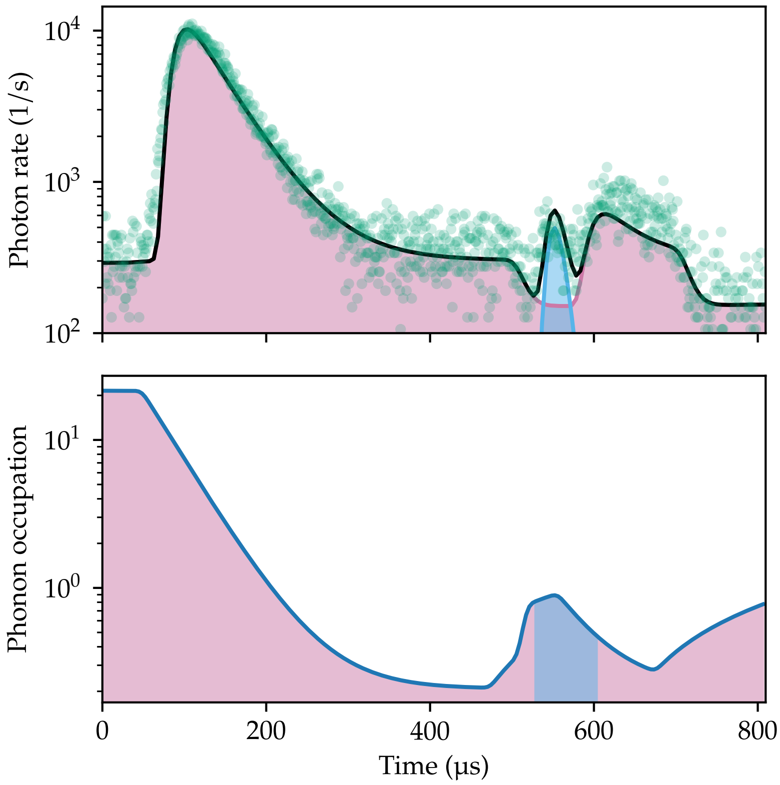

Figure 10.8: **Top:** averaged photon counts for a series of measurements aimed at Cauchy-Schwarz inequality violation. Black trace is obtained from a priori knowledge of the pulsing sequence, and scaled to the experimentally observed rates (green) in order to obtain estimates on occupation and coupling rates. Red and blue shaded areas corresponds to regions of the sequence where the reading or writing are the dominant process, respectively. The initial large spike correspond to the rapid readout of phonons that were accumulated during the long idle period preceding the sequence (see main text). **Bottom:** phonon occupation estimated from counting data and experimental parameters. Note that the occupation starts to increase slightly before the marked beginning of the writing pulse (blue shaded area). This is due to the fact that our model includes delays due to propagation through filter cavities, which contribute a combined time delay of $4 \cdot 2/\kappa \approx 42\,\mu s$, in addition to slight smoothing of the pulses.

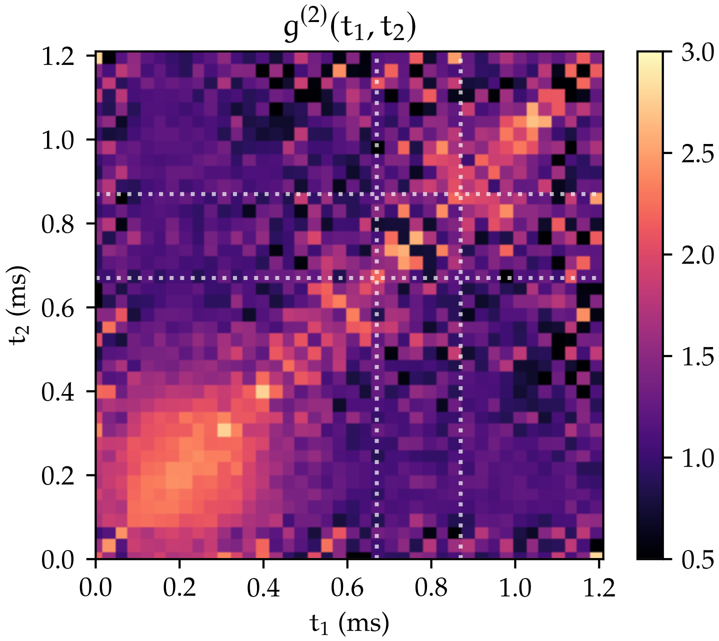

Figure 10.9: Correlation map for an experiment where the preparation probability was set to low values in order to see non-classical values of the Cauchy-Schwarz parameter. Off-diagonal regions, corresponding to write-read correlations, show an indication of non-trivial correlations. While the map itself does not look very indicative, numerical calculations confirmed a level of R compatible with non-classicality (see main text).

a stronger signal would pierce through the noise and give us further insights. Predictably, the rates of generation of photons increased, as shown in Fig. 10.10.

The increased number of events (about 6000 coincidences) allowed us to compute statistics with less uncertainty. Unfortunately, higher levels of excitation lead, by their nature, to decreased correlations in schemes such as ours. Nevertheless, Fig. 10.11 shows off-diagonal regions with increased $g^{(2)}$, which is a hint that we are on the right track, provided that several outstanding experimental issues can be addressed. With this dataset, we estimate a Cauchy-Schwarz parameter of 0.78 ± 0.06, which is still significantly higher than the "thermal-uncorrelated" 0.5.

10.6.2 Conclusion and outlook

Our system strongly suggests that non-classicality is achievable with photon counting with such a low-frequency system. There are still challenges to be solved, namely:

- Mystery heating, which limits both our cooling, repetition rate, and experimental stability.

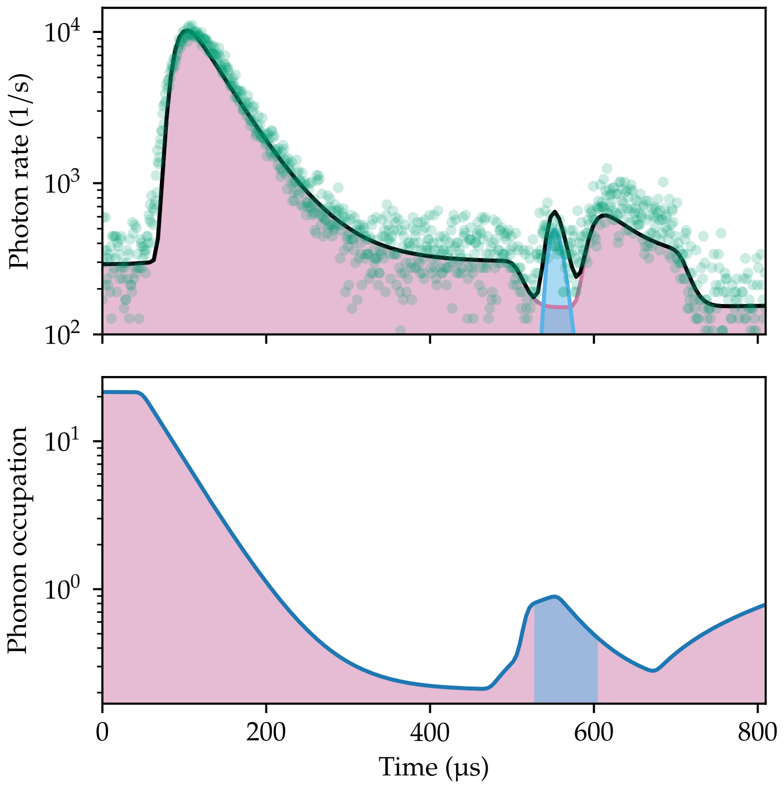

Figure 10.10: High-excitation photon rates and estimated phonon occupation. Structure of this figure is similar to that of Fig. 10.8

- Thermalization of the sample holder, which can possibly be solved by designing a new, more robust holder with less degrees of freedom.
- Mirror noise. If it proves to be a limiting factor, we shall look into better ways of thermalizing mirrors.
- Quantum efficiency. At the moment our system does not have one big bottleneck in terms of optical losses, but improving the transmission of filter cavities, and streamlining the fiber-based delivery of light to the single-photon counter should give us a relatively easy boost to performance.

However, the results are highly encouraging, and the author is looking forward to continuing work in that direction.

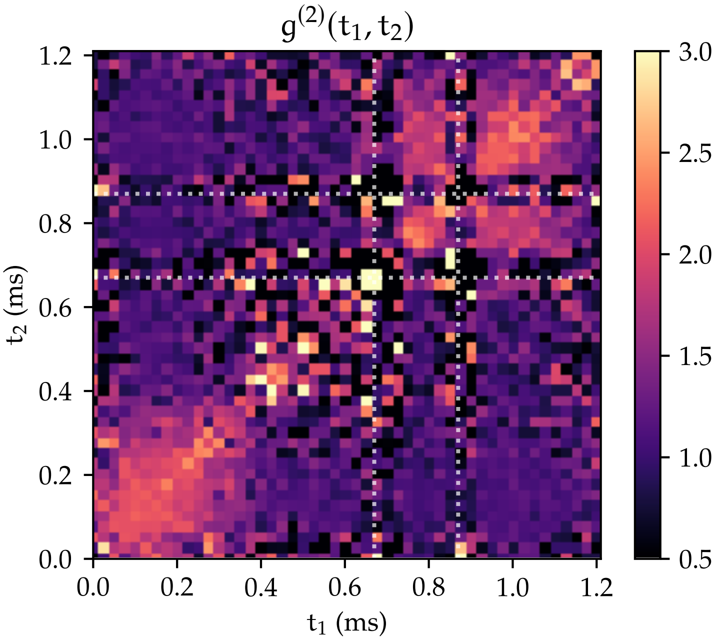

Figure 10.11: Correlation map for an experiment where we increased the preparation probability to high values. While the Cauchy-Schwarz value was degraded, the increased amount of statistics allowed us to more clearly see the off-diagonal regions in the map, where $g^{(2)} > 0.5$ (the value of 0.5 is chosen for aesthetics, as $g^{(2)}$ per se is insufficient for conclusions on non-classicality). These regions are indicated by the dotted lines. The rectangles to the top and right of the intersection are the regions of interest, which indicate non-trivial values of R.

Part V

CONCLUSION

CHAPTER 11

CONCLUSION AND THE FUTURE

> “Prediction is very difficult, especially if it’s about the future.
>
> NIELS BOHR(a)
>
> ---
>
> (a) and others, seems to be a very popular saying.

We summarize the main results of this work, the difficulties encountered, and the outlook for near future.

11.1 CONCLUSION

The work done, which culminated in this thesis, was a long and interesting journey. We have solved so many experimental challenges, big and small, that at this point everything looks like a nail waiting to be hit with our experimental sledgehammer. First, I will list the principal scientific results of this work, in a somewhat chronological order:

1. Filter cavity system, our pièce de résistance. Through several design iterations, tireless work by KU’s mechanical workshop, countless hours of programming, soldering, noise-hunting, and debugging, we made an optical filter with a bandwidth of 30 kHz, twice as narrow as the hearing range of a possum, and with an þ8-order rolloff.

2. We converted mechanical quanta into photons, and studied their thermal statistics, confirming the theoretical expectations, down to the level of sub-phonon occupations.

3. We established preliminary results on the non-classicality of specially prepared mechanical states, showing that our system displays(1) quantum memory capabilities.

(1) to a good degree of certainty

The author and his teammates went through such an experimental fire baptism in the process of establishing the above results, that we became thick-skinned, hard-to-kill jacks-of-all-trades. To substantiate the latter, let me show a non-exhaustive list of technical challenges that we had to overcome, and skills we had to learn:

- Generation of low-phase-noise RF drives.
- Multi-GHz RF design.
- Suspending half of our experiment on springs.
- Gold-plating of copper(2).
- Acousting modes of the air inside an optical cavity.
- 3D printing, including building a 3D printer.
- Resuscitating a GPS-disciplined oven-controlled crystal oscillator.
- Remote experimental work during COVID lockdowns.
- Reverse-engineering a proprietary USB-Serial protocol for a power supply.
- Programming of Xilinx Zynq, including both the programmable logic and processing system.
- Design of low-noise piezo amplifiers, based on Jürgen Appel's design.
- Putting things on top of other things.
- And many more!

(2) with real aurocyanate!

What I want to say is that under the hood of any experimental project, there is way more than meets the eye.

11.2 THE FUTURE

We have already covered future prospects in the relevant sections, so here I will simply list the most important takeaways, in order of decreasing priority. First, the problems to solve:

1. Mystery heating and short-time power-induced drift of the optomechanical cavity.
2. Mode hybridization in OM cavity (possibly related to, or causing the previous point).
3. Continue noise hunting to improve SNR of single-photon signals.
4. Improvement of single-photon detection efficiency, including filter system efficiency.
5. Thermaliztion of OM cavity, internal (mirrors) and external (coupling to cryostat). Possibly an improved design of OM sample holder.
6. Further automation of the experiment.

11.3 AFTERWORD

I am very thankful to everybody in QUANTOP and the "Greater QUANTOP" (HyQ, including Schliesser lab (SLAB)) for being such a friendly, understanding, and wise crowd. And thank you, dear reader! Galinskiy out.

List of Figures

BIBLIOGRAPHY

Ashkin, A. (Jan. 26, 1970). “Acceleration and Trapping of Particles by Radiation Pressure”. In: *Physical Review Letters* 24.4, pp. 156–159. DOI: 10.1103/PhysRevLett.24.156. URL: https://link.aps.org/doi/10.1103/PhysRevLett.24.156 (visited on 03/07/2023) (cit. on p. 4).

Aspelmeyer, Markus et al. (Dec. 2014). “Cavity Optomechanics”. In: *Reviews of Modern Physics* 86.4, pp. 1391–1452. ISSN: 0034-6861. DOI: 10.1103/RevModPhys.86.1391. URL: https://link.aps.org/doi/10.1103/RevModPhys.86.1391 (cit. on pp. 5, 23, 25–27, 32, 34, 88, 89).

Barwicz, Tymon et al. (Apr. 5, 2004). “Microring-Resonator-Based Add-Drop Filters in SiN: Fabrication and Analysis”. In: *Optics Express* 12.7, pp. 1437–1442. ISSN: 1094-4087. DOI: 10.1364/OPEX.12.001437. URL: https://opg.optica.org/oe/abstract.cfm?uri=oe-12-7-1437 (visited on 02/26/2023) (cit. on p. 68).

Bohr, N. (July 1, 1913). “I. On the Constitution of Atoms and Molecules”. In: *The London, Edinburgh, and Dublin Philosophical Magazine and Journal of Science* 26.151, pp. 1–25. ISSN: 1941-5982. DOI: 10.1080/14786441308634955. URL: https://doi.org/10.1080/14786441308634955 (visited on 03/07/2023) (cit. on p. 3).

Bowen, Warwick P. and Gerard J. Milburn (Dec. 2, 2015). *Quantum Optomechanics*. Boca Raton: CRC Press. 376 pp. ISBN: 978-0-429-15931-2. DOI: 10.1201/b19379. URL: https://doi.org/10.1201/b19379 (cit. on pp. 17, 18, 23, 25, 26, 28, 32).

Braginsky, V. B. and A. B. Manukin (1967). “Ponderomotive Effects of Electromagnetic Radiation”. In: *Soviet Physics JETP* (cit. on p. 5).

Braginsky, Vladimir B. et al. (1980). “Quantum Nondemolition Measurements”. In: *Science (New York, N.Y.)* 209.4456, pp. 547–557. DOI: 10.1126/science.209.4456.547 (cit. on p. 5).

Cassiday, Grant R. and George L. Fowles (2005). *Analytical Mechanics*. 6th ed. Thomson Brooks/Cole. ISBN: 978-0-534-49492-6 (cit. on p. 19).

Caves, Carlton M. (1981). “Quantum-Mechanical Noise in an Interferometer”. In: *Physical Review D: Particles and Fields* 23.8, pp. 1693–1708. DOI: 10.1103/PhysRevD.23.1693 (cit. on p. 5).

Chowdhury, A et al. (Mar. 2019). “Calibrated Quantum Thermometry in Cavity Optomechanics”. In: *Quantum Science and Technology* 4.2, p. 024007. DOI: 10.1088/2058-9565/ab05f1. URL: https://doi.org/10.1088%2F2058-9565%2Fab05f1 (cit. on p. 91).

Cohen, Justin D. et al. (Apr. 2015). “Phonon Counting and Intensity Interferometry of a Nanomechanical Resonator”. In: *Nature* 520.7548, pp. 522–525.

ISSN: 0028-0836. DOI: 10.1038/nature14349. URL: http://www.nature.com/articles/nature14349 (cit. on p. 91).

De Broglie, Louis (Oct. 1923). "Waves and Quanta". In: *Nature* 112.2815 (2815), pp. 540–540. ISSN: 1476-4687. DOI: 10.1038/112540a0. URL: https://www.nature.com/articles/112540a0 (visited on 03/07/2023) (cit. on p. 3).

Dideriksen, Karsten B. et al. (June 17, 2021). "Room-Temperature Single-Photon Source with near-Millisecond Built-in Memory". In: *Nature Communications* 12.1 (1), p. 3699. ISSN: 2041-1723. DOI: 10.1038/s41467-021-24033-8. URL: https://www.nature.com/articles/s41467-021-24033-8 (visited on 03/15/2023) (cit. on p. 97).

Duan, Lingze (Aug. 9, 2012). "General Treatment of the Thermal Noises in Optical Fibers". In: *Physical Review A* 86.2, p. 023817. DOI: 10.1103/PhysRevA.86.023817. URL: https://link.aps.org/doi/10.1103/PhysRevA.86.023817 (visited on 02/01/2023) (cit. on pp. 63, 64).

Duthil, P (2014). "Material Properties at Low Temperature". DOI: 10.5170/CERN-2014-005.77. arXiv: 1501.07100. URL: https://cds.cern.ch/record/1973682 (cit. on p. 40).

Egan, William (Apr. 2, 2003). *Practical RF System Design*. John Wiley & Sons, Inc. ISBN: 978-0-471-65409-4. URL: https://doi.org/10.1002/0471654094 (cit. on p. 11).

Foster, Scott et al. (May 2007). "Fundamental Thermal Noise in Distributed Feedback Fiber Lasers". In: *IEEE Journal of Quantum Electronics* 43.5, pp. 378–384. ISSN: 1558-1713. DOI: 10.1109/JQE.2007.894744 (cit. on pp. 63, 64).

Galinskiy, I. et al. (June 2020a). "Phonon Counting Thermometry of an Ultracoherent Membrane Resonator near Its Motional Ground State". In: *Optica* 7.6, pp. 718–725. DOI: 10.1364/OPTICA.390939. URL: http://www.osapublishing.org/optica/abstract.cfm?URI=optica-7-6-718 (cit. on pp. ix, 67, 84–88).

— (June 20, 2020b). "Phonon Counting Thermometry of an Ultracoherent Membrane Resonator near Its Motional Ground State". In: *Optica* 7.6, pp. 718–725. ISSN: 2334-2536. DOI: 10.1364/OPTICA.390939. URL: https://opg.optica.org/optica/abstract.cfm?uri=optica-7-6-718 (visited on 02/01/2023) (cit. on pp. 75, 80).

Galinskiy, Ivan, Georg Enzian, et al. (5/Sep/2021). "Counting MHz Phonons: Towards Generaton of Non-Gaussian Quantum States of Moton". In: Quantum Optics X. Torun, Poland (cit. on p. ix).

Galinskiy, Ivan, Yeghishe Tsaturyan, et al. (2/Dec/2018). "Towards Heralded Single-Phonon State Generation of an Ultracoherent Nanomechanical Resonator". In: Advances in Open Systems and Fundamental Tests of Quantum Mechanics. Bad Honnef, Germany (cit. on p. ix).

Galinskiy, Ivan et al. (2014). "Counterpropagating Sagnac Optical Tweezers as an Efficient Method for 3D Trapping in Air". In: *Latin America Optics and Photonics Conference*, LTu4A.31. DOI: 10.1364/LAOP.2014.LTu4A.31. URL: https://www.osapublishing.org/abstract.cfm?uri=LAOP-2014-LTu4A.31 (cit. on p. 4).

Galland, Christophe et al. (2014). "Heralded Single-Phonon Preparation, Storage, and Readout in Cavity Optomechanics". In: *Physical Review Let-*

ters 112.14, pp. 1–6. ISSN: 10797114. DOI: 10.1103/PhysRevLett.112.143602. pmid: 24765960 (cit. on pp. 29–31, 56, 98, 109).

Gere, James M. and Barry J. Goodno (Jan. 1, 2012). *Mechanics of Materials*. 8th edition. Stamford, CT: Cengage Learning. 1056 pp. ISBN: 978-1-111-57773-5 (cit. on p. 79).

Gil-Santos, Eduardo et al. (June 2020). "Optomechanical Detection of Vibration Modes of a Single Bacterium". In: *Nature Nanotechnology* 15.6 (6), pp. 469–474. ISSN: 1748-3395. DOI: 10.1038/s41565-020-0672-y. URL: https://www.nature.com/articles/s41565-020-0672-y (visited on 03/07/2023) (cit. on p. 5).

Goldstein, Herbert et al. (June 15, 2001). *Classical Mechanics*. 3rd edition. San Francisco Munich: Pearson. 664 pp. ISBN: 978-0-201-65702-9 (cit. on pp. 19, 20).

Gorodetsky, M. L. et al. (Oct. 2010). "Determination of the Vacuum Optomechanical Coupling Rate Using Frequency Noise Calibration". In: *Optics Express* 18.22, pp. 23236–23246. DOI: 10.1364/OE.18.023236. URL: http://www.opticsexpress.org/abstract.cfm?URI=oe-18-22-23236 (cit. on pp. 35, 46, 92).

Heisenberg, W. (Dec. 1, 1925). "Über quantentheoretische Umdeutung kinematischer und mechanischer Beziehungen." In: *Zeitschrift für Physik* 33.1, pp. 879–893. ISSN: 0044-3328. DOI: 10.1007/BF01328377. URL: https://doi.org/10.1007/BF01328377 (visited on 03/07/2023) (cit. on p. 3).

Hofer, Sebastian G. et al. (2011). "Quantum Entanglement and Teleportation in Pulsed Cavity Optomechanics". In: *Physical Review A - Atomic, Molecular, and Optical Physics* 84.5, pp. 1–10. ISSN: 10502947. DOI: 10.1103/PhysRevA.84.052327. arXiv: 1108.2586 (cit. on p. 31).

Ismail, Nur et al. (July 25, 2016). "Fabry-Pérot Resonator: Spectral Line Shapes, Generic and Related Airy Distributions, Linewidths, Finesses, and Performance at Low or Frequency-Dependent Reflectivity". In: *Optics Express* 24.15, pp. 16366–16389. ISSN: 1094-4087. DOI: 10.1364/OE.24.016366. URL: https://opg.optica.org/oe/abstract.cfm?uri=oe-24-15-16366 (visited on 02/13/2023) (cit. on pp. 10, 13).

Jayich, A M et al. (Sept. 2008). "Dispersive Optomechanics: A Membrane inside a Cavity". In: *New Journal of Physics* 10.9, p. 095008. DOI: 2008100103130400. URL: https://dx.doi.org/10.1088/1367-2630/10/9/095008 (cit. on p. 13).

Jiang, Xiaoshun et al. (Nov. 9, 2009). "High-Q Double-Disk Microcavities for Cavity Optomechanics". In: *Optics Express* 17.23, pp. 20911–20919. ISSN: 1094-4087. DOI: 10.1364/OE.17.020911. URL: https://opg.optica.org/oe/abstract.cfm?uri=oe-17-23-20911 (visited on 03/07/2023) (cit. on p. 5).

Keplero, Iohanne (1619). *De Cometis Libelli Tres*. Typis Andreae Apergeri, p. 168 (cit. on p. 4).

Landau, L.D. and E.M. Lifshitz (1976). "Chapter V - Small Oscillations". In: *Mechanics (Third Edition)*. Ed. by L.D. Landau and E.M. Lifshitz. Third Edition. Oxford: Butterworth-Heinemann, pp. 58–95. ISBN: 978-0-7506-2896-9. DOI: 10.1016/B978-0-08-050347-9.50010-1. URL: https://www.sciencedirect.com/science/article/pii/B9780080503479500101 (cit. on p. 19).

Lebedew, Peter (1901). “Untersuchungen Über Die Druckkräfte Des Lichtes”. In: *Annalen der Physik* 311.11, pp. 433–458. DOI: 10.1002/andp.19013111102 (cit. on pp. 2, 4).

Li, Xiufei et al. (Jan. 2020). “Impact Analysis of Cavity Length on Transfer Cavity Frequency Locking System for Atomic Inertial Measurement Device”. In: *AIP Advances* 10.1, p. 015340. DOI: 10.1063/1.5125604. URL: https://aip.scitation.org/doi/10.1063/1.5125604 (visited on 02/25/2023) (cit. on p. 84).

Liu, Chien et al. (Jan. 2001). “Observation of Coherent Optical Information Storage in an Atomic Medium Using Halted Light Pulses”. In: *Nature* 409.6819 (6819), pp. 490–493. ISSN: 1476-4687. DOI: 10.1038/35054017. URL: https://www.nature.com/articles/35054017 (visited on 03/13/2023) (cit. on p. 49).

Maiman, T. H. (Aug. 1960). “Stimulated Optical Radiation in Ruby”. In: *Nature* 187.4736 (4736), pp. 493–494. ISSN: 1476-4687. DOI: 10.1038/187493a0. URL: https://www.nature.com/articles/187493a0 (visited on 03/07/2023) (cit. on p. 4).

Mandel, Leonard and Emil Wolf (1995). *Optical Coherence and Quantum Optics*. Cambridge: Cambridge University Press. DOI: 10.1017/CBO9781139644105 (cit. on pp. 16, 17).

Marquardt, E. D. et al. (2002). “Cryogenic Material Properties Database”. In: *Cryocoolers 11*. Ed. by R. G. Ross. Boston, MA: Springer US, pp. 681–687. ISBN: 978-0-306-47112-4. DOI: 10.1007/0-306-47112-4_84. URL: https://doi.org/10.1007/0-306-47112-4_84 (cit. on p. 101).

Marquardt, Florian et al. (Aug. 2007). “Quantum Theory of Cavity-Assisted Sideband Cooling of Mechanical Motion”. In: *Physical Review Letters* 99.9, p. 093902. DOI: 10.1103/PhysRevLett.99.093902. URL: https://link.aps.org/doi/10.1103/PhysRevLett.99.093902 (cit. on p. 88).

Mathiassen, Jonas (3/Dec/2019). “Characterising and Modelling Thermal Substrate Noise for a Membrane in the Middle Optomechanical Cavity”. MSc. Niels Bohr Institute, Faculty of Science, University of Copenhagen (cit. on p. 47).

Maxwell, James Clerk (1873). *A Treatise on Electricity and Magnetism*. Vol. 1. Clarendon press (cit. on p. 4).

McCuller, L. et al. (Apr. 28, 2020). “Frequency-Dependent Squeezing for Advanced LIGO”. In: *Physical Review Letters* 124.17, p. 171102. DOI: 10.1103/PhysRevLett.124.171102. URL: https://link.aps.org/doi/10.1103/PhysRevLett.124.171102 (visited on 02/26/2023) (cit. on p. 68).

Meenehan, Seán M et al. (2015). “Pulsed Excitation Dynamics of an Optomechanical Crystal Resonator near Its Quantum Ground State of Motion”. In: *Physical Review X* 5.4, p. 041002. ISSN: 21603308. DOI: 10.1103/PhysRevX.5.041002. arXiv: 1503.05135. URL: https://journals.aps.org/prx/pdf/10.1103/PhysRevX.5.041002 (cit. on p. 91).

Møller, Christoffer B. et al. (July 2017). “Quantum Back-Action-Evading Measurement of Motion in a Negative Mass Reference Frame”. In: *Nature* 547.7662, pp. 191–195. ISSN: 0028-0836. DOI: 10.1038/nature22980. URL: http://www.nature.com/doifinder/10.1038/nature22980 (cit. on p. 44).

Nichols, E. F. and G. F. Hull (1903). “The Pressure Due to Radiation”. In: *Proceedings of the American Academy of Arts and Sciences* 38.20, pp. 559–599. ISSN: 0199-9818. DOI: 10.2307/20021808. JSTOR: 20021808. URL:

https://www.jstor.org/stable/20021808 (visited on 03/07/2023) (cit. on p. 4).

Nielsen, William Hvidtfelt Padkær (2016). “Quantum Cavity Optomechanics with Phononic Bandgap Shielded Silicon Nitride Membranes”. University of Copenhagen. 160 pp. (cit. on pp. 15, 49, 89).

NIR Free-Space Isolators (690 - 1080 Nm) (2023). URL: https://www.thorlabs.com (visited on 02/24/2023) (cit. on p. 81).

Østfeldt, Christoffer (2022). “Quantum Optomechanics for Hybrid Spin-Membrane Entanglement”. Niels Bohr Institute, Faculty of Science, University of Copenhagen (cit. on pp. 15, 40, 49, 51).

Parniak, Michał et al. (Mar. 1, 2021). “High-Frequency Broadband Laser Phase Noise Cancellation Using a Delay Line”. In: *Optics Express* 29.5, pp. 6935–6946. ISSN: 1094-4087. DOI: 10.1364/OE.415942. URL: https://opg.optica.org/oe/abstract.cfm?uri=oe-29-5-6935 (visited on 02/01/2023) (cit. on pp. ix, 55, 61–63, 65).

Peterson, R. W. et al. (Feb. 2016). “Laser Cooling of a Micromechanical Membrane to the Quantum Backaction Limit”. In: *Physical Review Letters* 116.6, p. 063601. ISSN: 0031-9007. DOI: 10.1103/PhysRevLett.116.063601. URL: https://link.aps.org/doi/10.1103/PhysRevLett.116.063601 (cit. on pp. 88, 91).

Planck, Max (1900). “Entropie Und Temperatur Strahlender Wärme”. In: *Annalen der Physik* 306.4, pp. 719–737. ISSN: 1521-3889. DOI: 10.1002/andp.19003060410. URL: https://onlinelibrary.wiley.com/doi/abs/10.1002/andp.19003060410 (visited on 03/07/2023) (cit. on p. 3).

Purdy, T P et al. (2015). “Optomechanical Raman-Ratio Thermometry”. In: *Physical Review A: Atomic, Molecular, and Optical Physics* 92.3, p. 31802. ISSN: 10941622. DOI: 10.1103/PhysRevA.92.031802. URL: https://journals.aps.org/pra/pdf/10.1103/PhysRevA.92.031802 (cit. on p. 91).

Riedinger, Ralf, Sungkun Hong, et al. (2016). “Non-Classical Correlations between Single Photons and Phonons from a Mechanical Oscillator”. In: *Nature* 530.7590, pp. 313–316. ISSN: 0028-0836. DOI: 10.1038/nature16536. pmid: 26779950. URL: http://www.nature.com/doifinder/10.1038/nature16536 (cit. on p. 5).

Riedinger, Ralf, Andreas Wallucks, et al. (Apr. 2018). “Remote Quantum Entanglement between Two Micromechanical Oscillators”. In: *Nature* 556.7702 (7702), pp. 473–477. ISSN: 1476-4687. DOI: 10.1038/s41586-018-0036-z. URL: https://www.nature.com/articles/s41586-018-0036-z (visited on 03/15/2023) (cit. on pp. 5, 6).

Rossi, Massimiliano et al. (Nov. 2018). “Measurement-Based Quantum Control of Mechanical Motion”. In: *Nature* 563.7729, pp. 53–58. ISSN: 0028-0836. DOI: 10.1038/s41586-018-0643-8. URL: http://www.nature.com/articles/s41586-018-0643-8 (cit. on p. 94).

Schrödinger, E. (1926). “Quantisierung Als Eigenwertproblem”. In: *Annalen der Physik* 384.4, pp. 361–376. ISSN: 1521-3889. DOI: 10.1002/andp.19263840404. URL: https://onlinelibrary.wiley.com/doi/abs/10.1002/andp.19263840404 (visited on 03/07/2023) (cit. on p. 3).

Shkarin, A. B. et al. (Apr. 15, 2019). “Quantum Optomechanics in a Liquid”. In: *Physical Review Letters* 122.15, p. 153601. DOI: 10.1103/PhysRevLett.122.153601. URL: https://link.aps.org/doi/10.1103/PhysRevLett.122.153601 (visited on 03/07/2023) (cit. on p. 5).

Tsaturyan, Y. et al. (Aug. 1, 2017). “Ultracoherent Nanomechanical Resonators via Soft Clamping and Dissipation Dilution”. In: *Nature Nanotechnology* 12.8, pp. 776–783. ISSN: 1748-3395. DOI: 10.1038/nnano.2017.101. URL: https://doi.org/10.1038/nnano.2017.101 (cit. on pp. 43, 45, 46).

Tsaturyan, Yeghishe (2019). “Ultracoherent Soft-Clamped Mechanical Resonators for Quantum Cavity Optomechanics”. Niels Bohr Institute, Faculty of Science, University of Copenhagen (cit. on pp. 43, 44).

Underwood, M. et al. (Dec. 2015). “Measurement of the Motional Sidebands of a Nanogram-Scale Oscillator in the Quantum Regime”. In: *Physical Review A: Atomic, Molecular, and Optical Physics* 92.6, p. 061801. ISSN: 1050-2947. DOI: 10.1103/PhysRevA.92.061801. URL: https://link.aps.org/doi/10.1103/PhysRevA.92.061801 (cit. on p. 91).

Walls, D.F. and G.J. Milburn (2008). *Quantum Optics*. Springer Berlin Heidelberg. ISBN: 978-3-540-28573-1. URL: https://books.google.dk/books?id=LiWsc3Nlf0kC (cit. on pp. 16, 109).

Weinstein, A. J. et al. (Oct. 2014). “Observation and Interpretation of Motional Sideband Asymmetry in a Quantum Electromechanical Device”. In: *Physical Review X* 4.4, p. 041003. ISSN: 21603308. DOI: 10.1103/PhysRevX.4.041003. arXiv: 1404.3242. URL: https://link.aps.org/doi/10.1103/PhysRevX.4.041003 (cit. on p. 91).

Weis, S. et al. (2011). “Optomechanically Induced Transparency”. In: *2011 Conference on Lasers and Electro-Optics Europe and 12th European Quantum Electronics Conference, CLEO EUROPE/EQEC 2011* 58.22, pp. 23236–23246. ISSN: 0036-8075. DOI: 10.1109/CLEOE.2011.5943657. pmid: 21071628 (cit. on p. 50).

Wilson-Rae, I. et al. (Aug. 2007). “Theory of Ground State Cooling of a Mechanical Oscillator Using Dynamical Backaction”. In: *Physical Review Letters* 99.9, p. 093901. DOI: 10.1103/PhysRevLett.99.093901. URL: https://link.aps.org/doi/10.1103/PhysRevLett.99.093901 (cit. on p. 88).

Woolley, M. J. and A. A. Clerk (June 28, 2013). “Two-Mode Back-Action-Evading Measurements in Cavity Optomechanics”. In: *Physical Review A* 87.6, p. 063846. DOI: 10.1103/PhysRevA.87.063846. URL: https://link.aps.org/doi/10.1103/PhysRevA.87.063846 (visited on 02/18/2023) (cit. on p. 29).

Zhang, Grace H. et al. (2015). “Note: Fast Compact Laser Shutter Using a Direct Current Motor and Three-Dimensional Printing”. In: *Review of Scientific Instruments* 86.12, p. 126105. DOI: 10.1063/1.4937614. eprint: https://doi.org/10.1063/1.4937614. URL: https://doi.org/10.1063/1.4937614 (cit. on p. 83).

Zhang, Jie et al. (Mar. 7, 2013). “Design of an Optical Reference Cavity with Low Thermal Noise Limit and Flexible Thermal Expansion Properties”. In: *The European Physical Journal D* 67.2, p. 46. ISSN: 1434-6079. DOI: 10.1140/epjd/e2013-30458-2. URL: https://doi.org/10.1140/epjd/e2013-30458-2 (visited on 02/25/2023) (cit. on pp. 74, 80).

Zhang, W. et al. (Dec. 15, 2017). “Ultrastable Silicon Cavity in a Continuously Operating Closed-Cycle Cryostat at 4 K”. In: *Physical Review Letters* 119.24, p. 243601. DOI: 10.1103/PhysRevLett.119.243601. URL: https://link.aps.org/doi/10.1103/PhysRevLett.119.243601 (visited on 02/26/2023) (cit. on p. 71).

Zwettler, Timo (Sept. 16, 2019). “Suppression of Heating Mechanisms for Deep Optomechanical Ground-State Cooling”. M.Sc. thesis. Copenhagen, Denmark; München, Germany: Ludwig Maximilians Universität, München; University of Copenhagen (cit. on pp. 46, 56, 57, 102–104).